Keele
UNIVERSITY

This work is protected by copyright and other intellectual property rights and duplication or sale of all or part is not permitted, except that material may be duplicated by you for research, private study, criticism/review or educational purposes. Electronic or print copies are for your own personal, non-commercial use and shall not be passed to any other individual. No quotation may be published without proper acknowledgement. For any other use, or to quote extensively from the work, permission must be obtained from the copyright holder/s.

The fate of massive single stars: exploring the impact of rotation and metallicity

Caitlan Sarah Chambers

Master of Philosophy

Keele University

December 2024

Abstract

The fate of massive stars depends largely on the mass and structure of their inner cores, and the composition of their envelopes at death. This is dependent on the mass loss history of the star, which has significant effects on the evolution of massive stars, how they die, and the remnants which they leave behind. In this work, the remnant and supernova type of massive stars are mapped as a function of initial mass and metallicity, aiming to determine where neutron stars and black holes are likely to form, and where the different types of supernovae are produced. These results are combined with various formulations of the initial mass function, aiming to find the fraction of massive stars forming each remnant type and producing each type of supernova, at each metallicity considered. This relies on the data from complete grids of stellar evolution models across a large range in initial mass and metallicity, which have been computed using `GENEC` over the past decade. Consistent input physics allows for interpolation of their properties across an evenly spaced grid of initial masses, so that the impact of changing metallicity and rotation can be examined on a macroscopic scale. A significant proportion of massive stars are found to end their lives as neutron stars, exploding as Type IIP supernovae. Despite this, the fate of massive stars is highly variable across metallicity, in particular with relation to pair-instability supernovae, which leave behind no remnant. The location of the pair-instability mass gap is also considered, with reference to recent gravitational wave detections. Considering the fate of massive single stars has far-reaching consequences

across many different fields within astrophysics, and understanding the impact of rotation and metallicity will contribute to an improved understanding of how massive stars end their lives and their impact on the universe.

Acknowledgements

Firstly, I would like to thank my supervisor, Prof. Raphael Hirschi, whose academic expertise and guidance over the past year has made this project possible. Alongside this academic support, he has inspired me to take on new, exciting challenges, and has helped me to grow as a person. I look forwards to embarking on my PhD journey together in the upcoming academic year!

I would also like to extend my thanks to Norhasliza Yusof for her help and support over the past year. From running the extra models which are unpublished, but included in this work, to discussing potential results and shaping this thesis in regular meetings, this project would not have been possible without her input. In addition, I would like to thank everyone involved in running the `GENEC` models used in this work, as this has been an ongoing effort across the last decade, upon which this project is based. I am particularly grateful to Vishnu and Em from the Stellar HYdrodynamics, Nucleosynthesis and Evolution group at Keele University, for their daily words of encouragement and many, many coffee breaks spent discussing our research!

Finally, I would like to express my deepest gratitude to my family whose belief in my abilities and unconditional support played an integral role in this journey. To Sacha and Belle: Thank you for everything, I dedicate this thesis to you.

Contents

List of Figures

List of Tables

Chapter 1

Introduction to massive stars

This introductory chapter provides the context for the main research questions and thesis as a whole, highlighting the importance of massive stars from both a theoretical and observational perspective. The aims and objectives of this thesis are outlined, and the structure is presented.

1.1 Definition and properties of massive stars

Massive stars are defined as stars that produce an iron core at the end of their evolution, generally corresponding to stars with $M_{\rm ini} \geq 9\ M_\odot$ (Woosley et al., 2002; Maeder, 2008). Below this mass, the CO core becomes degenerate at the end of helium burning. This means that it does not reach temperatures above 5×10^8 K, and so cannot begin carbon burning. Such stars then evolve along the asymptotic giant branch (AGB), experiencing strong mass loss. This removes what remains of their envelope, and they end their lives as CO white dwarfs. Alternatively, when initial mass is just below $M_{\rm ini} = 9\ M_\odot$, degenerate oxygen-neon cores can form in super-AGB stars (Siess, 2006). They can collapse and give electron capture supernovae (with a neutron star remnant) or lose their envelopes and form an O-Ne-Mg white dwarf (Jones et al., 2013). Above this mass, higher temperatures allow for ignition of carbon in the core, followed by the burning of heavier fuels until an iron core is formed. Due to its unstable nature, this core collapses and can result in a supernova explosion. Hence, the very definition of massive stars has a basis in their final fate. This highlights the importance of considering what may happen at the end of a massive star's life, and the wider implications this may have.

Massive stars are characterised by their high luminosities, short lifetimes, and dramatic deaths. They are distinctive objects that shape their host galaxies through contributing to the luminosity of the galaxy as a whole and enriching its chemical composition. Additionally, they leave behind both neutron stars and black holes as compact remnants, leaving a lasting legacy long after their deaths. Such stars have a significant influence on the universe through synthesis of heavy elements, aiding reionisation and providing kinetic energy input to their surroundings (Murphy et al., 2021). They are progenitors of supernovae, which are one of the main sources of heavy elements in the universe (Woosley and Janka, 2005), contributing significantly to the chemical complexity of their host galaxies. Furthermore, the shockwaves that they generate can act as a catalyst to the formation of new stars (Weaver, 1976). This interest in the fate of massive stars and how it may be influenced by different factors is a source of motivation for this work.

One aim of stellar evolution models is to reproduce observations, and to aid in their analysis. Hence, it is important to consider notable observations of massive stars and any observational constrains on stellar models. In particular, the central object of the 30 Doradus star-forming region in the Large Magellanic Cloud, R136, was found to have a mass of 2500 $M_\odot$ by Cassinelli et al. (1981), but it was later shown that R136 is a young cluster of lower mass objects, each with mass within the range $165 - 320$ $M_\odot$ (Crowther et al., 2010; Brands et al., 2022).

This highlights the uncertainties around finding the mass of observed objects depending on resolution, and which relies on the use of models unless the star is part of a spectroscopic binary system (Batten, 1968; Zucker and Alexander, 2006). The longest stage of stellar evolution is the main sequence, followed by the helium burning phase. Thus, many observations made are of stars in the early stages of their evolution, as the later stages get shorter and so the likelihood of observing a star in the advanced stages of evolution is low. Generally, only the surface properties of stars can be observed (such as surface chemical abundance, effective temperature, luminosity) using spectroscopic methods and atmospheric models. These observational properties can be compared to those of stellar evolution models to deduce additional information about the observed star(s) and accuracy of the models. The ability to reproduce observational results accurately is important for stellar models; there is a clear interdependence between observations and models. This highlights the importance of modelling massive stars, and is another source of motivation for this work.

The initial mass function (IMF) describes the number density of stars in relation to their initial mass, commonly denoted by Eq. (1.1) and known as the Salpeter IMF, with an exponent of $\alpha = 2.35$ for stars with $M > 0.5\ M_\odot$ (Salpeter, 1955).

$$\frac{dN}{dM} = M^{-\alpha} \tag{1.1}$$

According to the Salpeter IMF, for every star with an initial mass of 100 $M_\odot$, there are almost 300 with $M_{\rm ini} = 9\ M_\odot$ and over 50,000 with $M_{\rm ini} = 1\ M_\odot$. This exponential relation may seem to suggest that massive stars are insignificant, due to their low number density. However, this does not account for the fact that they are responsible for the nucleosynthesis of heavy elements, and have much higher luminosities than other stars. They disproportionately affect their environments when compared to stars of lower mass, and so their significance should not be underestimated. Other formulations of the IMF suggest that massive stars may be more common than initially suggested by the Salpeter IMF, and that this may depend on their metallicity, or take the form of a broken power-law (see Section 1.2.1 for an in-depth discussion of this). Very massive stars are not included in the mass range covered by the Salpeter IMF and so changes and additions are required when considering these stars.

Very massive stars are defined as stars with $M_{\mathrm{ini}} \geq 100\ M_{\odot}$ (Yusof et al., 2013; Köhler et al., 2015; Martinet et al., 2023; Zinnecker and Yorke, 2007). They are even less numerous than massive stars, see Eq. (1.1), but were possibly more common in the metal-poor early universe. It is widely accepted that this can be represented by an updated IMF, with an extended mass range, that levels off at higher masses and low values of metallicity (Wollenberg et al., 2020; Hirano et al., 2014; Nakamura and Umemura, 2001) as discussed in Section 1.2.1. With their luminosities approaching the Eddington limit, very massive stars generally experience mass loss rates much larger than those experienced by massive stars, which has a direct impact on their fates. The Eddington limit is a critical luminosity at which a star's radiation pressure balances its gravitational forces, given by Eq. (1.2).

$$L_{\mathrm{Edd}} = \frac{4\pi G M c}{\kappa} \tag{1.2}$$

where G is the gravitational constant, M is the mass of the star, c is the speed of light and κ is the opacity.

As shown by Eq. (1.2), the Eddington limit increases with mass, but decreases with opacity, which is related to metallicity. Hence, mass loss due to proximity to the Eddington limit is one mechanism by which very massive stars with low metallicities can lose significant amounts of mass throughout their evolution, despite having a lower opacity. It has also been suggested by Sanyal et al. (2015) that most stars above 40 $M_\odot$ exceed the Eddington limit, and so these effects may apply to all massive stars, not just very massive stars.

1.2 The life and death of massive stars

Before considering the fate of massive stars, it is important to consider their evolution to provide the context for both the methodology and results of this work, presented in Chapters 2 and 3. After all, it is the evolution of a star throughout its life that shapes its death and final fate. Additionally, considerations of how massive stars form are useful when considering the IMF, which is used in this work when determining the fraction of massive stars per remnant and supernova type in Chapter 4 and allows for comparisons to be made with observational data. The existence of an upper mass limit is also explored, as this work considers stars with initial mass of up to 500 $M_\odot$.

1.2.1 Formation and the IMF

The formation of massive stars is an uncertain process; the questions of how massive stars form and whether an upper mass limit to this formation exists remain unanswered. Despite such uncertainties, there are two main models for the formation of massive stars: through accretion or as a result of collisions between stars of lower mass. The work of Larson (1971) highlighted issues with existing theories when applied to the formation of massive stars, and also discussed the existence of an upper mass limit for star formation. It has been suggested that this upper mass limit exists at $M \approx 150\ M_\odot$ (Figer, 2005; Weidner and Kroupa, 2004), which is significantly higher than that initially given by Larson (1971). A similar limit in the range of $120 \leq M \leq 200\ M_\odot$ was given by Oey and Clarke (2005), but it is important to note that these limits represent a *statistical* upper mass limit based on the analysis of observational data. Similarly, Larson (1982) suggested that the upper mass limit is scaled by the mass of the molecular cloud in which the star forms, and so is variable such that a cloud of mass $10^5\ M_\odot$ can form a $50\ M_\odot$ star.

The existence of a *physical* upper mass limit is a different question to which there is not yet an answer. The mass-luminosity relation is commonly given as $L \propto M^3$, which is valid for stars wherein the radiation pressure is negligible. Using this relation, the Eddington luminosity is reached when $M \approx 150\ M_\odot$, giving an effective upper mass limit. However, this is not the case for massive stars which have a mass-luminosity relation of $L \propto M$ which gives a much higher theoretical mass limit (Yusof et al., 2013).

It is largely accepted that low and intermediate mass stars form by accretion, and it is possible that massive stars also form in the same way (Haemmerlé et al., 2016). There are two ways that a star can form by accretion: core accretion or competitive accretion (Krumholz et al., 2005; Tan et al., 2014). Initially, a disturbance to the pressure equilibrium of an interstellar cloud, caused by either a collision with another cloud or a supernova explosion in the vicinity of the cloud, leads it to partially collapse under its own gravity. It then fragments into smaller clouds which also begin to collapse; this fragmentation continues until the cloud fragments are sufficiently small. Here is the first issue when applying this theory of star formation to that of massive stars: these fragments tend to have mass approximately equal to the Jeans mass, given by Eq. (1.3) as derived in Maeder (2008), Section 18.2.1, which is generally smaller than the mass of a protostellar core that goes on to form a massive star (Tan et al., 2014).

$$M_J = 4 \times 10^4 \ M_\odot \left(\frac{T}{100 \text{ K}}\right)^{\frac{3}{2}} \left(\frac{n}{\text{cm}^{-3}}\right)^{-\frac{1}{2}} \tag{1.3}$$

where T is the temperature and n is the molecular number density.

However, the level of fragmentation may be reduced by both radiation feedback and the presence of magnetic fields, resulting in fewer fragments each with higher mass (Krumholz and McKee, 2008). Radiation feedback further heats the gas, causing the density and Jeans mass to increase. This would mean that massive stars can continue in their formation without fragmenting to a significant extent. However, Peters et al. (2010) conclude that this heating does not stop fragmentation and so the formation of massive stars is still limited, but this was only investigated in regions of lower density than that of a typical massive star forming region.

Magnetic fields transport angular momentum outward through magnetic braking, preventing the formation of accretion disks which are vulnerable to instabilities that cause fragmentation (Myers et al., 2013). The magnetic braking originates from a magnetic tension force caused by inner regions of the cloud collapsing faster than the outer regions (Stahler and Palla, 2008). Magnetic fields also provide extra pressure support that can prevent collapse, unless their magnetic flux to mass ratio remains below a critical value, given by Crutcher (2012). This means that higher fragment masses can be reached before collapse occurs. The effects of radiation feedback and magnetic fields complement each other: early magnetic braking directs gas towards the centre of a forming star. This will increase the accretion rate, and so the luminosity also increases, leading to more effective radiative heating. A lack of fragmentation would suggest that massive stars are more likely to form in single star systems. This is not in line with observational evidence showing that massive stars do not typically form in isolation and have high levels of multiplicity (Chini et al., 2012; Preibisch et al., 2001; Sana et al., 2012). Hence, the extent to which fragmentation occurs and has an impact on the formation of massive stars is very uncertain.

After some degree of fragmentation, the density of the collapsing cloud increases, making the gas opaque to infrared photons, and so the temperature and pressure within the cloud increase to form a protostellar core (Tan et al., 2014). An accretion disk forms about the protostellar core, whereby the surrounding gas falls onto the core. The resulting gravitational energy either contributes towards heating the core or is radiated away, acting as a source of luminosity. The molecular hydrogen within the protostar begins to dissociate into atomic hydrogen due to rising temperatures, and any gravitational energy is absorbed by the dissociating molecules. Hence, hydrostatic equilibrium is no longer possible, and the temperature stops rising. Once all of the hydrogen has been dissociated, a state of hydrostatic equilibrium is reached again and the temperature starts to increase. At higher temperatures, this process repeats for the ionisation of helium. When the ionisation processes are complete, the protostar is once again in a state of hydrostatic equilibrium with a much smaller radius. Ionisation may cause accretion to slow once the mass of the protostar exceeds $50 - 100\ M_\odot$, eventually causing accretion to stop at $150\ M_\odot$ (McKee and Tan, 2008). This effect is largely reliant on the environment around the protostar, and so the potential limitation on accretion and mass is uncertain. When the rate of accretion does eventually slow to zero, the protostar becomes a pre-main sequence star.

Note that massive stars are likely to be still undergoing accretion throughout the main sequence, due to the timescale of accretion being longer than that of the main sequence (see the lifetimes given by Iben (1965) for example), highlighting another issue with the accretion mechanism when considering the formation of massive stars. Forming a star above 100 $M_\odot$ with an accretion timescale less than its main sequence lifetime (on the order of a few Myr) would need very high accretion rates, which are more likely to increase fragmentation. So even if massive stars can form by accretion, this may not be possible for very massive stars. In the most widely accepted mechanism of formation by which stars are thought to form, the surface cools, and a temperature gradient transporting heat towards the surface forms. The star is too cool to begin nuclear burning, and so the source of luminosity is gravitational contraction, which continues until core temperatures are high enough for hydrogen fusion to begin. In very massive stars, the temperatures required to begin burning hydrogen are reached before the rate of accretion reaches zero, and so there is likely an overlap between these two phases (Keto and Wood, 2006).

Alternatively, (very) massive stars may form by collision. This mechanism of formation also presents challenges, especially when considering collisions between massive stars: they have short lifetimes which limits when collisions could occur and there is generally a large separation between them. This would require clusters of very high density, which have not been observed (see Portegies Zwart et al. (2010) for a review on the topic). Due to this, models of formation of massive stars by collision centre around inducing a short-lived phase of high density in young clusters. For example, Bonnell and Bate (2005) employ high-mass close binary systems formed through accretion which merge to form very massive stars. Overall, the literature considered suggests that most stars form via accretion, but very massive stars may form during collisions between massive stars. Since stars of lower mass are thought to form via accretion, formation by collision would mean that (very) massive stars are members of a distinct population when considering initial mass functions, due to this alternative mechanism of formation. There is some observational evidence for a power-law break in the IMF at high masses, suggesting that the IMF may take the form of Eq. (1.4), edited from Stanway and Eldridge (2019) for consideration of massive stars.

$$\frac{dN}{dM} = \int_{M_l}^{M_m} M^{-\alpha_m} dM + \int_{M_m}^{M_u} M^{-\alpha_u} dM \tag{1.4}$$

where α has the same meaning as within the Salpeter IMF given by Eq. (1.1), and the subscripts l, m, u refer to a lower mass limit, massive star mass limit and upper mass limit, and their respective exponents.

The 30 Doradus star-forming region in the Large Magellanic Cloud ($Z = 0.006$) has been found to contain up to 32% more stars with $M > 30\ M_\odot$ than predicted by the Salpeter IMF (see Section 1.1). An exponent of $\alpha = 1.90$ for Eq. (1.1) has been calculated based on spectroscopic observations of stars with mass ranging from 15 $M_\odot$ to 200 $M_\odot$, as shown in Fig. 1.1 (Schneider et al., 2018). From this, the exponents in Eq. (1.4) can be given as $\alpha_m = 2.35$ and $\alpha_u = 1.90$ where M_m and M_u correspond to the mass value at which the IMF breaks and an upper mass limit. It is important to note that a significant proportion of the sample stars considered by Schneider et al. (2018) were expected to be products of mass transfer in binary systems, and so the calculated IMF exponent may not be accurate for single stars. However, binary mass transfer also results in stars appearing younger than they are, and so these two effects may cancel each other out (Schneider et al., 2013). This highlights the uncertainty in such calculations, which is important to consider when drawing conclusions from IMF weighted proportions of remnant and supernova type (see Chapter 3).

It has also been shown that metallicity may influence the IMF, such that low

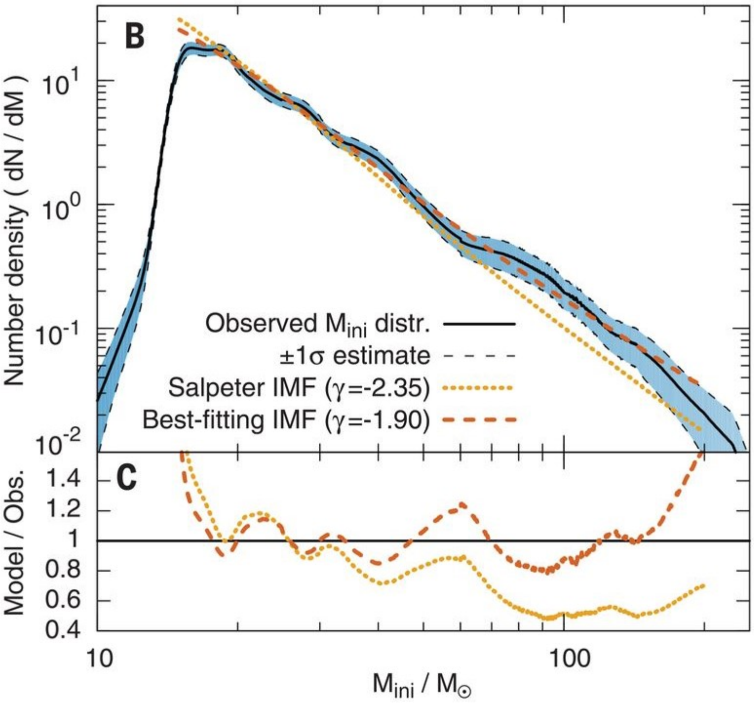

Figure 1.1: Distribution of initial masses of massive stars in 30 Doradus. Taken from Schneider et al. (2018) (Fig. 1).

metallicities result in a heavier mass distribution than higher metallicities (Tanvir and Krumholz, 2024; Marks et al., 2012; Li et al., 2023; Nakamura and Umemura, 2001; Ohkubo et al., 2009; Chon et al., 2021). Metallicity directly impacts dust abundances, which is important as dust couples gas to stellar radiation fields. Decreasing the metallicity causes less fragmentation due to the effects of radiation feedback (as discussed above), reducing the amount of cooling during formation (Bromm et al., 1999; Ohkubo et al., 2009; Li et al., 2023). This effect is only seen at higher masses, and it is acknowledged by Tanvir and Krumholz (2024) that variations in the IMF due to metallicity have limited significance. Despite this, there is increasing evidence that mass distributions at low metallicities are 'top-heavy' (Marks et al., 2012; Li et al., 2023; Nakamura and Umemura, 2001), but no functional relations describing how the number density varies with metallicity have been given. However, Bate (2019) found that changes in metallicity have very little effect on the IMF, using radiation hydrodynamical simulations to reach their conclusions rather than observations. The effect of varying metallicity on the IMF is one avenue for exploration in this work due to its uncertain nature, with the aim of calculating the proportions of different remnant/supernova types from massive stars and comparing results with observational data.

The formation of massive stars is linked to their fates through the consideration of an upper mass limit and the formulation of the IMF. If (very) massive stars form a distinct population due to different formation mechanism, then the analysis of their fates must account for this, particularly when considering the proportion of massive stars that form different types of remnant and explode as different types of supernova. Additionally, if an upper mass limit below $M \approx 120\ M_\odot$ exists, then there is no need to consider pair-instability supernovae as a potential fate, as their progenitors are thought to be very massive stars (Farmer et al., 2019).

Uncertainties in the mechanism of star formation and therefore the distribution of initial masses may seem like a very significant issue when considering the evolution and fate of massive stars. However, this is not the case. Once the star reaches hydrostatic and thermal equilibrium on the main sequence, the structure and evolution of the star over time only depend on the initial composition and the four stellar structure equations given in Chapter 2. Hence, by the time nuclear burning begins, issues around the formation mechanism do not translate into uncertainties in their structure.

The time a star takes to start hydrogen burning and reach the zero-age main sequence (ZAMS) depends on its mass. Since nuclear burning has not yet begun, this depends on gravitational contraction and so occurs on the Kelvin-Helmholtz thermal timescale, approximately given by Eq. (1.5), with the mass relation for the time taken to reach the ZAMS given by Eq. (1.6).

$$\tau_{\mathrm{KH}} \approx \frac{E_{\mathrm{int}}}{L} \approx \frac{|E_{\mathrm{grav}}|}{2L} \approx \frac{GM^2}{2RL} \tag{1.5}$$

$$\tau_{\mathrm{ZAMS}} \approx 10^7 \left(\frac{M}{M_\odot}\right)^{-2.5} yr \tag{1.6}$$

It is important to note that the nuclear timescale, τ_{nuc}, is at least two orders of magnitude longer than the Kelvin-Helmholtz timescale, which is many orders of magnitude longer than the dynamical timescale, τ_{dyn}. Hence, nuclear reactions generally determine the pace of stellar evolution, apart from when they are inefficient, or have not yet begun.

1.2.2 Early stages

Massive stars spend most of their lives on the main sequence. At the onset of hydrogen burning in the core, the temperature and pressure in the core of massive stars is high enough that the CNO cycle dominates over the $pp-$chain (above $T \approx 2 \times 10^7$ K). This is also the point at which the structure of a typical low mass star with a radiative core and a convective envelope switches to that of a massive star with a convective core and a radiative envelope. The nuclear binding energy released by the reactions of the CNO cycle account for the energy generation of core hydrogen burning, and balance gravity and the significant energy loss at the surface. The reactions of the various CNO cycles are summarised in Fig. 1.2. The general idea is that helium is formed from hydrogen using carbon, nitrogen and oxygen as ‘catalysts’ whereby they are involved in the reactions but are regenerated.

Once hydrogen in the core is fully depleted, there is no longer any energy generated in the core and a hydrogen burning shell provides the energy needed for

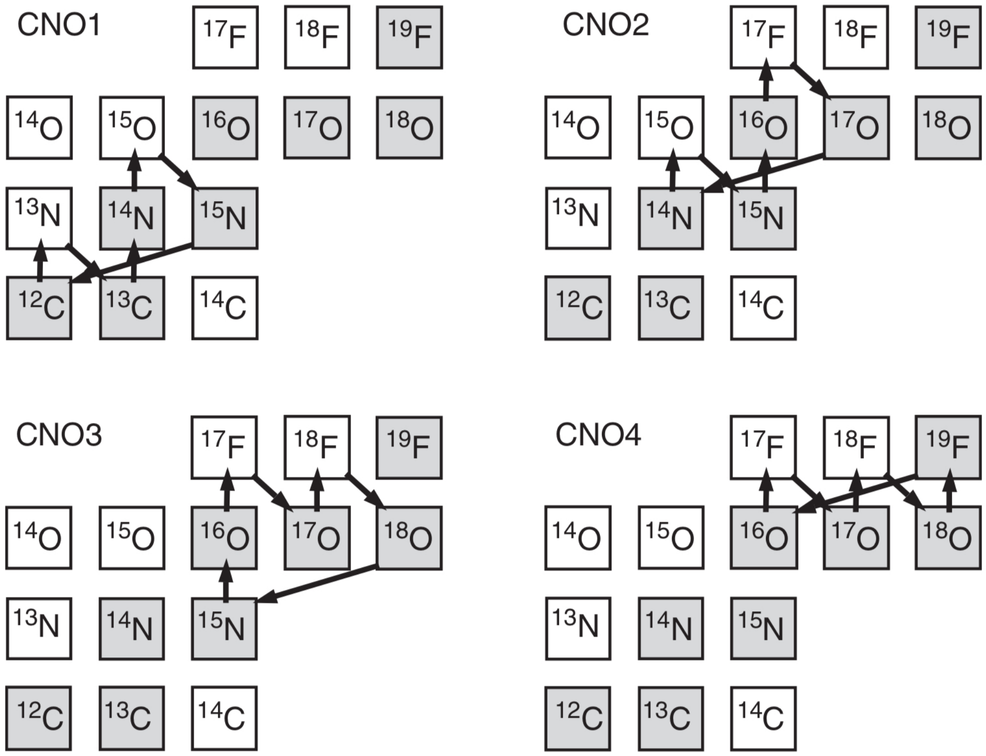

Figure 1.2: The CNO cycle, with stable nuclei shown as shaded squares. Taken from Iliadis (2015) (Fig. 5.8).

the star to remain in equilibrium. It is important to note that core and shell burning are distinct processes: shell burning occurs in an environment with higher temperatures and pressures so will have a slightly different nucleosynthesis. Hydrogen burning can also occur through the Ne-Na and Mg-Al cycles at high enough temperatures, such as those reached during shell hydrogen burning. In the final reaction in the CNO4 cycle given in Fig. 1.2, ^{18}F can instead combine with an alpha particle to start the Ne-Na cycle, if high enough temperatures are reached. Furthermore, when the temperature increases further, above $T \approx 3.5 - 4 \times 10^7$ K, the Mg-Al cycle can branch off from the Ne-Na cycle. This leads to the production of ^{26}Al through proton captures on ^{25}Mg, which acts as an observational marker for massive star formation in the universe (Prantzos and Diehl, 1996; Meynet et al., 1997). These reactions are unlikely to occur during core hydrogen burning as they require much higher temperatures. The CNO cycle has a significantly higher temperature dependence than the $pp-$chain, so stars with higher mass burn hydrogen at a faster rate and so spend less time on the main sequence. At this point in the evolution, the core is rapidly contracting while the envelope expands; this is often described as 'mirror-like' behaviour (see Sugimoto and Fujimoto (2000) for a review of possible mechanisms and Padmanabhan (2000) for a simple explanation of this effect). For the star to remain in thermal equilibrium, the temperature of the hydrogen burning shell must remain constant. If the shell were to contract, this would lead to an increase in temperature, hence the radius of the shell must also remain constant. Thus, as the core contracts, the *density* of the shell must decrease and it follows that the pressure of the shell would also decrease. And so the pressure of the envelope must decrease, leading to an increase in the radius of the envelope above the shell, maintaining thermal and hydrostatic equilibrium. The contraction happens rapidly on the Kelvin-Helmholtz thermal timescale, Eq. (1.5), continuing until helium burning begins at $T \approx 5 \times 10^8$ K.

Core helium burning is a significantly shorter phase where the 3α reaction accounts for energy generation in the core. The 3α reaction has two steps, starting with the fusion of two alpha particles to form unstable ^{8}Be, given by Eq. (1.7). Then, a third alpha particle participates in the reaction given by Eq. (1.8), if the unstable ^{8}Be has not already decayed back into two alpha particles.

$$^{4}\mathrm{He} + {}^{4}\mathrm{He} \rightarrow {}^{8}\mathrm{Be} + \gamma \tag{1.7}$$

$$^{4}\mathrm{He} + {}^{8}\mathrm{Be} \rightarrow {}^{12}\mathrm{C} + \gamma \tag{1.8}$$

This process has a sensitive dependence on temperature due to the very short half life of ^{8}Be, as a third alpha particle needs to react with the unstable ^{8}Be before it can undergo α-disintegration. Overall, the 3α reaction increases the core abundance of ^{12}C. However, when temperatures increase further and the abundance of carbon is high enough, the reaction $^{12}\mathrm{C}(\alpha, \gamma)^{16}\mathrm{O}$ begins to produce oxygen at the expense of carbon. It is more efficient in massive stars and so the C/O ratio found at the end of core helium burning is lower in stars with higher mass. This reaction is important when considering the fate of massive stars: if it has a faster rate, then there is less C left in the core at the onset of carbon burning which then leads to the core carbon burning phase being shorter (Tur et al., 2007). This means that there is less energy loss via neutrinos during the advanced phases and so the star has a higher core mass, directly influencing the fate and 'explodability' of the star.

Uncertainties around the rate of this reaction introduce problems in predicting the fate of massive stars. There have been a series of attempts to determine the temperature dependence of the rate (Caughlan et al., 1985; Holt et al., 2019), but uncertainties persist. Small variations in this rate affect the determination of the fate of massive stars significantly, particularly when considering if stars at low metallicity end their lives as PISN (Farmer et al. (2020); Takahashi (2018), also see Section 1.2.4).

The C/O ratio and the CO core mass are both factors that significantly impact the compactness of pre-supernova stellar cores, and hence affect the explodability of the star and its final fate (Sukhbold and Woosley, 2014). The C/O ratio is strongly related to the initial mass of the star, and so consideration of the CO core mass alone is sufficient for the purposes of this work. See however Farmer et al. (2019) for an example of how changing the C/O ratio by varying the ^{12}C$(\alpha,\gamma)^{16}$O reaction rate can change the boundaries for determining the fate of a massive star. From the end of core helium burning, the CO core mass remains constant and so, in this work, the CO core mass at the end of helium burning is used to determine the type of remnant left behind by massive stars (see Chapter 3).

In very massive stars, even higher temperatures are reached and so the reactions ^{16}O$(\alpha,\gamma)^{20}$Ne and ^{20}Ne$(\alpha,\gamma)^{24}$Mg continue to reduce the abundance of helium remaining in the core. In addition to these reactions, the helium burning core allows for further nucleosynthesis via the slow neutron-capture process (s-process), to produce even heavier elements (Woosley et al., 2002). From the end of core helium burning, the evolution of the core is disconnected from that of the envelope as they evolve on very different timescales (the Kelvin-Helmholtz thermal timescale of the envelope and the nuclear timescale of the core diverge significantly at this point) and so the core evolution cannot be inferred from surface properties. At the end of helium burning, the core is mostly composed of ^{12}C and ^{16}O, and ^{20}Ne in very massive stars. And so, the early stages of the evolution of a massive star play a significant role in determining their final fate.

Evolution in the HRD

As hydrogen is burned to produce helium during the main sequence, the mean molecular weight, μ, increases. The effects of this can be seen in the HR diagram: massive stars experience an increase in luminosity from the ZAMS to the point when the central hydrogen abundance decreases significantly at the end of core hydrogen burning, as shown by Fig. 1.3. Generally, chemically inhomogeneous stars evolve above and to the right of the ZAMS, as shown by the left panel of Fig. 1.3. When the core hydrogen abundance is sufficiently low, burning moves outwards towards the edge of the core as it contracts. The surface effects of this can be seen as a ‘hook’ in the HR diagram towards higher effective temperatures, marked by a blue dot in Fig. 1.3. The start of core helium burning is marked by the green dot in Fig. 1.3 at lower effective temperature and higher luminosity due to the mirror-like behaviour explained in Section 1.2.2. Very massive stars are almost chemically homogeneous, and so evolution in the HR diagram during core helium burning is different for massive and very massive stars, as shown by Fig. 1.3. Very massive stars evolve vertically in the HR diagram, covering a wide range of luminosities over a narrow range of effective temperatures, due to significant mixing as a result of extensive convective zones alongside strong mass loss. The track of the 150 $M_{\odot}$ star shown in the right panel of Fig. 1.3 evolves to lower effective temperature prior to the end of core helium burning, which is shown in Fig. 1.3 as an orange dot, due to the expansion of the envelope caused by energy released during core contraction (similar behaviour to that at the end of hydrogen burning).

1.2.3 Advanced stages

When a significant amount of helium in the core has been depleted, the core begins to contract again. During this process, the star is sustained by a hydrogen burning shell and a helium burning shell. This continues until the temperature

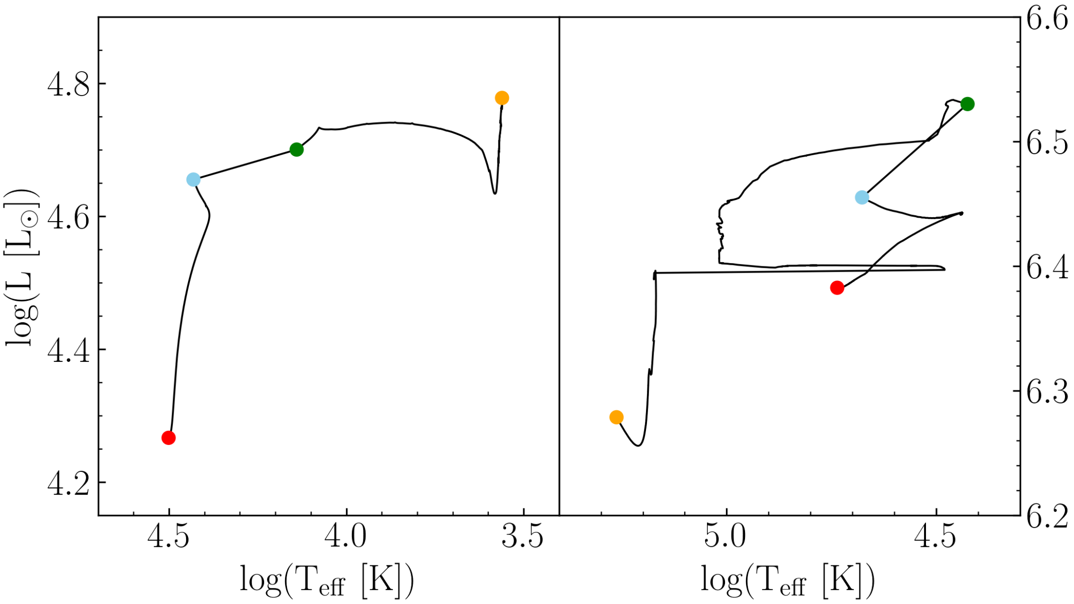

Figure 1.3: HR diagrams with evolutionary tracks for non-rotating 15 $M_{\odot}$ (left) and 150 $M_{\odot}$ (right) models at solar metallicity. The red dot indicates the start of core hydrogen burning (ZAMS), blue is the end of core hydrogen burning, green is the start of core helium burning, and orange is the end of core helium burning. Models taken from Ekström et al. (2012).

in the core is high enough for core carbon burning to begin, when $T \approx 6 \times 10^8$ K. Carbon burning proceeds through the $^{12}\mathrm{C} +^{12} \mathrm{C}$ fusion reaction to give ^{24}Mg, which is in an excited state and so decays via various pathways. At this temperature, the most important pathways for this reaction are $^{12}\mathrm{C}(^{12}\mathrm{C}, \alpha)^{20}$Ne and $^{12}\mathrm{C}(^{12}\mathrm{C}, p)^{23}$Na. Towards the end of core carbon burning, the reaction $^{12}\mathrm{C}(^{12}\mathrm{C}, n)^{23}$Mg can also occur due to the increased temperature of the core. Note that in each of the possible pathways, a light particle is emitted in order to carry the excess energy from the production of ^{24}Mg. These light particles can go on to initiate a series of secondary reactions involving the heavier nuclei produced by the primary reactions. After the carbon in the core is exhausted, carbon burning occurs in a series of successive carbon burning shells. At the end of core carbon burning, the core is mostly made up of ^{16}O, ^{20}Ne and ^{23}Na.

Due to the stability of ^{16}O, core oxygen burning does not begin until $T \approx 2 \times 10^9$ K and so photodisintegration of neon in the core occurs first at $T \approx 1.2 \times 10^9$ K. The most important reaction is $^{20}\mathrm{Ne}(\gamma, \alpha)^{16}$O, and the alpha particles produced by this reaction are captured in the $^{20}\mathrm{Ne}(\alpha, \gamma)^{24}$Mg reaction, then again in the $^{24}\mathrm{Mg}(\alpha, \gamma)^{28}$Si reaction. When core neon burning can begin depends on the mass of the CO core at the end of core helium burning: for $M_{\mathrm{CO}} > 3\ M_{\odot}$, it can begin soon after the end of core carbon burning but for $M_{\mathrm{CO}} < 3\ M_{\odot}$, the second carbon burning shell must have disappeared in order for the core to be massive enough for neon burning to begin (Chieffi and Limongi, 2020). At the end of core neon burning, the core is mostly made up of ^{16}O, ^{24}Mg and ^{28}Si. The core contracts again until temperatures are high enough for core oxygen burning to begin.

At this point, massive stars with very low metallicity may end their lives in a pair-instability supernova (PISN). Electron-positron pair production at the start of core oxygen burning causes the star to become unstable, and results in

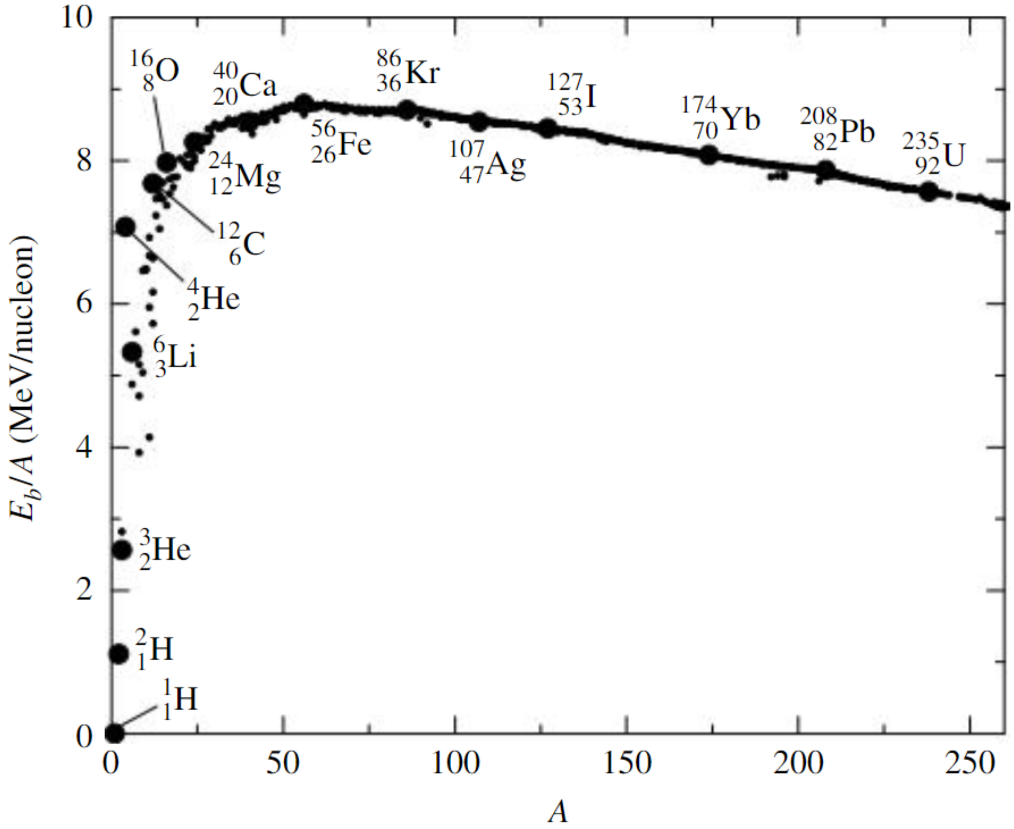

Figure 1.4: Binding energy per nucleon as a function of mass number, A. Taken from Carroll and Ostlie (2017) (Fig. 10.9).

an implosion of the core (Fowler and Hoyle, 1964). A single pulse disrupts the entire star as a PISN, leaving no remnant behind. This is thought to occur in stars at low metallicity with initial masses of $140 - 260\ M_\odot$ (Woosley, 2017). For stars at slightly lower mass or higher metallicity, a pulsational pair-instability supernova (PPISN) may result, ending with a core-collapse supernova and leaving behind a black hole remnant. This occurs when the initial pulse is not energetic enough to completely disrupt the star, and so the core contracts, then continues burning oxygen, then expands and cools then contracts again, and the sequence continues.

Eventually, the core mass is low enough that the star is no longer unstable and can finish oxygen/silicon burning in hydrostatic equilibrium. PPISN have been studied less extensively than PISN in terms of theory, and there have been no confirmed observations of either phenomenon. SN 2007bi is an example of a potential PISN candidate, as it was very luminous and long-lasting (Gal-Yam et al., 2009). Despite the lack of direct observational evidence, a black hole mass gap between $64 - 161\ M_\odot$ has been observed (Woosley and Heger, 2021), which is thought to be due to PISN. The existence of this mass gap has been challenged recently, due to the discovery of black holes that exist as merging pairs, with masses of $\sim 60 - 85\ M_\odot$ (Abbott et al., 2021, 2020) and the location of the mass gap is also still uncertain (Winch et al., 2024).

Otherwise, during core oxygen burning, the $^{16}\mathrm{O} + ^{16}\mathrm{O}$ fusion proceeds in a similar fashion to carbon burning with the emission of light particles due to the production of excited ^{32}S, with many likely reaction pathways and following secondary reactions. The rates for oxygen burning are not known to a large degree of accuracy due to uncertainties around the branching ratios of these different reactions (Spinka and Winkler, 1974; Woosley et al., 2002). At the end of core oxygen

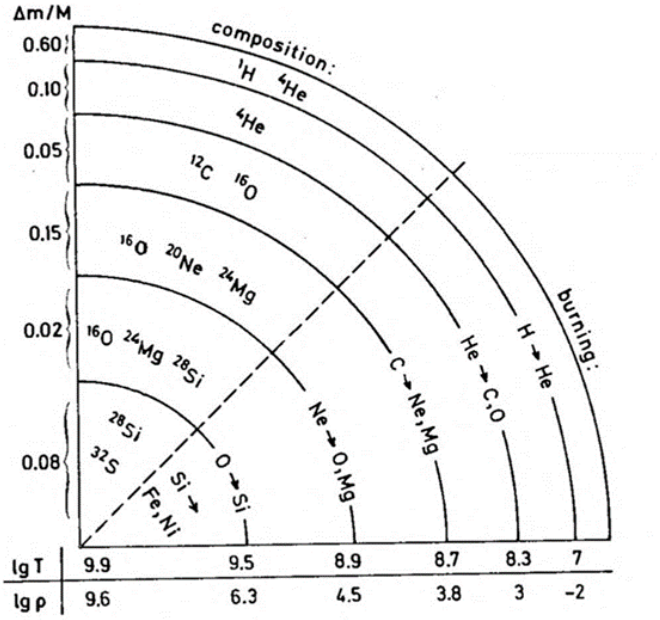

Figure 1.5: Illustration of the structure of the interior of a massive star during the advanced stages of evolution (not to scale). Taken from Kippenhahn et al. (1990) (Fig. 33.1).

burning, the core mostly consists of ^{28}Si and ^{32}S. Once again, the core contracts and the temperature increases but silicon burning does not proceed through the fusion of ^{28}Si with itself, as the Coulomb barrier for the reaction is too high.

Once the core temperature reaches $T \approx 4 \times 10^9$ K, core silicon burning proceeds in a similar way to that of neon: through photodisintegration reactions whereby the silicon nuclei are broken up by high energy thermal photons, releasing light particles (mostly alpha particles) which combine with other nuclei in further secondary reactions (Woosley et al., 1973). Overall, this process results in a complex sequence of reactions forming nuclei with mass numbers from $\sim 30-56$ (Phillips, 2013). Note that ^{62}Ni is the most stable nucleus, as per Fig. 1.4 where it can be found at the peak of the curve, with the highest binding energy. Hence, this is the nucleus at which the Coulomb barrier becomes too high, nuclear fusion becomes endothermic and so stops; heavier nuclei can only be formed through processes such as neutron capture. At the end of silicon burning, nuclear statistical equilibrium is reached by every nuclide from protons to iron-peak elements. However, weak interactions are not involved in this equilibrium as the neutrinos involved leave the star without interaction, as their mean free path is larger than the radius of the star, and so are not involved in the reverse reaction. These weak interactions cause a large neutron excess, favouring neutron-rich isotopes. The structure of the star at this point in the evolution is given by Fig. 1.5, showing the 'onion-like' layers resulting from each burning stage.

Kippenhahn diagram

The advanced stages of evolution can be illustrated in a Kippenhahn diagram, showing convective regions and total mass through the evolution. In Fig. 1.6, the convective alpha core and CO core can be seen during the early phases of evolution, alongside the hydrogen burning shell above the helium burning core. The convective carbon burning core is also shaded, and the series of convective carbon burning shells that follow core carbon burning can be seen. These shells are very significant in determining the fate of a massive star, and are thought to be responsible for the compactness peak discussed in Chapter 3 (Sukhbold and Woosley, 2014). Following this, the advanced phases of evolution continue through core neon, oxygen and silicon burning, illustrating the series of convective cores and burning shells during the evolution.

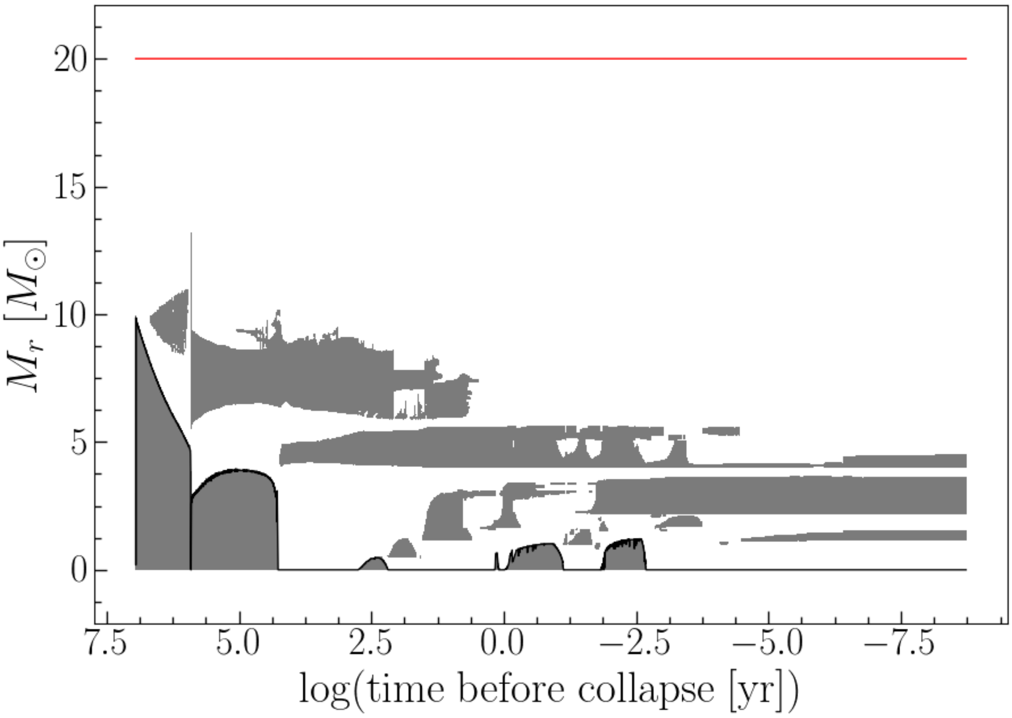

Figure 1.6: Kippenhahn diagram for the 20 $M_\odot$ non-rotating model with Z = 10^{-5}. Model taken from Sibony et al. (2024)

1.2.4 Core collapse and beyond

At the end of silicon burning, the core is largely composed of iron-peak elements. At this point, it becomes inert as insufficient amounts of energy can be released by nuclear reactions. A brief overview of the mechanism by which core collapse and the following supernova explosion occurs will be provided in this section (see Müller et al. (2016) for more detail, and Fig. 1.7 for an overview). At high density and pressure inside the inert core, free electrons are captured onto heavy nuclei and electron degeneracy pressure can no longer support the core against the rapid contraction leading to collapse. Electron captures increase the average mass per free electron, decreasing the electron fraction, Y_e, and it follows that the Chandrasekhar mass also decreases. This means that the core can collapse at a lower mass. A typical iron core in a massive star will have $Y_e \approx 0.45$ and so will have a Chandrasekhar mass of $M_{\mathrm{Ch}} \approx 1.18 M_\odot$, above which it becomes gravitationally unstable (Woosley et al., 2002).

Additionally, photodisintegration of heavy nuclei causes the adiabatic index to fall below 4/3 and so the core becomes dynamically unstable. These reactions require significant amounts of energy, causing the pressure to decrease rapidly on the free-fall timescale, further accelerating the collapse (Fowler and Hoyle, 1964). Electron captures on both bound and free protons also accelerate the collapse, releasing energetic neutrinos, as per Eq. 1.9, which diffuse outward.

$$p + e^- \rightarrow n + \nu_e \tag{1.9}$$

The temperature and pressure continue to increase until nuclear densities are reached, and the collapse is halted by increased pressure from degenerate neutrons and nuclear forces, causing a ‘bounce’. This gives rise to a shock wave which travels outward while the rest of the core is still collapsing. When the collapse

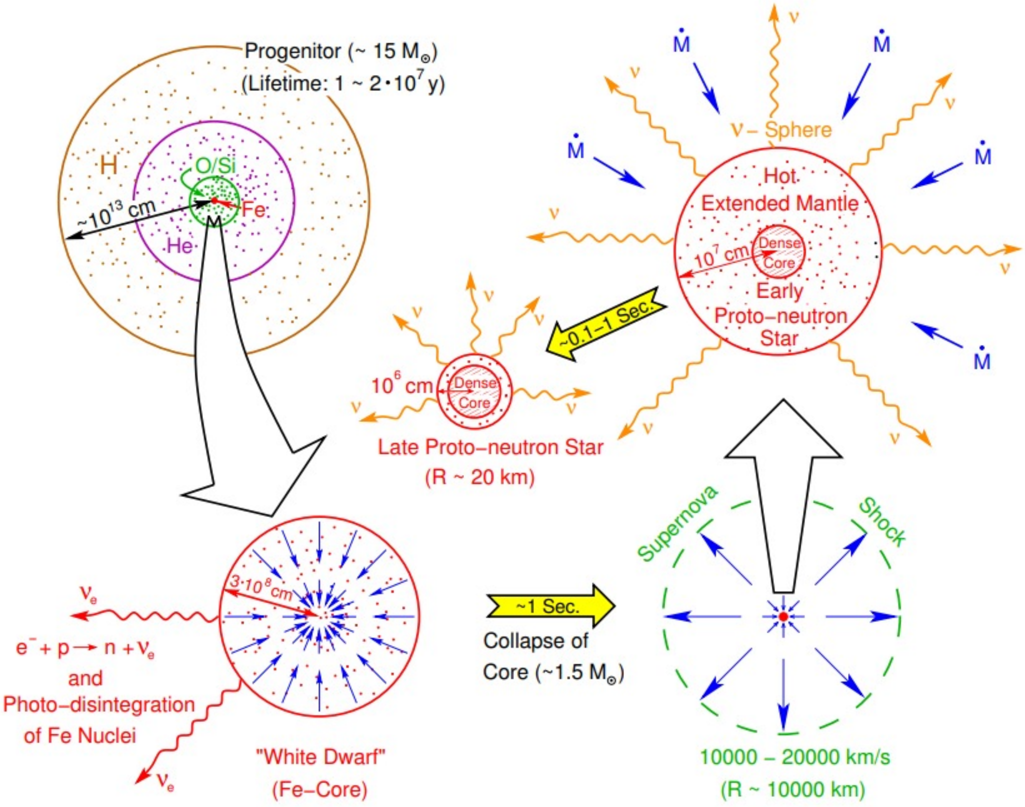

Figure 1.7: Evolution of a massive star from the onset of iron-core collapse to formation of a neutron star. Taken from Janka (2017) (Fig. 2).

is almost complete, neutrinos become trapped in the core as the velocity of the infalling gas is greater than the velocity of the escaping neutrinos, and a 'neutrinosphere' forms (Sato, 1975). It is only in the outer layers of the core that the density is low enough that the neutrinos can escape freely. A region of net neutrino heating emerges in front of the neutrinosphere and behind the shock wave, known as the gain region (Bethe and Wilson, 1985). It is this heating that provides the energy that drives the shock into a supernova explosion. These energetic neutrinos carry away most of the energy released in the collapse and can be detected, such as in the case of SN 1987A (Bionta et al., 1987; Hirata et al., 1987).

In order for an explosion to be possible, there must be a neutrino luminosity above a critical value which can be reduced by convection that prevents spherical symmetry in stars of higher mass (Janka and Müller, 1995). At higher masses, the shock is stalled by the infalling matter and must be revived before an explosion is possible. When there is a failed explosion, some mass can still be ejected from the collapsing core but the shock cannot be revived and so there is no supernova explosion. At this point, massive stars can either collapse directly into a black hole, form a black hole by fallback (both examples of failed supernovae) or explode as a supernova and leave behind a compact remnant (neutron star or black hole). Stars with more compact presupernova cores have higher values of the compactness parameter, $\xi_{2.5}$, and are more likely to be unable to revive the shock (see O'Connor and Ott (2011) and Chapter 3 for more detail). This means that such stars generally fail to explode and form black holes instead of neutron stars.

Since the advanced stages of evolution have very short lifetimes, they cannot be directly observed. However, they can be inferred from observations of supernova

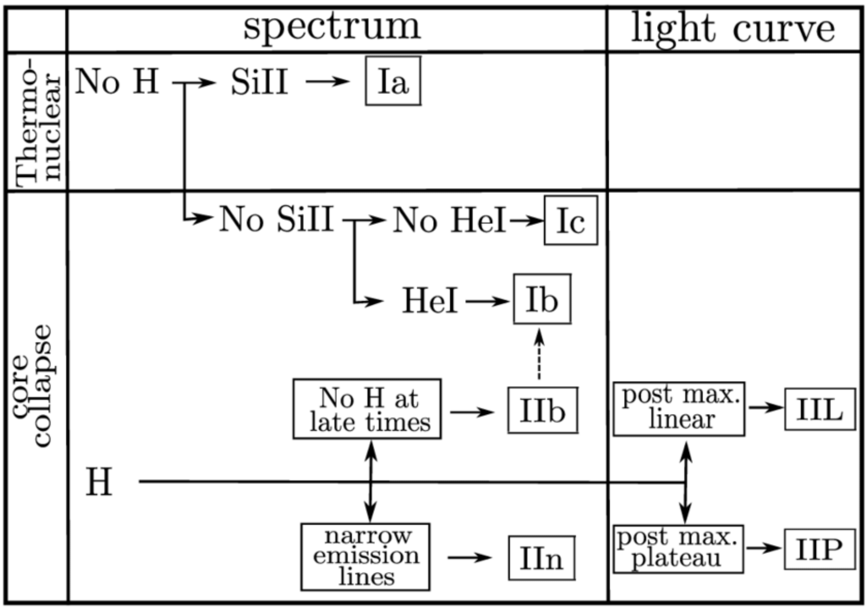

Figure 1.8: Schematic classification of supernovae. Taken from Coelho et al. (2014) (Fig. 1).

explosions (such as SN 1987A and SN 2007bi mentioned above) and compact remnants. Supernova observations usually comprise of both the spectrum and light curve which can be used to calculate properties such as ejected mass and explosion energy. The classification of supernova type is determined by both the spectrum and light curve of the explosion, given in Fig. 1.8.

1.3 This work

In this thesis, the relationship between the life and death of massive single stars is considered. The main aim is to determine the final fate of massive stars from the properties of stellar models at the end of core helium burning. The effects of initial mass, metallicity and rotation on the fate of massive stars are explored, and the role that different processes have on the final stages of evolution is considered. Finally, statistical analysis of the above results is presented to provide an overview of the fate of massive stars on a macroscopic level. Existing rotating and non-rotating models at metallicities from extremely metal poor (EMP), that of the Small Magellanic Cloud (SMC) and Large Magellanic Cloud (LMC) to solar and supersolar, ranging from $9-500\ M_\odot$ are analysed and their collective properties used to determine their final fate. The models were computed using the Geneva Stellar Evolution Code (`GENEC`) using consistent input physics to allow for both comparison and interpolation.

The 'fate' of a massive star is considered to be a comprehensive description of the star during and after death. This includes the type of supernova explosion (if any), the type of compact remnant (if any), and the lasting impact it has on the universe. It is important to note that up to 80% of massive stars form binary systems (Chini et al., 2012), but this work only concerns single stars and neglects any effects resulting from binary interactions. The structure of this thesis is as follows. In Chapter 2, modelling stellar structure and evolution is considered, with a focus on the use of `GENEC`. Analysis of the models used in this work will be provided and discussed. In Chapter 3, the main results are presented. A consideration of remnant and supernova types will be given, and black hole masses determined. Finally, Chapter 4 provides concluding remarks and suggestions for further work.

Chapter 2

Modelling stellar evolution

Complete and homogeneous grids of stellar models enable the analysis of a wide range of observations, and allow for the exploration of how stellar evolution depends on parameters such as initial mass, metallicity and rotation. They are also useful for considering the evolution of progenitors of neutron stars, supernovae and black holes, and also the evolution of galaxies. In this work, rotating and non-rotating stellar models at Z $= 10^{-5},\ 0.002,\ 0.006,\ 0.014,\ 0.02$ ranging from $9 - 500\ M_{\odot}$ are presented from the ongoing series of `GENEC` grids (Ekström et al., 2012; Georgy et al., 2013; Eggenberger et al., 2021; Yusof et al., 2022; Sibony et al., 2024), plus additional models for very massive stars (Yusof et al., 2013; Martinet et al., 2023), alongside models that have been calculated for this work that have not been previously published. A summary of the models and their origin is given in Table A.1, Appendix A. These models have been computed with the same input physics and physical ingredients to allow for direct comparison of their properties across masses and metallicities, facilitating determination of the fate of massive stars across cosmic time, with the exception of those from Martinet et al. (2023) which have slightly different input physics for modelling very massive stars.

This chapter is structured as follows. An introduction to modelling stellar evolution and the equations of stellar structure is given in Section 2.1, a summary of the `GENEC` model and input physics is provided in Section 2.2, properties of the stellar models are given and discussed in Section 2.3 and, from this, conclusions are drawn.

2.1 Stellar structure equations

Stellar structure can be described by four equations, alongside equations of chemical element abundance which are treated separately. Spherical symmetry is not assumed in rotating models, and so in order to treat the problem in 1D, the angular velocity is assumed to be constant on isobars (Zahn, 1992). This case is known as 'shellular rotation', and is used within the `GENEC` model. A summary of these equations as implemented within the code is given below, but for more detail see Meynet and Maeder (1997).

Conservation of mass equation:

$$\frac{\partial r_P}{\partial M_P} = \frac{1}{4\pi r_P^2 \bar{\rho}} \tag{2.1}$$

where M_P is the mass of a shell enclosed by radius r_P and ρ is the density.

Conservation of momentum equation:

$$\frac{\partial P}{\partial M_P} = -\frac{GM_P}{4\pi r_P^4} f_P \tag{2.2}$$

where P is the pressure and G is the gravitational constant.

Conservation of energy equation:

$$\frac{\partial L_P}{\partial M_P} = \epsilon_{\text{nuc}} - \epsilon_\nu + \epsilon_{\text{grav}} \tag{2.3}$$

where L_P is the luminosity and ϵ_ν, $\epsilon_{\rm nuc}$ denote the energy generation rates per unit mass for neutrinos and nuclear reactions,

$$\epsilon_{\rm grav} = -c_P \, \frac{\partial \bar{T}}{\partial t} + \frac{\delta}{\bar{\rho}} \frac{\partial P}{\partial t}$$

denotes gravitational energy changes due to expansion or contraction, t is time, c_P is the specific heat at constant pressure and $\delta = -\partial \ln \rho / \partial \ln T$.

Energy transport equation:

$$\frac{\partial \ln \bar{T}}{\partial M_P} = -\frac{G M_P}{4\pi r_P^4} f_P \min\left[\nabla_{\rm ad}, \nabla_{\rm rad} \frac{f_T}{f_P}\right] \tag{2.4}$$

where T is the temperature,

$$\nabla_{\rm ad} = \frac{P\delta}{\bar{T}\bar{\rho}c_P} \quad \text{(convective zones)},$$
$$\nabla_{\rm rad} = \frac{3}{64\pi\sigma G}\frac{\kappa L_P P}{M_P \bar{T}^4} \quad \text{(radiative zones)},$$

where κ is the total opacity and σ is the Stefan-Boltzmann constant,

$$f_P = \frac{4\pi r_P^4}{G M_P S_P} \frac{1}{\langle g^{-1} \rangle},$$
$$f_T = \left(\frac{4\pi r_P^2}{S_P}\right)^2 \frac{1}{\langle g \rangle \langle g^{-1} \rangle},$$

$\langle x \rangle$ is average on an isobaric surface, $\bar{x}$ is average in the volume separating two successive isobars and the index P refers to the isobar with a pressure equal to P. S_P is the surface of the isobar and g is the effective gravity.

Within `GENEC`, a finite difference method is employed to solve the structure equations. This is a time-implicit method, wherein solutions are computed at every point in a mesh and interpolated between to obtain a general solution. For a description of how the structure equations are implemented in another code see Chieffi et al. (1998). The conservation of mass equation, given by Eq. (2.1), relates the radial mass distribution to the local density, where the mass coordinate $M_P(r_P)$ is a Lagrangian coordinate that increases monotonically outward. It is generally used instead of r, the radius of a spherical shell, as the interval on which the radius is defined changes by significant amounts during the evolution. The momentum equation, Eq. (2.2), demonstrates the conservation of momentum by considering the equation of motion of a gas element within the star and is a simplified form of the Navier-Stokes equations. While a star is in hydrostatic equilibrium, as assumed in this equation, the pressure decreases outwards and the gravitational force balances the pressure forces. The conservation of energy equation, Eq. (2.3) considers local energy conservation to describe changes in the internal energy of the star by heat and work. Heat is added by the release of nuclear energy and removed by the release of energetic neutrinos. The ϵ_ν term accounts for energy released by weak interaction processes; neutrinos released during nuclear reactions are accounted for in the nuclear energy term, $\epsilon_{\rm nuc}$. When $\epsilon_{\rm grav} > 0$, energy is released (contraction), otherwise energy is absorbed by the mass shell (expansion). The energy transport equation, Eq. (2.4), describes how energy is transported outward to the surface, dependent on the temperature gradient. For outward radiative energy transport to occur, a temperature gradient of $\nabla_{\rm rad}$ is required. At higher values of L, this increases. If it increases past $\nabla_{\rm ad}$, then an instability within the gas sets in, resulting in a net buoyancy force upwards that leads to convection. Hence, the stability against convection is determined by the Schwarzschild criterion in this model.

In order to solve the above equations, an equation of state is required. This includes energy, pressure, temperature, density and composition terms. Discussion of the extent of the nuclear reaction network and solution of chemical abundance equations is not within the scope of this work. For a summary of the species, reactions and rates used within `GENEC`, see Ekström et al. (2012), and refer to Chapter 1 for a general consideration of the nucleosynthetic processes within massive stars.

2.1.1 The hydrodynamic momentum equation

Hydrostatic equilibrium is assumed for the equations given in Section 2.1. If this assumption is removed, Eq. (2.2) includes an additional acceleration term (Heger et al., 2000) as per Eq. (2.5).

$$\frac{\partial P}{\partial M_P} = -\frac{GM_P}{4\pi r_P^4} f_P - \frac{1}{4\pi r_P^2}\frac{\partial^2 r_P}{\partial^2 t} \tag{2.5}$$

Eq. (2.4) also includes an additional term if this assumption is removed, but the others remain unchanged. Within `GENEC`, the acceleration terms are not included; hydrostatic equations are used to model stellar evolution.

2.2 Physical ingredients of the models

The initial abundances of each grid of models are given in Table 2.1. The mixture of heavy elements used in each grid is assumed to be the same as that used in Ekström et al. (2012), with the absolute abundances scaled to the metallicity considered. The nuclear reaction rates are mainly taken from the NACRE database (Angulo et al., 1999), though some have been updated as detailed in Ekström et al. (2012).

Table 2.1: The initial abundances of H (X), He (Y) and metals (Z) as mass fractions.

Z	X	Y
0.00001	0.7516	0.2484
0.002	0.747	0.251
0.006	0.738	0.256
0.014	0.72	0.266
0.02	0.7064	0.2735

2.2.1 Mass loss

The fate of a massive star depends strongly on the mass loss experienced throughout its life (Meynet et al., 2015; Georgy, 2012). It is not modelled explicitly within the code, rather a series of empirical and theoretical prescriptions are employed at different domains to give the mass loss rate of the star. Particular mass loss events are therefore not included within the model, but a series of average rates are used across the evolution of the star. For a given point in the HR diagram, the use of different mass loss prescriptions can give drastically different results and so it is important to note the choice of mass loss prescriptions within the code and where each one acts. It is also important to highlight the uncertainties in these prescriptions and how this may affect predictions of remnant and supernova type. Fig. 2.1 summarises the domains where each mass loss prescription is used (note only massive star models with $M_{\rm ini} \geq 9\ M_\odot$ are considered in this work). On the main sequence, the mass loss rate from Vink et al. (2001) is used in the domains where it is valid and that from de Jager et al. (1988) is used elsewhere. The formula from Reimers (1975) is used for RSG under 12 $M_\odot$ and that from de Jager et al. (1988) is used again for stars above 15 $M_\odot$ with $\log T_{\rm eff} > 3.7$. When $\log T_{\rm eff} \leq 3.7$, a fit of the data from van Loon et al. (1999) and Sylvester et al. (1998) is used (Crowther, 2000). Wolf-Rayet (WR) stars are characterised by having $\log T_{\rm eff} > 4$ and a surface hydrogen fraction $X_{\rm H} < 0.3$ and their mass loss rates depend strongly on the Eddington factor, given by Eq. (2.6) (Ekström, 2021).

$$\Gamma_{\rm Edd} = \frac{L}{L_{\rm Edd}} = \frac{\kappa L}{4\pi c G M} \tag{2.6}$$

Within the code, these mass loss rates are given by Nugis and Lamers (2000) or Gräfener and Hamann (2008) (see Fig. 2.1 for the domains). When the Vink et al. (2001) rate is higher than that given by Gräfener and Hamann (2008), it is used instead. Note that there are newer mass loss prescriptions available, but those described above are used consistently throughout the grids of models to ensure that their properties can be directly compared (see the Vink (2022) review for more detail on newer prescriptions). For example, the new prescription from Yang et al. (2023) for highly luminous RSG has been developed using results from a spectroscopic survey of the SMC. Furthermore, the rates of mass loss experienced by stars at low metallicity that are close to the Eddington limit are very uncertain, but have a significant impact on the advanced stages of evolution

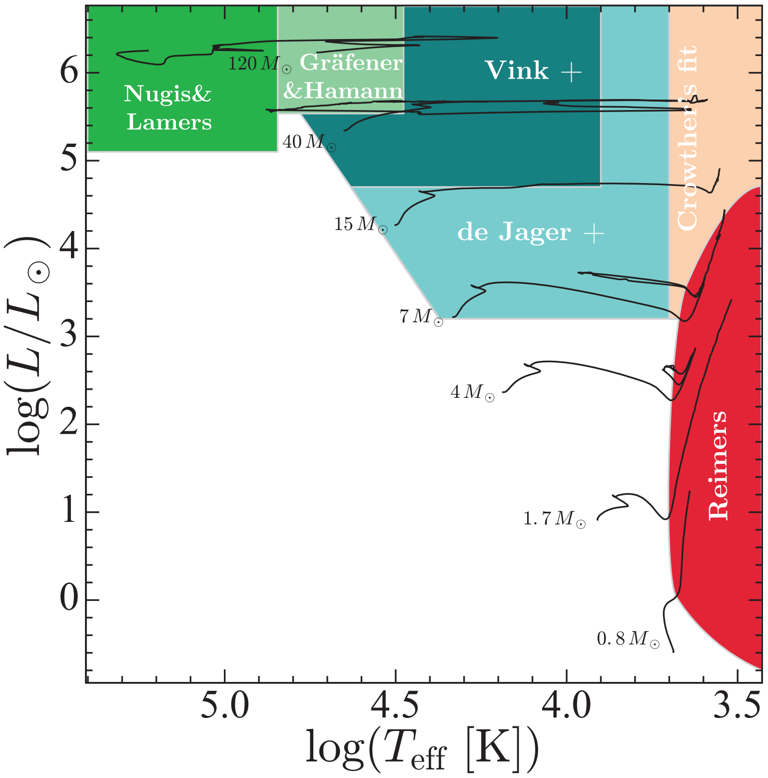

Figure 2.1: Domains where various prescriptions of mass loss rates are applied in the HR diagram. Taken from Eggenberger et al. (2021) (Fig. 1).

and determination of the fate of the star (Sander and Vink, 2020). Despite this, such uncertainties are thought to affect stars at higher luminosity and temperature less and so may not be significant when considering (very) massive stars (Björklund et al., 2023). It is important to note that even though new prescriptions are available, other recent grids of models also still use the same rates as described above (Fragos et al., 2023; Song and Liu, 2023). Radiative mass loss has a metallicity dependence given by Eq. (2.7).

$$\dot{M}(Z) = \dot{M}(Z_\odot)(Z/Z_\odot)^\alpha \tag{2.7}$$

where $\alpha = 0.85$ is used for the O-type phase and WN phase, $\alpha = 0.66$ for the WC and WO phases, and $\alpha = 0.5$ is used for the de Jager et al. (1988) prescription. When considering WR stars, the initial metallicity is used in this equation rather than the surface metallicity (Eldridge and Vink, 2006). It is important to note that the value of the exponent, α, is subject to uncertainties, as discussed in Mokiem et al. (2007). This dependence does not appear to apply to RSG, as their mass loss has been found to have a very weak dependence on metallicity, and so no metallicity scaling is applied when $\log T_{\text{eff}} \leq 3.7$ (van Loon et al., 2005).

Rotating models at lower metallicity retain more mass and angular momentum and so are more likely to have a surface velocity reaching the critical velocity, where the gravitational acceleration is balanced by the centrifugal force and mechanical mass loss occurs. This does not occur to a significant degree in the models considered in this work with $Z > 10^{-5}$, and at this metallicity the critical velocity is only reached in models with $M_{\text{ini}} \geq 40\ M_\odot$. Even though mass loss occurs at the surface, it can have consequences throughout the star. When mass loss is high on the main sequence the structure of the star can be changed significantly, and this can result in lower core masses. This leads to different nucleosynthetic conditions in the later stages of evolution, perhaps leading to different yields and changing the fate of the star. When mass loss is high past the main sequence, the envelope of the star can be removed, possibly leaving a bare core as early as the end of helium burning. If this does happen, there is no possibility of hydrogen shell burning and so the mass of the CO core cannot increase, it can only decrease further. Hence, *when* the mass loss happens during the evolution of the star can affect its fate. It is important to acknowledge that the mass loss rates discussed in this section are a major source of uncertainty in this work.

2.2.2 Rotation

It is widely known that stars rotate, and extensive observational data showing this is available (Evans et al., 2005; Dufton et al., 2006; Howarth et al., 1997; Conti and Ebbets, 1977). Typically, stars have equatorial velocities of ~ 200 km s^{-1} (Fukuda, 1982). The rotating models in this work start on the ZAMS with a value of $v_{\rm ini}/v_{\rm crit} = 0.4$ (Ekström et al., 2012). This value is chosen as it aligns with the peak of the velocity distribution of young B stars in Huang et al. (2010). This rotation has many effects, such as increased mechanical mass loss due to the non-spherical nature of rotating star, whereby the outer layers are not bound as tightly due to the weaker gravity at the equator (see Section 2.2.1). For rotating models, a correction factor is applied to the mass loss rate as per Maeder and Meynet (2000a) (also see Ekström et al. (2012) for implementation within the code). The centrifugal force helps to balance the star's gravity, which also has consequences for the hydrostatic equilibrium, playing an especially important role in the advanced evolution of massive stars (Endal and Sofia, 1978). Hence, rotating stars act like those with higher mass that do not rotate. In the HR diagram, this is shown by rotating tracks generally being shifted towards lower effective temperature and higher luminosity.

The shellular-rotation hypothesis is employed within the code, whereby the turbulence along an isobar is strong as the restoring force of the density gradient (buoyancy) acts in the vertical direction, and so there is no restoring force in the horizontal direction (see Zahn (1992) for more detail). Rotation also drives internal mixing and allows for the transport of angular momentum throughout the evolution of a star, due to instabilities such as meridional circulation and shear instabilities. This mixing also increases the size of the convective core at any given point in the evolution, and so has a significant impact on the predictions of fate made in this work.

As per the von Zeipel theorem (von Zeipel, 1924), a rotating star experiences different amounts of heating in the polar and equatorial directions, driving a large-scale circulation (Eddington, 1925; Sweet, 1950). The timescale for mixing from this circulation is shorter than the main-sequence lifetime, and so rotating stars experience mixing in radiative zones (Schwarzschild, 1958). The effects of this meridional circulation and the horizontal turbulence can be combined to give an effective diffusion coefficient, given by Eq. (2.8) from Chaboyer and Zahn (1992).

$$D_{\mathrm{eff}} = \frac{1}{30}\frac{|rU(r)|^2}{D_{\mathrm{h}}}, \tag{2.8}$$

where $U(r)$ is the vertical component of the meridional circulation velocity and D_{h} is the horizontal diffusion coefficient. Shear turbulence at the boundary of layers with different rotational velocities is also an effective mixing process. If excess kinetic energy from the differential rotation is less than the buoyancy force the layer remains stable (Chandrasekhar, 1961); that is, when the Richardson number is greater than a critical value, given by Eq. (2.9) from Maeder and Meynet (2000b).

$$Ri = \frac{N^2}{(\frac{dV(r)}{dr})^2} > Ri_{\mathrm{cr}} = \frac{1}{4}, \tag{2.9}$$

where N^2 is the Brunt-Väisälä frequency (buoyancy frequency) and $V(r)$ is the horizontal component of the meridional circulation velocity. Thermal dissipation reduces the buoyancy force, and so the shear instability occurs with greater ease (Endal and Sofia, 1978). The shear turbulence coefficient, D_{shear} used within the code can be found in Maeder (1997). The transport of angular momentum within the star obeys Eq. (2.10) from Zahn (1992).

$$\rho \frac{d}{dt}(r^2\Omega)_{M_r} = \frac{1}{5r^2}\frac{\partial}{\partial r}(\rho r^4 \Omega U(r)) + \frac{1}{r^2}\frac{\partial}{\partial r}\left(\rho D r^4 \frac{\partial \Omega}{\partial r}\right), \tag{2.10}$$

where $\Omega(r)$ is the mean angular velocity at r, D is the total diffusion coefficient in the vertical direction, and the first term gives the divergence of the advected flux and the second term gives the divergence of the diffused flux. If $U(r)$ and D are both zero, the local conservation of angular momentum is recovered, that is $r^2\Omega = c$ where c is a constant for a fluid element. The transport of chemical elements can be treated similarly to this (Heger et al., 2000; Maeder and Meynet, 2000b; Endal and Sofia, 1978), but the transport can be treated as a diffusive process with coefficient D_{eff} (see Eq. (2.8)) with the change in mass fractions given by Eq. (2.11) from Ekström et al. (2012).

$$\frac{dX_i}{dt} = \frac{1}{r^2}\frac{\partial}{\partial r}\left(\rho r^2 [D + D_{\text{eff}}] \frac{\partial X_i}{\partial r}\right) + \left(\frac{dX_i}{dt}\right)_{\text{nuc}}, \tag{2.11}$$

where X_i is the abundance of element i, D is the total diffusion coefficient in the vertical direction as per Eq. (2.10), and the final term gives the change in chemical abundance due to nuclear reactions.

The conservation of angular momentum throughout the evolution of the star is important as the final angular momentum of the star directly impacts its fate (Yoon et al., 2006). In the code, total angular momentum varies due to mass loss (stellar winds carry away momentum) as well as a numerical variation on which a correction, q_{corr}, is applied (Ekström et al., 2012). This variation is due to the structure of the code itself, whereby the envelope is floating over the interior layers (Kippenhahn et al., 1967).

The envelope is assumed to rotate at the same angular velocity as the shell of the interior at the boundary to the envelope, and so its angular momentum depends on the interior. This means that for the total angular momentum to remain constant, a correction must be applied. The expected final angular momentum at the end of the nth time step is given by Eq. (2.12).

$$\mathcal{L}_{\mathrm{fin}}^{\mathrm{exp}} = \mathcal{L}_{\mathrm{ini}} - \Delta\mathcal{L}_{\mathrm{winds}} \tag{2.12}$$

where $\mathcal{L}_{\mathrm{ini}}$ is the initial total angular momentum at time step $n-1$ and $\Delta\mathcal{L}_{\mathrm{winds}}$ is the total amount of angular momentum carried away by stellar winds.

This is usually different to the final angular momentum obtained, $\mathcal{L}_{\mathrm{fin}}^{\mathrm{ob}}$, and so a correction given by Eq. (2.13) is necessary.

$$\Delta\mathcal{L}_{\mathrm{corr}} = \mathcal{L}_{\mathrm{fin}}^{\mathrm{ob}} - \mathcal{L}_{\mathrm{fin}}^{\mathrm{exp}} \tag{2.13}$$

This correction is applied through the correction factor, q_{corr}, given by Eq. (2.14), from Ekström et al. (2012).

$$q_{\mathrm{corr}} = \frac{\Delta\mathcal{L}_{\mathrm{corr}}}{\mathcal{L}_{\mathrm{e}} + \sum_{i=1}^{N_{\mathrm{corr}}} \mathcal{L}_{\mathrm{i}}}, \tag{2.14}$$

where $\mathcal{L}_{\mathrm{e}}$ and $\mathcal{L}_{\mathrm{i}}$ are the angular momenta of the envelope and ith interior shell, and the choice of N_{corr} is fixed.

2.2.3 Convection

Convective zones are determined using the Schwarzschild criterion, and the convective core is extended with an overshoot parameter $d_{\mathrm{over}}/H_P = 0.1$. Stars are inherently 3D objects, and so some phenomena cannot be replicated within 1D models. In the code, convection is parameterised and calibrated according to observational data within the models, not directly simulated. The mixing-length theory (Böhm-Vitense, 1958) is used, and one issue with this is that it does not determine where the convective boundary lies (Arnett et al., 2019). Thus, prescriptions based on simple linear-analysis are used. This introduces even more uncertainty, especially in post-MS evolution. This then affects predictions of pre-supernova structures, which is problematic as core collapse outcome is heavily dependent on the convective history (Ertl et al., 2016), especially that of O and Si burning shells (see Section 1.2.3 for a discussion of the advanced stages of evolution). Convection plays a pivotal role in both the evolution of massive stars and their fate, and so is one important source of uncertainty in this work.

2.3 Properties of the stellar models

The evolutionary tracks in the HR diagram of all models used in this work are given in Fig. 2.2, showing that the width of the main sequence band generally increases with the initial mass of the model at all metallicities. Rotating models are generally cooler (more red) and more luminous than non-rotating models with the same initial mass and metallicity. Rotation increases mixing (see Section 2.2.2), and so more metals are brought to the surface. The presence of more metals at the surface increases the opacity, leading to a cooler envelope due to increased photon absorption. As the metallicity increases, models at the same initial mass tend to become cooler (more red), again due to metals at the surface increasing the opacity. A higher metallicity also means that fewer photons leave the surface of the star, and so they have a lower luminosity. Hence, the most luminous models are those with high initial mass and low metallicity that rotate. Note that 'blue' models are defined as those with $\log T_{\rm eff} > 3.9$, 'red' models are defined as those with $\log T_{\rm eff} < 3.7$, and those in between are referred to as 'yellow'. The hook found between the end of hydrogen burning and the start of helium burning is less noticeable for models with lower metallicity. This is because the temperature of the core at the end of hydrogen burning is higher in stars with lower metallicity, and so less contraction is required to heat up the core and maintain energy generation, resulting in a smaller hook feature for lower metallicities. Models at very high mass with $Z > 0.002$ evolve almost vertically in the HR diagram, as shown in Fig. 2.2, evolving across a wide range of luminosities but with almost constant effective temperature. In these models, the convective core typically accounts for a large proportion of the mass of the star and the evolution is very similar for stars with $M > 150\ M_\odot$ and $Z > 0.002$, particularly with respect to effective temperature.

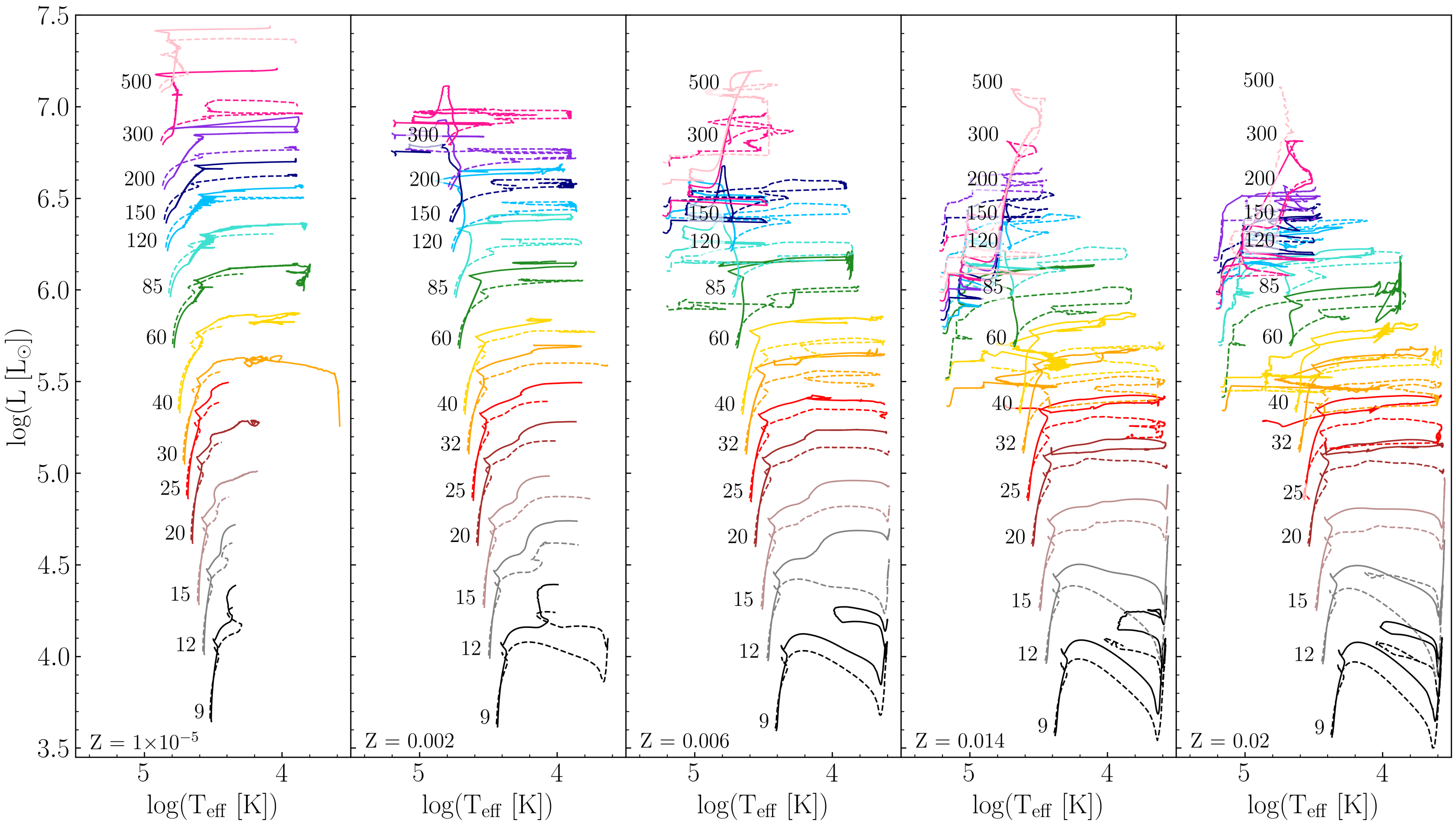

Figure 2.2: Evolutionary tracks in the HRD for rotating (solid line) and non-rotating (dashed line) models. Each track is labelled and colour coded with its initial mass.

The increased mixing in rotating models brings more hydrogen into the core, resulting in longer main sequence lifetimes at all initial masses and metallicities. This is not the case for the helium burning lifetime, as this tends to increase due to the convective core having a higher mass. See Ekström et al. (2012); Georgy et al. (2013); Yusof et al. (2013, 2022); Martinet et al. (2023); Sibony et al. (2024) for tables of main sequence and helium burning lifetimes at different metallicities. Models across the metallicities end helium burning as either blue, yellow or red supergiants (depending on their effective temperature), or as Wolf-Rayet stars (depending on their effective temperature and surface abundances). During the main sequence, the convective core mass gradually increases; in rotating stars this happens at a faster rate due to increased mixing. As initial mass increases, evolution on the $T_c - \rho_c$ diagram becomes more linear, see Ekström et al. (2012); Georgy et al. (2013); Yusof et al. (2013, 2022); Martinet et al. (2023); Sibony et al. (2024) for an in-depth discussion of evolution on the $T_c - \rho_c$ diagram. Mixing due to rotation means that rotating models have a higher core temperature and lower core density than their non-rotating counterparts.

2.3.1 Final total, envelope and core masses

The final total, envelope and core mass all have an impact on the fate of a massive star. The final mass is an indicator of the amount of mass lost throughout a star's life, and when coupled with the core and envelope masses it can be used to compare the impact of mass loss early and late in the evolution. The mass and composition of the envelope is crucial in determining the type of supernova explosion that may occur after collapse (see Section 1.2.4). Many factors affect the core, envelope and final mass: they do not increase monotonically with initial mass, as shown in Fig. 2.3 and 2.4. Note that the rotating model with $M_{\text{ini}} = 500\ M_\odot$, $Z = 0.02$ did not reach the end of hydrogen burning due to numerical issues. Data at this point is essential for the interpolation function used in Section 3.1, and it was assumed that the properties of this model would be the same as those of the rotating model at the same metallicity with $M_{\mathrm{ini}} = 300\ M_\odot$. As shown by Fig. 2.4, this is a reasonable assumption to make, as their properties of the rotating 300 $M_\odot$ and 500 $M_\odot$ models at $Z = 0.014$ also converge to a very similar value.

In this work, the final mass is defined as the total mass at the end of core helium burning, and is strongly dependent on the mass loss history of the model, and so is dependent on the metallicity of the model. Taking the final mass at the end of helium burning may seem premature, as the star will continue to evolve and burn carbon, neon, oxygen and silicon before reaching a true final mass. However, these advanced phases of evolution have much shorter lifetimes and so any mass loss experienced after this point is very small and thus assumed to be negligible. As a result, the true final mass of these models may be smaller than the final mass taken at the end of helium burning, as quoted in this work. Rotation generally decreases the final mass when initial mass and metallicity are held constant, due to the increased mass loss rates experienced by rotating models (see Section 2.2.1). Similarly, due to the metallicity dependence of mass loss on the main-sequence, an increase in metallicity results in a decrease in final mass. This is shown in Fig. 2.3 and 2.4, where both the rotating and non-rotating models with $Z = 10^{-5}$ have the highest final mass for all initial masses, and non-rotating models with $Z = 0.02$ have the lowest final mass for all initial masses. Rotating models generally have lower final masses due to the increased mass loss in rotating models. The significance of this effect increases with initial mass and metallicity until a peak at $Z = 0.006$, but at solar and supersolar metallicities, both non-rotating and rotating models experience significant post-MS mass loss and so there is less of a difference in final mass. In particular, rotating models with $Z = 0.02$ have the lowest final mass for initial masses below 85 $M_\odot$ (and at

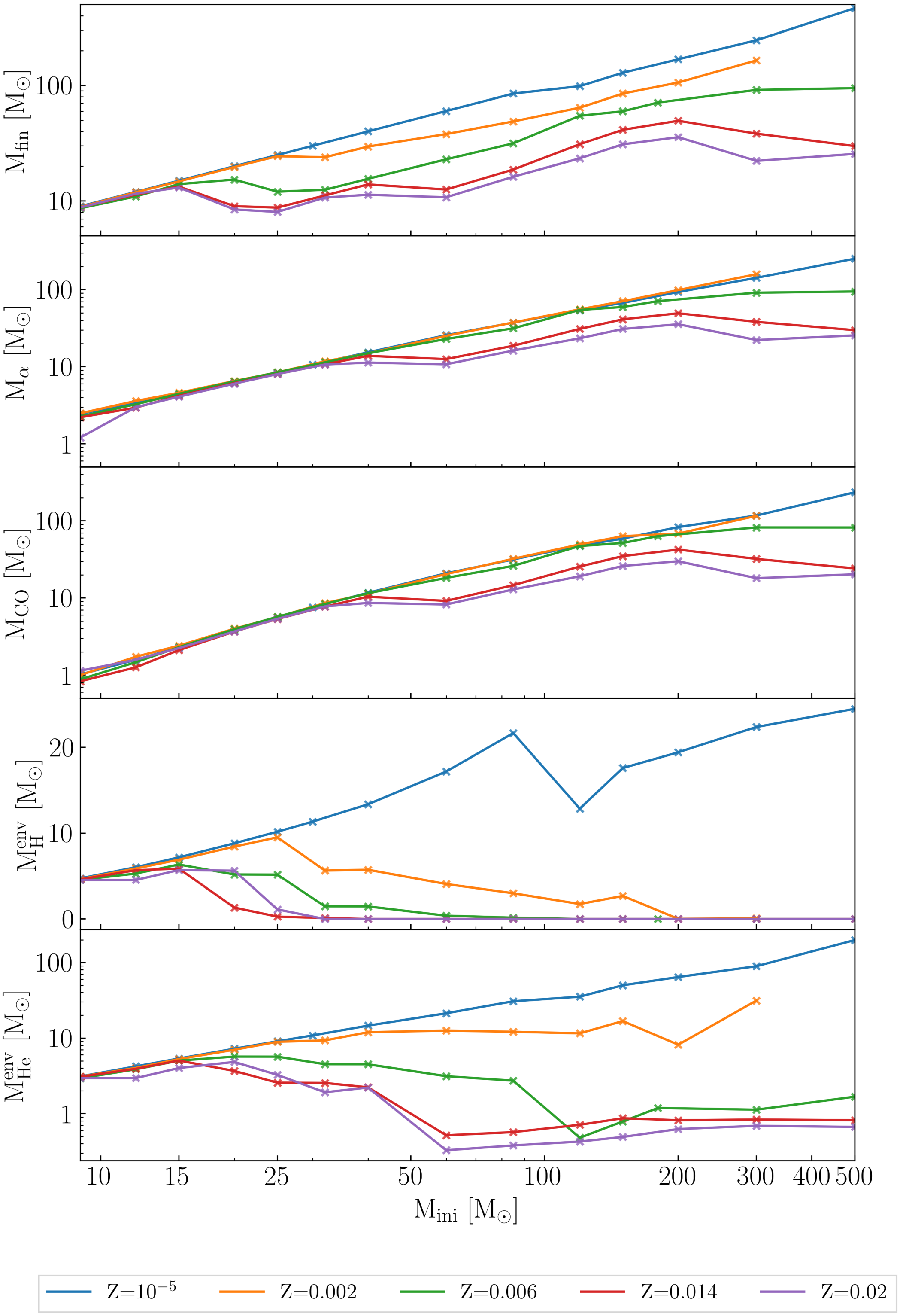

Figure 2.3: M_{fin}, M_α, M_{CO}, $M_{\mathrm{H}}^{\mathrm{env}}$ and $M_{\mathrm{He}}^{\mathrm{env}}$ as a function of initial mass for non-rotating models, determined at the end of core helium burning.

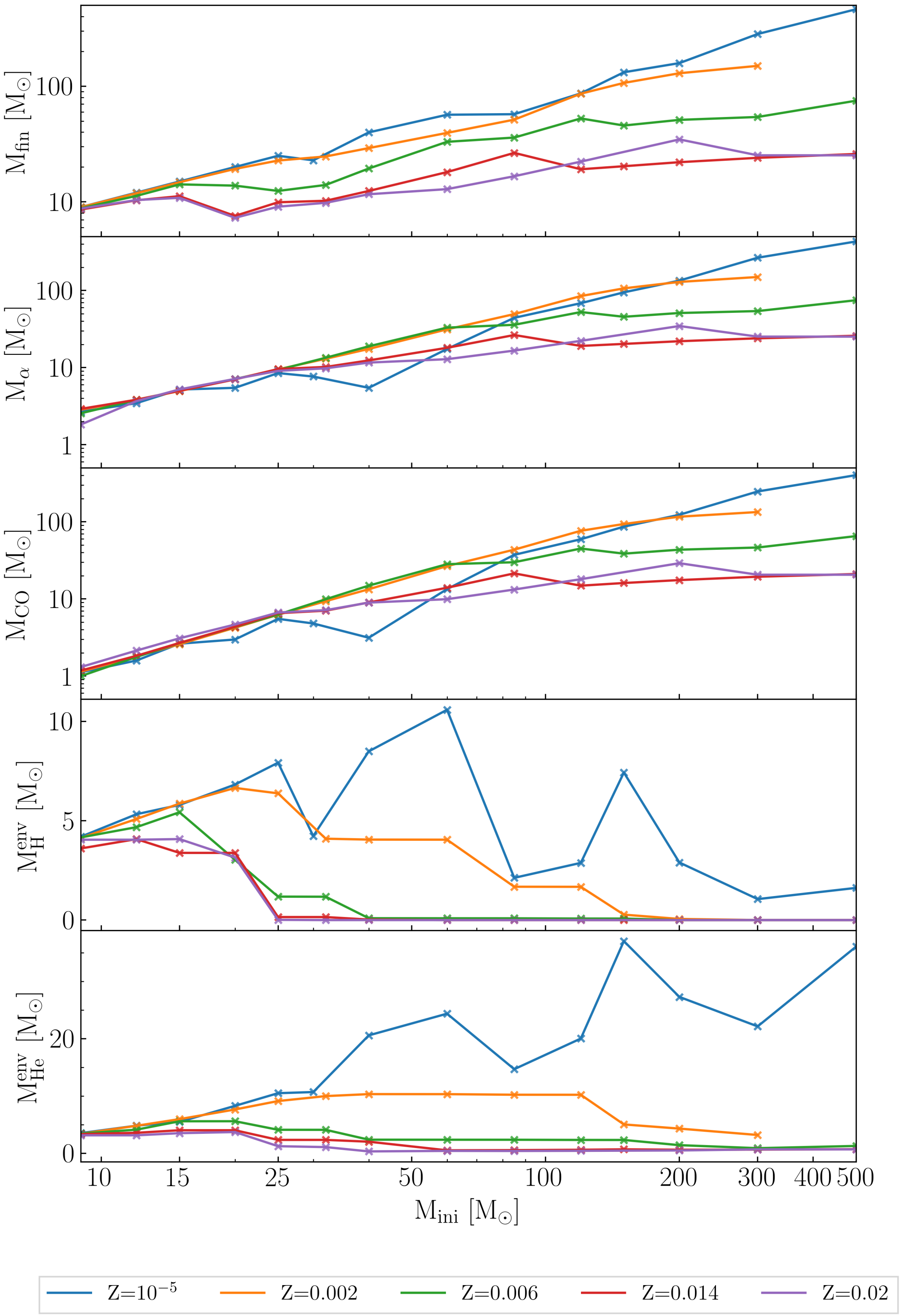

Figure 2.4: Same as Fig. 2.3 but for rotating models.

Table 2.2: $M_{\rm ini}$, $v_{\rm ini}/v_{\rm crit}$, and $M_{\rm CO}$ of selected models with $Z = 10^{-5}$. Taken from Table B.1, Appendix B.

$M_{\rm ini}$	$v_{\rm ini}/v_{\rm crit}$	$M_{\rm CO}$
30	0	7.57
30	0.4	4.81
40	0	11.67
40	0.4	3.14
60	0	20.94
60	0.4	13.42

500 $M_\odot$). Above 85 $M_\odot$, models with $Z = 0.014$ have the lowest final mass because they experience high rates of post-MS mass loss which is not dependent on the metallicity (Crowther, 2000).

The CO core mass is the main indicator of fate used in this work and so is of the highest significance. It is defined as the mass coordinate where the helium mass fraction falls below 1% and corresponds to the maximum convective core mass reached by the end of core helium burning. This mass coordinate marks the edge of the core, where there is a steep density gradient which eventually helps the supernova shock-wave to eject material above the edge of the core. It is important to note that there are other ways to define the CO core mass, such as the mass coordinate where the combined carbon and oxygen mass fraction is greater than 20%. This definition finds a CO core mass that lies in-between the alpha core mass and the CO core mass as defined in this work, and it can include the helium burning shell outside of the core. It is for this reason that this definition is not used in this case, as it may suggest that a star is helium free when it is not. Firstly, CO core masses of the non-rotating models (Fig. 2.3) will be considered. The CO core mass increases monotonically for non-rotating models with $M_{\rm ini} < 30$ $M_\odot$, across all of the metallicities considered. Above this initial

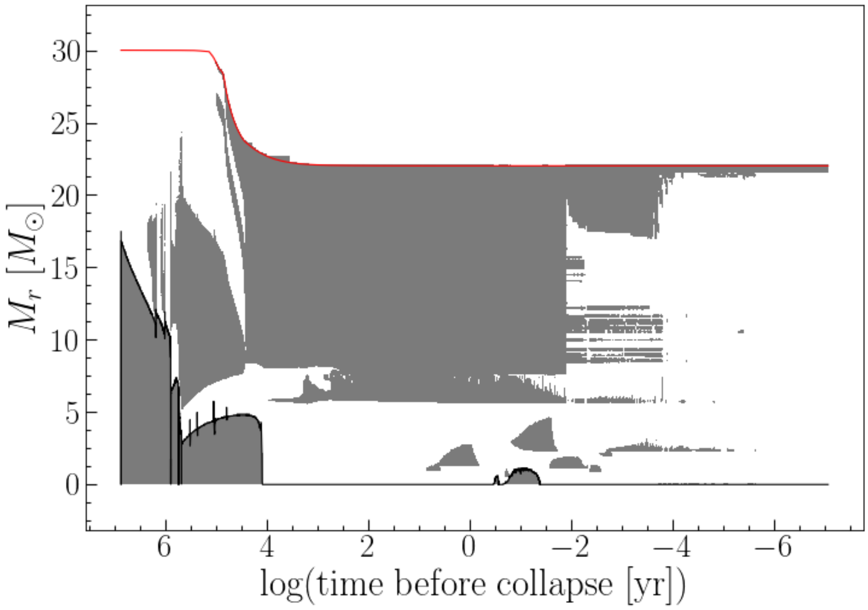

(a) 30 $M_\odot$

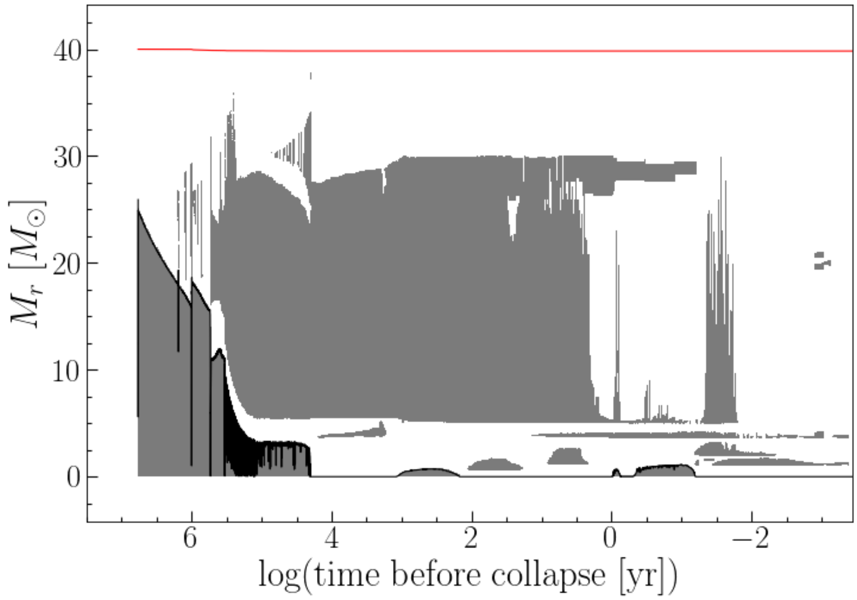

(b) 40 $M_\odot$

Figure 2.5: Kippenhahn diagrams for rotating models with $Z = 10^{-5}$.

mass, models use a variety of mass loss prescriptions across different stages of their evolution and mass loss is much stronger, so the CO core mass still increases with initial mass, but the relationship is no longer monotonic.

Additionally, there is a peak in CO core mass at solar and supersolar metallicity around 200 $M_{\odot}$, as shown in Fig. 2.3. This peak is due to the very high levels of post-MS mass loss experienced past this initial mass. With the exception of models at $Z = 10^{-5}$, the rotating models show a qualitatively similar relationship between CO core mass and initial mass as their non-rotating counterparts. At this metallicity, an unusual growth in the hydrogen burning shell causes a reduction in the CO core mass, as seen in Fig. 2.5. This effect can be seen in rotating models with $Z = 10^{-5}$ with initial mass $M_{\text{ini}} = 20 - 60\ M_{\odot}$ to varying extents (most noticeable in the 30 $M_{\odot}$ and 40 $M_{\odot}$ models shown in Fig. 2.5). They have significantly lower CO core masses than their non-rotating counterparts, as shown in Table 2.2. For $Z > 10^{-5}$, rotating models generally have a higher CO core mass, and the dependence of CO core mass on metallicity is less clear than that of final mass.

The H and He envelope masses are calculated by integrating the hydrogen or helium mass fraction throughout the star. Rotating models have a smaller hydrogen envelope mass for a given initial mass and they have a much smaller helium envelope mass across all metallicities. These relationships are much less monotonic than those for the final and CO core mass, suggesting that they are affected by a complex combination of many factors, including rotation, metallicity, mass loss and the extent of mixing. Rotating stars at both solar and supersolar metallicity with $M_{\text{ini}} \geq 25\ M_{\odot}$ are considered as 'H-poor', defined as stars with $M_{\text{H}}^{\text{env}} < 0.5\ M_{\odot}$ (see Section 3.3 for a discussion on this definition). For non-rotating stars at supersolar metallicity this is also the case, but those at

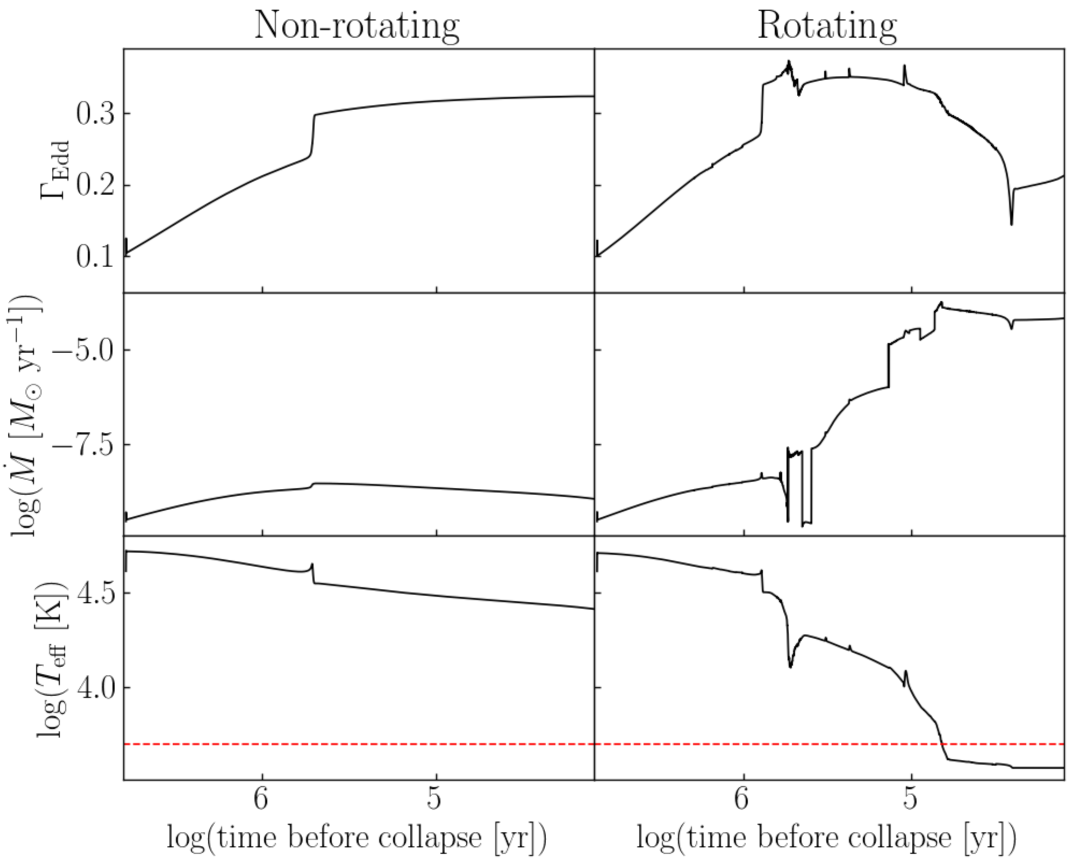

Figure 2.6: Comparison between Eddington factor, rate of mass loss and effective temperature of non-rotating and rotating models at 30 $M_\odot$ with $Z = 10^{-5}$. The red dashed line indicates the temperature below which the star is considered an RSG. Models taken from Sibony et al. (2024).

solar metallicity are considered H-poor when $M_{\rm ini} \geq 32\ M_\odot$. This difference is due to the increased post-MS mass loss rates experienced by rotating stars. At LMC metallicity, rotating stars with $M_{\rm ini} \geq 40\ M_\odot$ and non-rotating stars with $M_{\rm ini} \geq 60\ M_\odot$ are considered H-poor. Similarly, at SMC metallicity, rotating stars with $M_{\rm ini} \geq 150\ M_\odot$ and non-rotating stars with $M_{\rm ini} \geq 200\ M_\odot$ are considered H-poor, while both rotating and non-rotating stars at all initial masses with $Z = 10^{-5}$ retain their hydrogen envelope and so are considered 'H-rich'. The rotating model at $Z = 10^{-5}$ with $M_{\rm ini} = 30\ M_\odot$ evolves towards lower effective temperature during core helium burning than its non-rotating counterpart (see Fig. 2.6), and so experiences much higher mass loss due to the RSG prescription (Crowther, 2000). Fig. 2.6 also highlights that the Eddington factor is similar for both models, and so the large increase in mass loss is not due to exceeding the Eddington limit. This results in a smaller hydrogen envelope mass ($\sim 7\ M_\odot$ less than the non-rotating model) and so it also has a smaller final mass. Very few models become 'He-poor', defined as stars with $M_{\rm He}^{\rm env} < 0.5\ M_\odot$ (see Section 3.3 for a discussion on this definition). This has significant consequences when considering the supernova type of the models that are predicted to explode successfully, including PPISN and PISN.

Chapter 3

Determining the fate of massive stars

In Chapter 2, individual models were considered alongside the equations and numerical methods on which they are based, and the properties that they have. This analysis of the models forms the basis for the main results of this work, where the macroscopic properties of the combined grids of models are examined, and how their properties change in relation to rotation and metallicity. The properties of the models given in Chapter 2 can be analysed on a macroscopic level since they have consistent input physics. These properties and the following determination of fates allow for comparisons to be made between models and observations when combined with a suitable IMF. The results from this analysis are presented and discussed in this chapter, alongside a consideration of IMF choice.

3.1 Remnant type

The advanced phases of the evolution of massive stars are largely determined by the CO core mass and the abundance of ^{12}C at the end of core helium burning (Chieffi and Limongi, 2020; Patton and Sukhbold, 2020). In particular, the CO core mass is significant in determining the further evolution of the star, but the abundance of ^{12}C left after core helium burning is also informative as it determines the extent of both core and shell carbon burning phases. This mass fraction is not independent of the CO core mass (Chieffi and Limongi, 2020), and so will not be considered separately in this work. In order to relate the CO core mass to different remnant types, the compactness of the pre-supernova stellar core is often used; given by Eq. (3.1) evaluated at $M = 2.5\ M_\odot$ (O'Connor and Ott, 2011).

$$\xi_M = \frac{M/M_\odot}{R(M)/1000\text{km}} \tag{3.1}$$

The compactness is a non-monotonic function of the CO core mass, as shown in Fig. 3.1, and is important when considering the final fate of massive stars. From this, the CO core mass at the end of core helium burning can be used to predict the type of compact remnant left behind when a massive star dies - either a neutron star, black hole or no remnant in the case of PISN. In this work, remnant types are determined using the CO core mass alone as per Table 3.1.

Massive stars with $M_{\mathrm{CO}} < 6\ M_\odot$ are thought to explode successfully and form neutron stars (Patton and Sukhbold, 2020). O'Connor and Ott (2011) found that when $\xi_{2.5} > 0.45$, successful explosions are much less likely and there is a transition between neutron star and black hole formation. Similarly, Ugliano et al. (2012) found that there is a transition region between neutron star and black hole formation when $0.15 < \xi_{2.5} < 0.35$. There is a peak in compactness between $6 < M_{\mathrm{CO}} < 12\ M_\odot$ where the compactness increases and falls within this transition region, as per both Fig. 3.1 and Sukhbold and Woosley (2014). When $6 < M_{\mathrm{CO}} < 8\ M_\odot$, the compactness increases through the transition region given by Ugliano et al. (2012) and above the explodability limit suggested by O'Connor

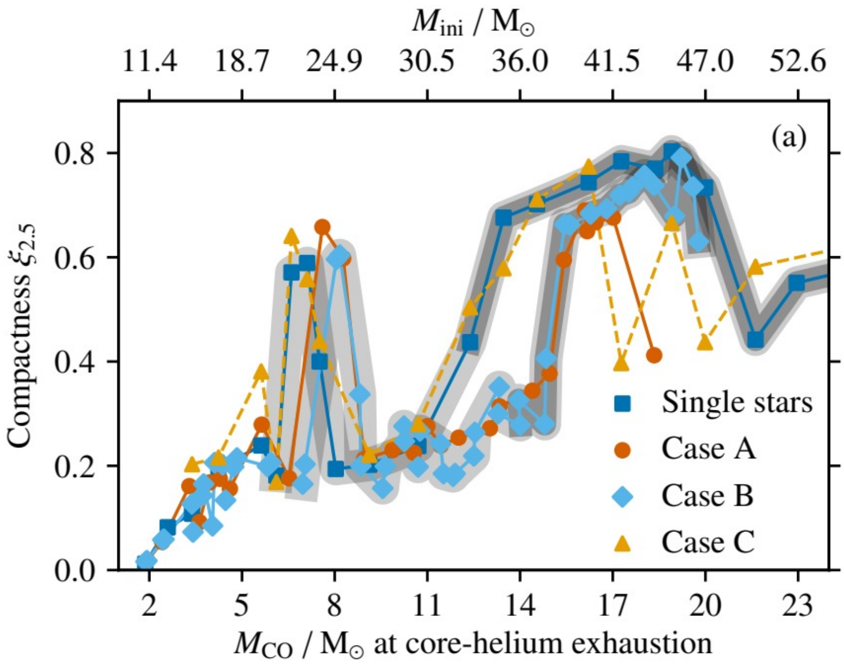

Figure 3.1: Compactness, $\xi_{2.5}$, at core collapse as a function of the CO core mass at the end of core helium burning, with blue squares indicating data from single star models. Taken from Schneider et al. (2021) (Fig. 5a).

and Ott (2011) and so such models are considered as unlikely to explode and these are expected to form black holes, with the possibility of a successful explosion to form a neutron star. Black holes formed within this transition mass range result from 'failed' explosions and so form by fallback. When $8 < M_{\rm CO} < 12\ M_\odot$, the compactness falls below the explodability limit into the transition region and so such models are likely to explode successfully and are expected to form neutron stars, with the possibility of a failed explosion leading to black hole formation. This 'island' of explodability is shown clearly in Fig. 13 of Sukhbold et al. (2016) and is also eluded to in O'Connor and Ott (2011). When $12 < M_{\rm CO} < 40\ M_\odot$, there is direct collapse to a black hole with $M_{\rm BH} = M_{\rm fin}$, such that there is no explosion (Patton and Sukhbold, 2020). Above $M_{\rm CO} = 40\ M_\odot$, stars are expected to undergo PPSIN followed by a core-collapse supernova, resulting in the formation of a black hole, and when $60 < M_{\rm CO} < 130\ M_\odot$ stars are expected to be fully disrupted in a PISN that leaves behind no remnant (Farmer et al., 2019).

Table 3.1: Dependency of remnant type on the CO core mass. PPISN refers to pulsation pair-instability supernovae and PISN refers to pair-instability supernovae.

	Remnant type
$M_{\mathrm{CO}} < 6\ M_{\odot}$	Neutron star
$6 < M_{\mathrm{CO}} < 8\ M_{\odot}$	Black hole (neutron star)
$8 < M_{\mathrm{CO}} < 12\ M_{\odot}$	Neutron star (black hole)
$12 < M_{\mathrm{CO}} < 40\ M_{\odot}$	Black hole
$40 < M_{\mathrm{CO}} < 60\ M_{\odot}$	PPISN with black hole
$60 < M_{\mathrm{CO}} < 130\ M_{\odot}$	PISN with no remnant
$M_{\mathrm{CO}} > 130\ M_{\odot}$	Black hole

Above this, the photodisintegration instability allows for direct black hole formation again (Heger et al., 2003). The CO core mass was calculated from each model in the ongoing series of grids as per the definition given in Section 2.3.1. Linear interpolation between these values across an evenly spaced grid of initial masses (with steps of 1 $M_{\odot}$) allows for analysis of the CO core mass across the whole mass range considered. This also fills gaps in the current grids of models by those which encountered numerical issues and did not reach the end of helium burning (see Table A.1). This interpolation was also performed on the final mass and H and He envelope masses of the models. In order to show how the CO core mass responds to changes in initial mass and metallicity, a contour map was plotted on the $M_{\mathrm{ini}} - Z$ plane, using CO core mass as the response variable. One difficulty with using contour maps is that any irregular data points may result in oversimplified relationships and missing features in the map, leading to less accurate representations of the underlying behaviour of the variables. Similarly, the use of linear interpolation may also result in missing features in the map. This is why it is also useful to refer back to the model data around interesting features in the contour map, given in Appendix B.

The contour boundaries used are given in Table 3.1, and it is important to note that the above assumptions mean that the behaviour of the variables may be less accurately represented at such boundaries, and that further analysis of these regions may be required to build an accurate picture of how the response variable is related to the independent variables.

3.1.1 Expected results

It is expected that stars with higher initial mass will generally have a higher CO core mass. This is, however, impacted greatly by both metallicity and rotation. It is expected that increasing the metallicity will lead to an increased rate of mass loss as per the relation given by Eq. (2.7). If this mass loss occurs early in the evolution, it will result in smaller helium core masses and so leading to a smaller CO core mass. The impact of rotation is more complex as it has competing effects on the evolution. Increased mixing leads to the formation of larger helium cores, and so larger CO core masses are expected. On the other hand, rotation also leads to higher luminosities and so higher rates of early mass loss (as well as mechanical mass loss). This would lead to smaller helium cores and so a decrease in CO core mass. And so, there are two competing effects that both result from including rotation in the models. The increase in CO core mass due to internal mixing tends to be the dominant effect at lower initial mass and metallicity, whereas the decrease due to increased mass loss tends to dominate at higher initial mass and metallicity. Hence, the results are expected to show an interesting combination of these effects.

3.1.2 Impact of metallicity

Firstly, the effect of changing initial mass and metallicity will be considered for non-rotating models. Fig. 3.2a shows the dependence of fate on initial mass and

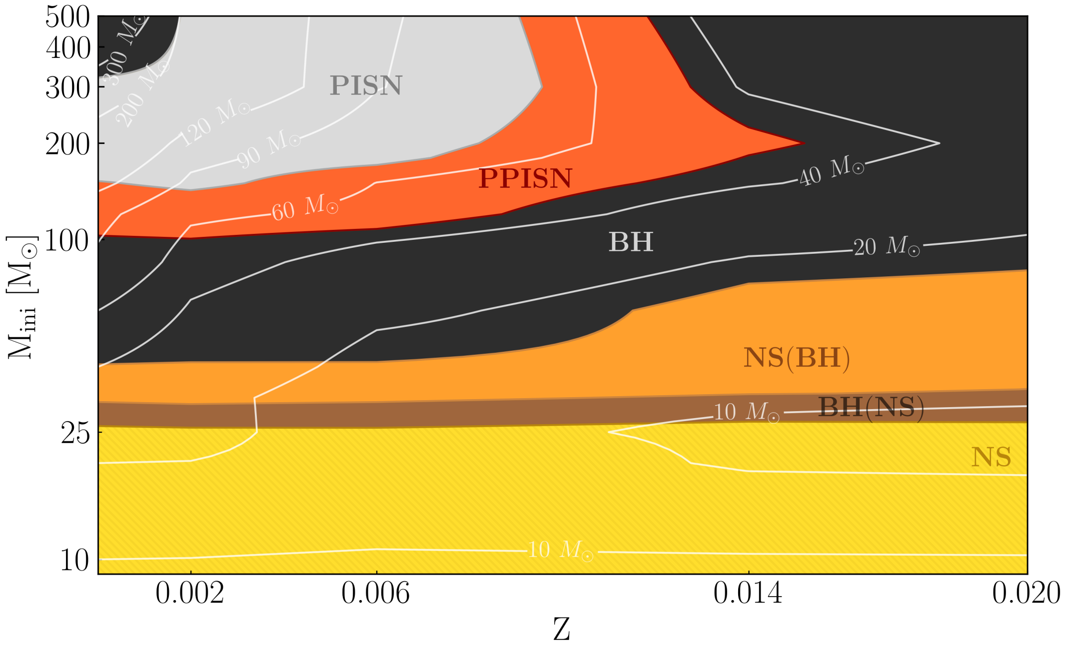

(a) Non-rotating

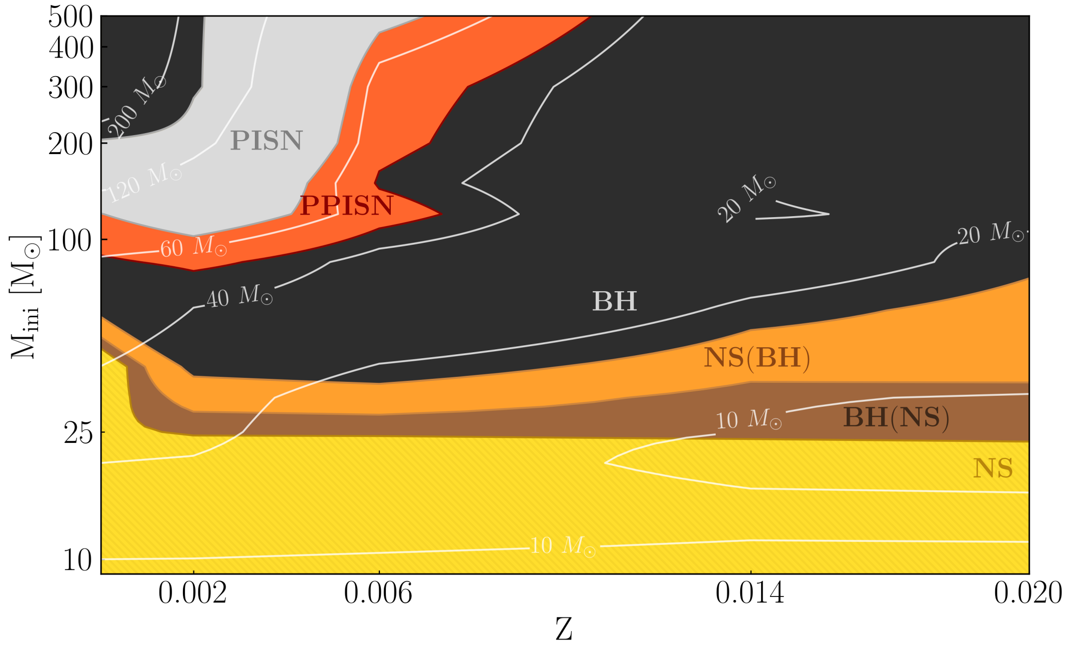

(b) Rotating

Figure 3.2: Remnant type as a function of initial mass and metallicity. The boundaries for each remnant type are given in Table 3.1, and the white contour lines indicate final mass.

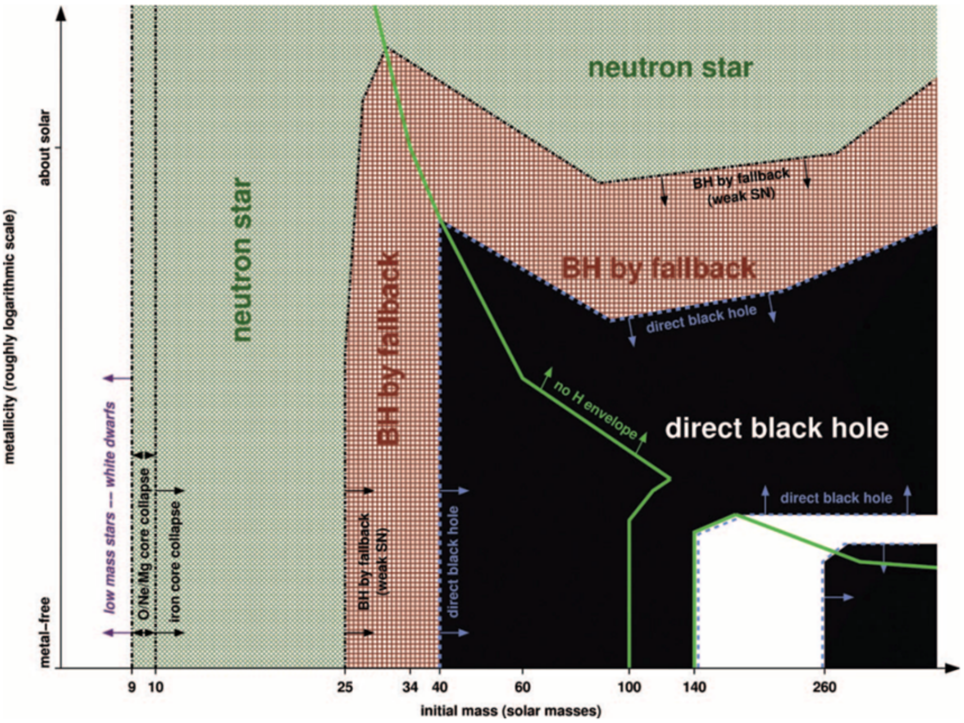

(a) Figure 1 from Heger et al. (2003).

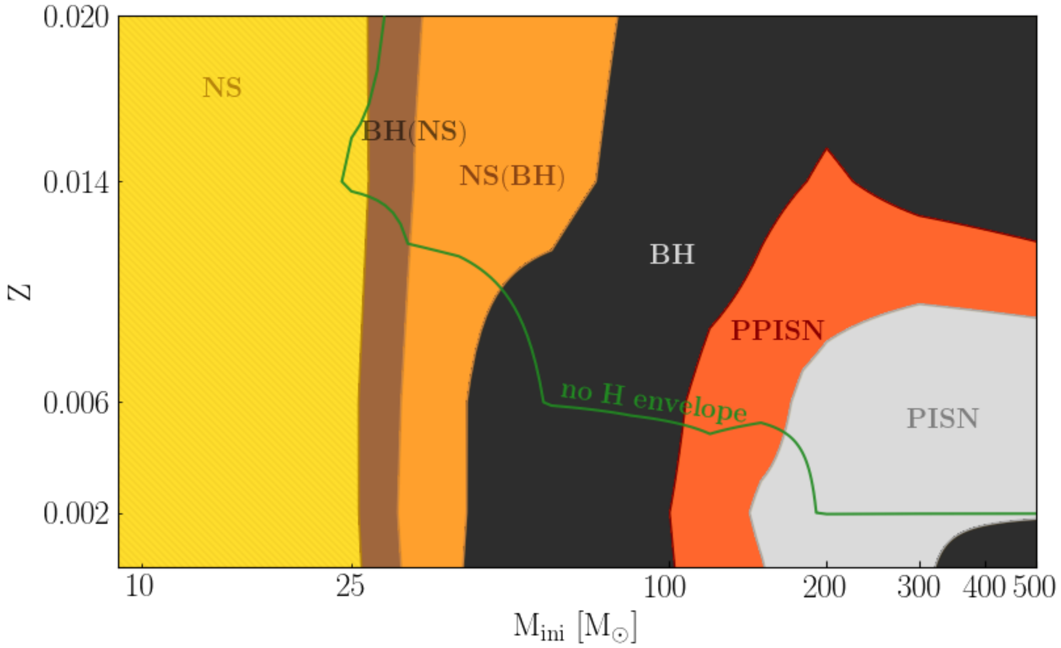

(b) Adapted from Figure 3.2a in this work.

Figure 3.3: Comparison of remnant type as a function of initial mass and metallicity between results from Heger et al. (2003) and this work.

metallicity for non-rotating models. When initial mass is low, i.e. $M_{\rm ini} < 40\ M_\odot$, the dependence of remnant type on metallicity is very limited. This is due to very low rates of mass loss, particularly early in the evolution. Hence, the CO core mass for a particular initial mass is constant across the range of metallicities considered in this work. Fig. 3.2a shows that stars with $M_{\rm ini} < 25\ M_\odot$ end their lives as neutron stars (NS), for the whole metallicity range considered. At higher initial mass, when $25 < M_{\rm ini} < 30\ M_\odot$, black holes via failed supernovae are expected, with the possibility of a successful explosion leading to a NS remnant, referred to as BH (NS) from this point (see Section 3.1). When $30 < M_{\rm ini} < 40\ M_\odot$, NS are expected but there is still the possibility of a black hole remnant, referred to as NS (BH) from this point. At higher initial mass, when $M_{\rm ini} > 40\ M_\odot$, the remnant type shows a strong dependence on metallicity. For example, the boundary between NS (BH) and direct black hole formation increases from $M_{\rm ini} = 41\ M_\odot$ when $Z = 10^{-5}$ to $M_{\rm ini} = 75\ M_\odot$ when $Z = 0.014$. The case of low metallicity ($Z < 0.001$) and high metallicity ($Z > 0.001$) will be considered separately for higher initial masses ($M_{\rm ini} > 40\ M_\odot$).

At low metallicity and high initial mass, the CO core mass remains high due to low rates of mass loss early in the evolution. Then, for $40 < M_{\rm ini} < 100\ M_\odot$, direct black holes are formed. As shown by the white contours on Fig. 3.2a, the maximum black hole mass below the pair-instability gap ranges from $M_{\rm BH} \approx\ 30 - 90\ M_\odot$ and so is highly dependent on metallicity; this is discussed further in Section 3.2. The upper boundary for black hole formation without encountering the pair-instability increases with metallicity and so has an upward slope in Fig. 3.2a, such that it is located at $M_{\rm ini} = 100\ M_\odot$ when $Z = 10^{-5}$, and $M_{\rm ini} = 140\ M_\odot$ when $Z = 0.01$. Likewise, the upper boundary for PPISN forming black holes below the PISN gap is also dependent on metallicity, such that it is located at $M_{\rm ini} = 150\ M_\odot$ when $Z = 10^{-5}$, and $M_{\rm ini} = 300\ M_\odot$ when $Z = 0.01$. When

$Z < 0.002$, PISN are predicted from this boundary until $M_{\rm ini} = 325\ M_\odot$ above which direct black hole formation is predicted once again. When $Z > 0.002$, PISN are predicted up to $M_{\rm ini} = 500\ M_\odot$, which is the highest mass considered in this work. At high metallicity and high initial mass, the CO core mass decreases as metallicity increases (assuming constant initial mass). This is because mass loss early in the evolution becomes significant, as these models evolve at higher luminosities than their lower mass counterparts; this effect is scaled with metallicity as per Eq. (2.7). The boundary between NS (BH) and direct black hole formation lies between $50 < M_{\rm ini} < 80\ M_\odot$ depending on the metallicity. Above this, models result in direct collapse to black holes, and when $Z > 0.014$ this is the case for all models in this region. Finally, PPISN are predicted at $Z < 0.014$ in the region of $M_{\rm ini} = 200\ M_\odot$, as shown on Fig. 3.2a.

Comparison to Heger et al. (2003)

Fig. 3.3a and 3.3b show a comparison between this work and that of Heger et al. (2003). Both show qualitatively similar results but the key differences are considered in this section. There are significant differences in the models used in Heger et al. (2003) and this work, such as different mass loss prescriptions and the inclusion of models with $Z = 0$. The newer mass loss prescriptions used in this work lead to lower rates of mass loss, which leading to larger CO core masses for high mass stars at high metallicity in particular. It is also important to note that the ‘black hole by fallback’ remnant type category from Heger et al. (2003) encompasses both the BH (NS) and NS (BH) remnant type categories used in this work, both referring to the possibility of a failed supernova explosion. One key difference between the plots given in Fig. 3.3 is the absence of NS at high metallicity for $M_{\rm ini} > 25\ M_\odot$ in Fig. 3.3b, which is due to the difference in mass loss prescriptions. Similarly, this is also the reason for the absence of BH (NS) and NS (BH) above $M_{\rm ini} = 75\ M_\odot$ in Fig. 3.3b. Additionally, Heger et al. (2003)

Table 3.2: Dependency of remnant type on the helium core mass as per Heger et al. (2003).

	Remnant type
$M_\alpha < 8\ M_\odot$	Neutron star
$8 < M_\alpha < 15\ M_\odot$	Black hole by fallback
$15 < M_\alpha < 65\ M_\odot$	Black hole
$65 < M_\alpha < 135\ M_\odot$	No remnant
$M_\alpha > 135\ M_\odot$	Black hole

use the helium core mass to determine remnant type, as per Table 3.2, instead of the CO core mass. It is acknowledged by Heger et al. (2003) that the CO core mass may be a better determinant of fate, hence the its use in this work. See Section 3.1 for a discussion on use of the CO core mass to determine remnant type.

The results from Heger et al. (2003) suggest that stars at low metallicity with $100 < M_{\rm ini} < 140\ M_\odot$ lose their hydrogen envelope due to the use of helium star models at $Z = 0$, whereas all models in this work at EMP metallicity (regardless of their initial mass) retain a significant amount of their hydrogen envelope. The upper metallicity limit of $Z \approx 0.01$ for PISN is significantly higher in this work than in that of Heger et al. (2003), due to the factors discussed above, and PPISN are not considered separately to direct black holes. It is also important to note that only non-rotating models were considered in Heger et al. (2003), and so comparisons cannot be drawn with results from the rotating models of this work.

3.1.3 Impact of rotation

The impact of rotation can be seen in Fig. 3.2, and differs depending on both initial mass and metallicity, due to the competing effects that rotation has on the

CO core mass. The results on the $M_{\rm ini} - Z$ plane will be separated into four cases depending on the initial mass and metallicity, where the dominant effect due to rotation differs.

Case 1: low initial mass, very low metallicity

When $M_{\rm ini} < 60\ M_\odot$ and $Z < 0.002$, Fig. 3.2b differs significantly from the same region in Fig. 3.2a. Firstly, unusual growth in the hydrogen burning shell, as seen in Fig. 2.5 and discussed in Section 2.3.1, causes a decrease in CO core mass at $Z = 10^{-5}$, up until $Z = 0.002$. This effect is strongest around 40 $M_\odot$, but can be seen in many models at EMP metallicity. This causes the boundary for NS, BH (NS) and NS (BH) to increase in initial mass when compared to the non-rotating case, where this effect is not seen, introducing a negative slope to the boundary (which is flat in Fig. 3.2a). Hence, more stars are predicted to form NS, BH (NS) and NS (BH) than in the non-rotating case in this region. This is *not* due to increased rates of mass loss (as one might expect), but is because of an interesting effect of rotation on the hydrogen burning shell (see Section 2.3.1). The final mass contours in Fig. 3.2a and 3.2b are very similar as increased mass loss is not the dominant effect of rotating in this region, and so both rotating and non-rotating models experience similar rates of mass loss.

Case 2: low initial mass, higher metallicity

When $M_{\rm ini} < 60\ M_\odot$ and $Z > 0.002$, the dominant effect of rotation is increased mixing, leading to higher CO core masses when compared to results from Fig. 3.2a. This causes the boundary between NS (BH) and direct black hole formation to generally decrease in initial mass when compared to the non-rotating case. Similarly to the non-rotating case, the boundary increases to higher initial mass as metallicity increases due to the fact that CO core mass generally decreases with increasing metallicity in this region of Fig. 3.2b. In the rotating case, this increase is seen as a gentle upward slope in Fig. 3.2b, unlike the sharp increase and plateau seen in Fig. 3.2a. Again, the final mass contours are very similar between Fig. 3.2a and 3.2b in this region, since the rates of mass loss are not greatly impacted by rotation at low initial mass.

Case 3: high initial mass, very low metallicity

When $M_{\rm ini} > 60\ M_\odot$ and $Z < 0.002$, the dominant effect of rotation is also increased mixing, leading to higher CO core masses when compared to results from Fig. 3.2a. When $Z = 10^{-5}$, direct black holes are formed for $60 < M_{\rm ini} < 90\ M_\odot$. The lower boundary of this mass range is significantly higher than that in the non-rotating case ($M_{\rm ini} = 40 M_\odot$) due to the interaction between the hydrogen burning shell and helium burning core. The upper boundary is lower in the rotating case due to an increase in CO core mass due to internal mixing.

The maximum black hole mass below the pair-instability gap ranges from $M_{\rm BH} \approx 35 - 60\ M_\odot$, which is discussed further in Section 3.2. The lower boundary of this mass range is lower than in the non-rotating case due to the hydrogen burning shell effect (see Section 2.3.1), and the upper boundary is significantly lower than in the non-rotating case due to increased mixing.

Case 4: high initial mass, higher metallicity

When $M_{\rm ini} > 60\ M_\odot$ and $Z > 0.002$, the dominant effect of rotation is increased mass loss. The metallicity boundaries for PPISN and PISN are lower for rotating models and when $Z > 0.01$, only direct black holes and NS (BH) are predicted in this region. When compared to the same region in Fig. 3.2a, the impact of rotation can be seen by the decreased final masses (and so lower black hole masses; see Section 3.2).

Table 3.3: Number of stars per mass range, calculated using the Salpeter IMF (Salpeter, 1955) such that there is one star with $M = 500\ M_{\odot}$, and the top-heavy IMF (Schneider et al., 2018) calculated such that the total population is of the same size.

	$9 - 30\ M_{\odot}$	$30 - 100\ M_{\odot}$	$100 - 300\ M_{\odot}$	$> 300\ M_{\odot}$	Total
Salpeter	74375	12929	2495	367	90166
Top-heavy	63202	19300	6286	1378	90166

3.1.4 Fraction of massive stars per remnant type

In order to place the above results in the context of a population of stars, they must be weighted according to the IMF. The distribution of remnants depends on the regions identified in Fig. 3.2 and also the choice of IMF. For this reason, this distribution has been calculated for two different initial mass functions: the Salpeter IMF (Salpeter, 1955) with results given in Table 3.4 and the top-heavy IMF from Schneider et al. (2018) with results given in Table 3.5. The distributions were calculated such that there is one star with $M_{\text{ini}} = 500\ M_{\odot}$ in the Salpeter IMF distribution, with a total population of 90166 massive stars, as per Table 3.3. Then, the top-heavy mass distribution was calculated such that the population size remained the same as that calculated using the Salpter IMF. In this case, there are 4.3 stars with $M_{\text{ini}} = 500\ M_{\odot}$, illustrating the top-heavy nature of this IMF when compared to the Salpeter IMF. The number of stars in different mass ranges is given in Table 3.3 for both IMF variations. As expected, this shows that the mass distribution calculated using the Salpeter IMF has more stars with mass between $9 - 30\ M_{\odot}$. The opposite is true above this mass; the mass distribution calculated using the top-heavy IMF has more stars in the $30 - 100\ M_{\odot}$, $100 - 300\ M_{\odot}$ and $> 300\ M_{\odot}$ categories than that calculated

Table 3.4: Fraction of massive stars per remnant type, calculated using the IMF from Salpeter (1955) with $\alpha = 2.35$.

Z	NS	NS (BH)	Total NS	BH (NS)	BH	Total BH	PPISN	PISN
Non-rotating								
10^{-5}	0.787	0.049	0.836	0.045	0.091	0.136	0.014	0.013
0.002	0.776	0.061	0.837	0.049	0.082	0.131	0.013	0.018
0.006	0.776	0.053	0.829	0.057	0.086	0.143	0.015	0.013
0.014	0.787	0.109	0.896	0.052	0.048	0.100	0.004	0
0.02	0.787	0.103	0.890	0.065	0.044	0.109	0	0
Rotating								
10^{-5}	0.900	0.017	0.917	0.011	0.043	0.054	0.014	0.014
0.002	0.763	0.061	0.824	0.044	0.091	0.135	0.014	0.026
0.006	0.763	0.050	0.813	0.044	0.117	0.161	0.024	0.001
0.014	0.749	0.060	0.809	0.109	0.082	0.191	0	0
0.02	0.749	0.093	0.842	0.109	0.049	0.158	0	0

Table 3.5: Fraction of massive stars per remnant type, calculated using the top-heavy IMF from Schneider et al. (2018) with $\alpha = 1.9$.

Z	NS	NS (BH)	Total NS	BH (NS)	BH	Total BH	PPISN	PISN
				Non-rotating				
10^{-5}	0.657	0.064	0.721	0.053	0.156	0.209	0.033	0.037
0.002	0.644	0.079	0.723	0.057	0.135	0.192	0.030	0.055
0.006	0.644	0.069	0.713	0.066	0.142	0.208	0.036	0.043
0.014	0.657	0.158	0.815	0.062	0.112	0.174	0.011	0
0.02	0.657	0.155	0.812	0.078	0.110	0.188	0	0
				Rotating				
10^{-5}	0.799	0.026	0.825	0.016	0.093	0.109	0.029	0.036
0.002	0.630	0.076	0.706	0.050	0.151	0.201	0.028	0.065
0.006	0.630	0.062	0.692	0.050	0.189	0.239	0.066	0.003
0.014	0.615	0.084	0.699	0.128	0.173	0.301	0	0
0.02	0.615	0.140	0.755	0.128	0.118	0.246	0	0

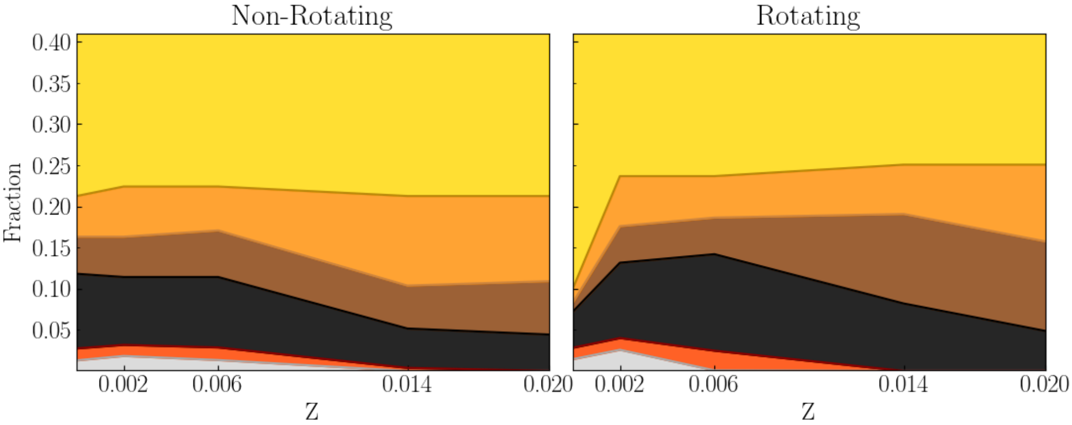

(a) Salpeter IMF.

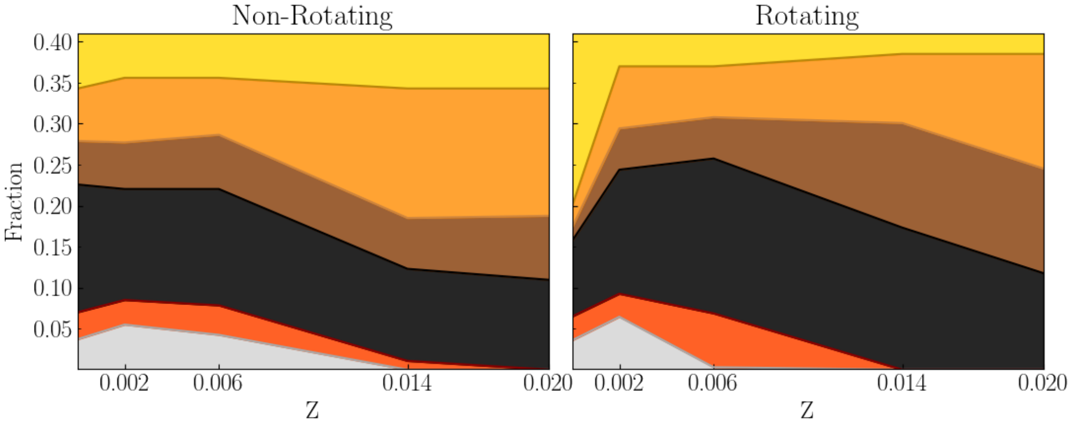

(b) Top-heavy IMF.

Figure 3.4: Plot of data from Table 3.4 and 3.5, with the fraction of massive stars per remnant type piled up on top of each other as per the colour coding used in Fig. 3.2.

using the Salpeter IMF. This effect is most significant at the highest masses, in particular those greater than 300 $M_{\odot}$. When discussing the results of this IMF weighting, the NS and NS (BH) categories will be considered together; this combination is given as 'Total NS' in Tables 3.4 and 3.5. Likewise, the BH and BH (NS) categories will be considered together; this combination is given as 'Total BH' in Tables 3.4 and 3.5.

Impact of metallicity

The non-rotating case weighted by the Salpeter IMF will be considered first, shown by the left panel of Fig. 3.4a. A significant proportion of massive stars are predicted to end their lives as NS at all metallicities considered. Table 3.3 shows that massive stars with initial mass between $9 - 30$ $M_{\odot}$ are much more common than those with higher mass; this is important as most stars in this mass range are predicted to end their lives as NS, and so the fraction remains high across all metallicities. The smallest fraction of massive stars to end their lives as NS is 0.829 at $Z = 0.006$, and the highest is 0.896 at solar metallicity- a difference in fraction of 0.067. The fraction of massive stars predicted to end their lives as BH increases from 0.136 at $Z = 10^{-5}$ to 0.143 at $Z = 0.006$, then sharply decreases due to mass loss when considering solar and supersolar metallicities to a fraction of around 0.1.

The fraction of PPISN is highly dependent on metallicity, with a fraction of over 0.01 predicted when $Z \leq 0.006$, decreasing to 0.004 at solar metallicity, and 0 at supersolar metallicity. This decrease is due to increased mass loss at higher metallicity, leading to smaller CO core masses that do not exceed the 40 $M_{\odot}$ threshold for PPISN at all masses considered. The fraction of PISN is similar to that of PPISN at $Z = 10^{-5}$ and $Z = 0.006$, increasing to a peak of almost 0.02 at $Z = 0.002$. When $Z > 0.006$, this fraction is 0 as no stars are predicted to have a

CO core mass above the 60 $M_\odot$ threshold for PISN due to high levels of mass loss.

Therefore, the main effect of metallicity on the fraction of massive stars per remnant type is due to the metallicity dependency of mass loss, given by Eq. (2.7). At low metallicity, there are more massive CO cores due to low levels of mass loss, increasing the fraction of (P)PISN and BH. At higher metallicity, increased levels of mass loss mean that the CO core mass does not exceed 40 $M_\odot$ and so there are very few (P)PISN (if any!). In addition, the high levels of mass loss mean that smaller CO core masses are more common, hence the increase in the fraction of NS at higher metallicities.

Impact of rotation

Now, the non-rotating and rotating cases (with Salpeter IMF weighting), will be compared. The main differences are clearly shown by Fig. 3.4a. Firstly, the majority of massive stars are still predicted to end their lives as NS, for the same reasons as outlined above. One key difference between the two panels of 3.4a is the significant increase in the fraction of NS at $Z = 10^{-5}$. In the non-rotating case, the fraction is 0.836, whereas in the rotating case it is 0.917. This increase is due to interactions between the hydrogen burning shell and helium burning core leading to a smaller CO core mass in rotating models (see Section 2.3.1 for more details). Massive stars within this mass range are heavily weighted by the IMF, hence this effect has a significant impact on the fraction of NS. The effect of metallicity is different for the rotating case, due to the hydrogen burning shell effect and the increased impact of mass loss in rotating models. The fraction of BH also shows a strong dependency on metallicity. Rotation decreases the fraction of BH at $Z = 10^{-5}$ significantly. This is because stars that would have massive enough CO cores to form BH if they were non-rotating experience the hydrogen shell effect, leading to smaller CO cores that lead to NS instead. For $Z \geq 0.002$, the fraction of massive stars ending their lives as BH is higher for rotating stars than their non-rotating counterparts. The most significant difference is at solar metallicity, where a fraction of 0.1 for non-rotating stars end their lives as BH; the fraction of rotating stars is almost double at 0.191. This is because of the increase in failed supernova leading to BH at this metallicity, which has a significant impact on the fraction due to the IMF weighting placing more emphasis on stars with mass between $9-30$ $M_{\odot}$. This effect is largely due to mass loss; stars which would have the remnant type NS (BH) if they were non-rotating tend to have the remnant type BH (NS) if they are rotating. This highlights the important impact that the islands of explodability (due to changes in compactness) can have on the fate of massive stars as a whole.

Rotation increases the fraction of PPISN when $10^{-5} < Z \leq 0.006$. Above this metallicity, no PPISN are predicted as the CO core mass of stars with solar and supersolar metallicity does not exceed 40 $M_{\odot}$ due to increased mass loss experienced by rotating stars. Similarly, the fraction of PISN is higher for rotating stars when $Z \leq 0.002$, but is almost zero at $Z = 0.006$ as very few stars at this metallicity have a CO core mass exceeding 60 $M_{\odot}$.

Impact of using a top-heavy IMF

The fraction of massive stars per remnant type is qualitatively very similar when comparing results weighted by either the Salpeter or top-heavy IMF, given by Fig. 3.4. Using the top-heavy IMF results in a smaller fraction of NS, and increased fractions of BH and (P)PISN. Additionally, using the top-heavy IMF means that less weighting is given to stars with mass between $9-30$ $M_{\odot}$, a small increase in weighting is given to stars with mass between $30-100$ $M_{\odot}$, and a significant increase in weighting is given to stars with mass over 100 $M_{\odot}$. This means that the fraction of (P)PISN experiences the most noticeable increase when considering the top-heavy IMF. Tables 3.4 and 3.5 show that these fractions are almost three times higher than those calculated using the Salpeter IMF. It is important to note that despite a fraction of 0.066 of rotating massive stars expected to result in PPISN at LMC metallicity (calculated using the top-heavy IMF from Schneider et al. (2018) based on an area of the LMC), there have been no confirmed observations of PPISN.

3.2 Maximum black hole mass

The black hole mass, M_{BH}, depends on the assumed mass of the ejecta. For direct black holes, this is assumed to be zero and so $M_{\mathrm{BH}} = M_{\mathrm{fin}}$. It is more complicated when considering failed supernova explosions, as some (or all) of the envelope could be ejected. Furthermore, when considering PPISN there will be significant mass ejected due to the pulsations and so determining the black hole mass is subject to uncertainties. Farmer et al. (2019) found that the black hole mass is dependent on CO core mass and metallicity as per Eq. (3.2).

$$M_{\mathrm{BH}} = \begin{cases} 4 + M_{\mathrm{CO}} & M_{\mathrm{CO}} < 38\ M_{\odot} \\ a_1 M_{\mathrm{CO}}^2 + a_2 M_{\mathrm{CO}} + a_3 \log Z + a_4 & 38\ \leq M_{\mathrm{CO}} \leq 60\ M_{\odot} \\ 0 & M_{\mathrm{CO}} > 60\ M_{\odot} \end{cases} \tag{3.2}$$

where $a_1 = -0.096$, $a_2 = 8.564$, $a_3 = -2.07$, $a_4 = -152.97$.

Eq. (3.2) is not used in this work for black hole masses of stars that undergo failed supernova and direct collapse as it is based on He stars only, and so $M_{\mathrm{BH}} = M_{\mathrm{fin}}$ alone will be used for black holes formed by direct collapse below the PI mass gap ($M_{\mathrm{CO}} < 40\ M_{\odot}$). Similarly, for black holes formed by direct collapse above the PI mass gap, $M_{\mathrm{BH}} = M_{\mathrm{fin}}$ will also be used. $M_{\mathrm{BH}} = M_{\mathrm{CO}}$ will be used for those that undergo failed explosions, with both NS (BH) and BH (NS) remnant types, assuming that they form black holes and eject their hydrogen and helium rich envelope. For stars that end their lives as PPISN, Eq. (3.2) will be used within the relevant M_{CO} domain, and PISN leave no remnant, hence $M_{\mathrm{BH}} = 0$, as per Eq. (3.2). Fig. 3.5 shows that the maximum black hole mass below the PI mass gap for non-rotating stars is $M_{\mathrm{BH,max}} = 92\ M_{\odot}$ (at $\mathrm{Z} = 10^{-5}$), and for rotating stars it is significantly lower with $M_{\mathrm{BH,max}} = 61\ M_{\odot}$ (also at $\mathrm{Z} = 10^{-5}$). This is because they are predicted to directly collapse to black holes (see Fig. 3.2), and

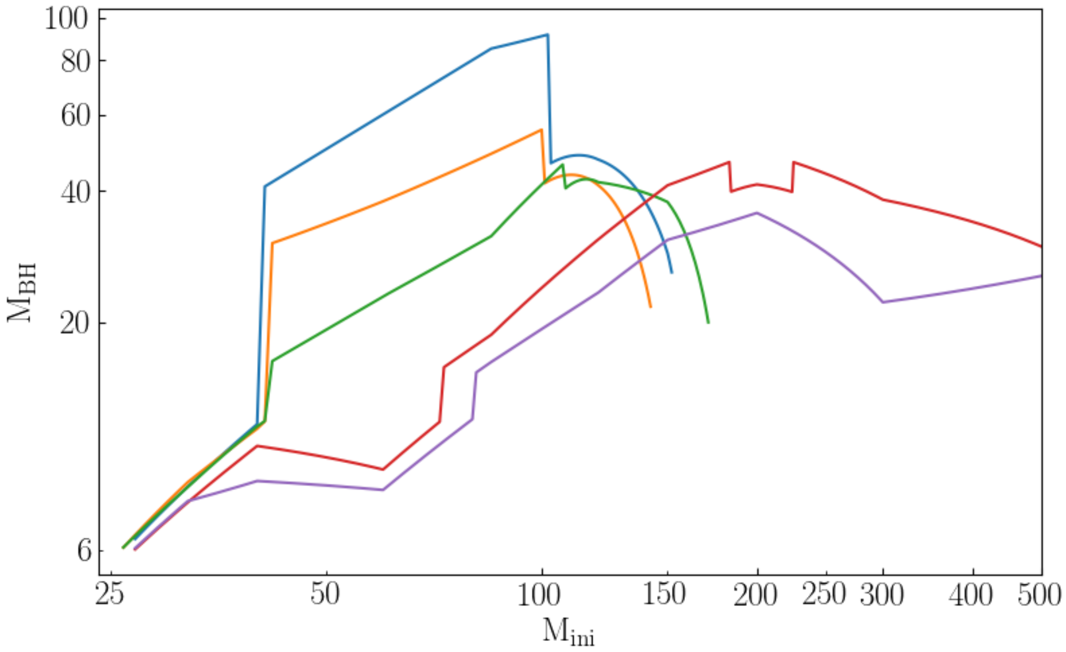

(a) Non-rotating

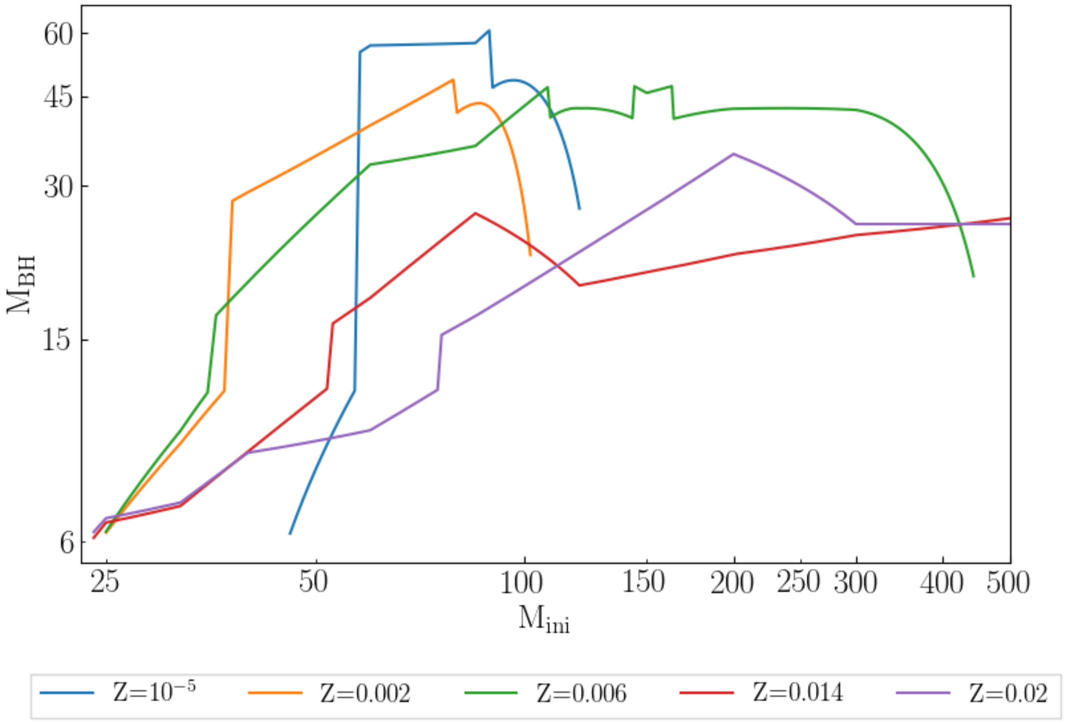

(b) Rotating

Figure 3.5: Black hole mass below the pair-instability gap.

so $M_{\mathrm{BH}} = M_{\mathrm{fin}}$. The final mass of the rotating models is lower than that of the non-rotating models due to increased mass loss (see Figs. 2.3 and 2.4). The recent detection of the GW190521 gravitational wave event involving a black hole with mass 85 $M_{\odot}$ challenged the existence of a PI mass gap between $M_{\mathrm{BH}} \approx 50 - 130\ M_{\odot}$ (Abbott et al., 2020; Fowler and Hoyle, 1964), but the results in this work suggest that the mass gap may have a higher boundary than first thought. This was also found in Vink et al. (2021), where it is predicted that black holes of mass $\sim$ 90 $M_{\odot}$ can form in low metallicity environments. This is also in agreement with results from Winch et al. (2024), where a maximum black hole mass below the PI mass gap of 93.3 $M_{\odot}$ was found using rotating models with $Z = 10^{-3}$. Note that the region in Fig. 3.5a where there is a sharp decrease in M_{BH} for $Z = 0.014$ is due to PPISN, which have a lower predicted mass due to mass lost during the pulsations. This is also seen in Fig. 3.5b for $Z = 0.006$, but the mass is higher in this case. This is because Eq. (3.2) predicts higher M_{BH} than M_{fin} (which is used either side of this region), due to the significant mass loss experienced by rotating models at this metallicity. Hence, the use of Eq. (3.2) has limitations when considering the models in this work.

It is important to also consider the mass of black holes *above* the PI mass gap. As per Fig. 3.2, direct black holes are predicted for both rotating and non-rotating models at low metallicities (below that of the SMC). These black holes are predicted to have $M_{\mathrm{BH}} = M_{\mathrm{fin}}$, which is very close to their initial mass as the models lose little mass throughout their evolution. The heaviest black hole predicted in this work has $M_{\mathrm{BH}} = 465.8\ M_{\odot}$, and lies above the PI mass gap. At the lower end of the mass range considered, no black holes below 6 $M_{\odot}$ are predicted by design. Note that this is expected as there is another likely black hole mass gap observed at $2 - 5\ M_{\odot}$ (Bailyn et al., 1998; Farr et al., 2011; Jonker et al., 2021).

3.3 Supernova type

Supernova types are based on both the spectral and light curve properties of a supernova explosion (see Fig. 1.8). In this work, this is based on the composition of the envelope which is retained by the star (if the envelope has not been completely lost), as per Table 3.6. Alternatively, the surface mass fraction of hydrogen/helium could also be used to determine supernova type, with Yoshida and Umeda (2011) using $X_{\rm He}^{\rm surf} = 0.5$ as the boundary between Type Ib and Ic, but this measure is less widely used than envelope masses. It is largely agreed that the threshold amount of hydrogen when differentiating between Type II and Type Ib supernovae is low, such that Wellstein and Langer (1999), Heger et al. (2003), Yusof et al. (2013) and Yoon et al. (2010) use a threshold of $M_{\rm H}^{\rm env} < 0.5\ M_{\odot}$ to determine whether a star is free of hydrogen whereas Georgy et al. (2009) use $M_{\rm H}^{\rm env} < 0.6\ M_{\odot}$. Considering this, the choice $M_{\rm H}^{\rm env} < 0.5\ M_{\odot}$ has been made in this work. It is important to note that it is suggested in Georgy et al. (2009) that a range of $0.6 < M_{\rm H}^{\rm env} < 1.5\ M_{\odot}$ gives very similar results for supernova type (see Appendix C for a comparison of threshold choices, shown by Fig. C.1 and C.2). The threshold for hydrogen poor/rich (and so between Type II and Ib supernovae) is non-zero because the absence of H lines in spectra does not indicate a complete absence of hydrogen in the envelope; factors such as the temperature and density of the envelope are also important when considering the strength of the H lines (Dessart et al., 2012). It is more difficult to choose a threshold amount of helium to distinguish models which explode as Type Ic from Type Ib since it is thought that the absence of He lines in spectra may not indicate absence of helium in the envelope of the progenitor, since this helium may be hidden due to very low ^{56}Ni mixing (if any) (Dessart et al., 2012). Despite this, both Frey et al. (2013) and Liu et al. (2016) determine that progenitors of Type Ic supernovae are completely free of helium. Frey et al. (2013) used a mixing algorithm based on 3D hydrodynamic simulations of massive stars to determine that the rates of mixing

Table 3.6: Progenitor properties for different types of core-collapse SN. H/He envelope mass at the end of core helium burning is given by $M^{\rm env}_{\rm H/He}$ respectively.

Envelope composition		SN type
$M^{\rm env}_{\rm H} > 2\ M_\odot$	$M^{\rm env}_{\rm He} > 0.5\ M_\odot$	Type IIP
$0.5 < M^{\rm env}_{\rm H} < 2\ M_\odot$	$M^{\rm env}_{\rm He} > 0.5\ M_\odot$	Type IIL
$M^{\rm env}_{\rm H} < 0.5\ M_\odot$	$M^{\rm env}_{\rm He} > 0.5\ M_\odot$	Type Ib
$M^{\rm env}_{\rm H} < 0.5\ M_\odot$	$M^{\rm env}_{\rm He} < 0.5\ M_\odot$	Type Ic

are higher than thought by Dessart et al. (2012). This mixing brings the helium into deeper, hotter layers of the star where it is burned to give O, resulting in completely helium free progenitors for Type Ic supernovae. For consistency, the choice $M^{\rm env}_{\rm He} < 0.5\ M_\odot$ has been made in this work in alignment with the value chosen for $M^{\rm env}_{\rm H}$.

To obtain the mass of hydrogen/helium in the envelope, the H/He mass fraction of each model was integrated throughout the star, since the CO core is free of both hydrogen and helium by definition. This allowed for determination of supernova type as described above. Additionally, models which are predicted to directly collapse to black holes in Section 3.1 are not allocated a type since they do not explode. Models resulting in BH (NS) or NS (BH) are allocated a type since it is uncertain to what extent they would explode (if at all).

3.3.1 Expected results

It is expected that stars with higher initial mass will generally lose more of their envelope as they evolve to higher luminosities, increasing the rate of mass loss which they experience. Additionally, stars with higher metallicity will lose more of their envelopes due to increased levels of mass loss. Due to this, more Type II supernovae are expected at low metallicity, and more Type 1b/c supernovae are expected at higher metallicity. Rotation is expected to decrease the minimum initial mass of progenitors of Type Ib/c supernovae as they will evolve to higher luminosities than their non-rotating counterparts. Similarly, rotation will decrease the number of Type II supernovae predicted as more models will lose their envelopes.

3.3.2 Impact of metallicity

Firstly, the effect of changing initial mass and metallicity will be considered for non-rotating models. Fig. 3.6a shows that when $M_{\rm ini} < 40\ M_\odot$ and $Z < 0.01$, most massive stars are expected to explode as Type IIP supernovae. This is because they experience low levels of mass loss during their evolution and so retain most of their envelope, which is rich in both hydrogen and helium. When $0.006 < Z < 0.01$ and $30 < M_{\rm ini} < 40\ M_\odot$, there is a region where stars retain a small amount of hydrogen in their envelope and so are expected to explode as Type IIL supernovae. This marks an intermediate region between Type IIP and Type Ib supernovae.

When $M_{\rm ini} > 40\ M_\odot$ and $Z < 0.01$, the dependence of supernova type on metallicity is stronger. It is important to note that stars in this region are predicted to either collapse directly to black holes, or explode as either PPISN or PISN of different types. PISN are indicated in Fig. 3.6a by the hatched region, then PPISN occur in the region between direct BH and PISN. A discussion of the supernova types of PISN will be presented in Section 3.4. When $Z < 0.01$ and $40 < M_{\rm ini} < 100\ M_\odot$, all stars are expected to directly collapse to black holes. When $100 < M_{\rm ini} < 325\ M_\odot$ and $Z < 0.002$, stars are expected to explode as Type IIP supernovae as they retain an envelope rich in both hydrogen and helium. This is due to the metallicity dependence of mass loss, given by Eq. (2.7), meaning that these stars experience low levels of mass loss. At the boundary between Type

IIP and Ib supernovae in Fig. 3.6a, there is a region where Type IIL supernovae are expected to occur, when $0.002 < Z < 0.006$ and $100 < M_{\mathrm{ini}} < 180\ M_{\odot}$. This region becomes very thin when $Z = 0.002$, extending from $200 < M_{\mathrm{ini}} < 500\ M_{\odot}$, as stars tend to either retain a hydrogen rich envelope or completely lose it, skipping the intermediate region. Then, Type Ib supernovae are expected between SMC and LMC metallicity for $200 < M_{\mathrm{ini}} < 500\ M_{\odot}$. Apart from a single point at $Z = 0.006$ and $M_{\mathrm{ini}} = 120\ M_{\odot}$ where one model is both H-poor and He-poor, the remainder of this area of Fig. 3.6a is expected to explode as Type Ib supernovae. This is because stars in this region are expected to lose all of the hydrogen in their envelope, while retaining a significant amount of helium.

When $0.01 < Z < 0.014$, the boundaries between Type IIP, IIL and Ib supernovae decrease in initial mass. This is because stars at lower initial mass tend to lose more of their envelope at higher metallicity. At higher metallicity, when $Z \geq 0.014$, initial mass has a more significant impact on supernova type than metallicity. This is shown in Fig. 3.6a, as the boundaries between different supernova types are largely horizontal, with a gentle upwards slope. This means that stars at supersolar metallicity explode as Type IIP supernovae at higher initial mass than those at solar metallicity. Mass loss which occurs later in the evolution means that more of the envelope is lost, which is the case for models at solar metallicity. After a region of expected Type IIL supernovae, Type Ib supernovae are predicted. Then, when $50 < M_{\mathrm{ini}} < 70\ M_{\odot}$, Type Ic supernovae are predicted above solar metallicity. These stars are free of both hydrogen and helium, since they experienced very high levels of post-MS mass loss. Stars between solar and supersolar metallicity above this mass range are expected to directly collapse to black holes. Hence, the impact of metallicity on supernova type is due to the dependence of mass loss rates on the metallicity. This effect changes depending on initial mass, which is related to the luminosity.

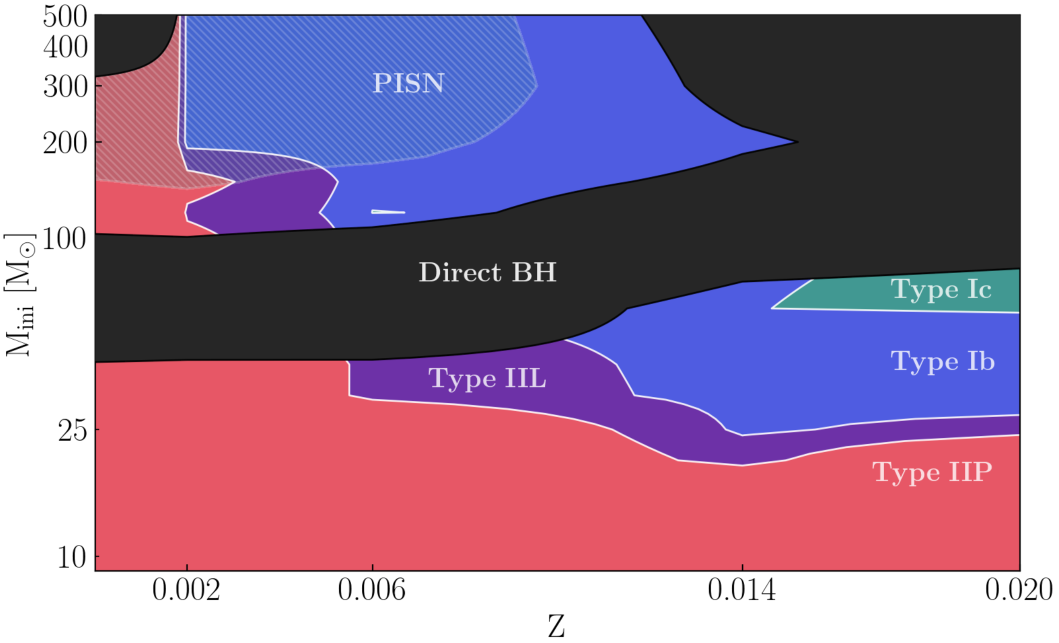

(a) Non-rotating

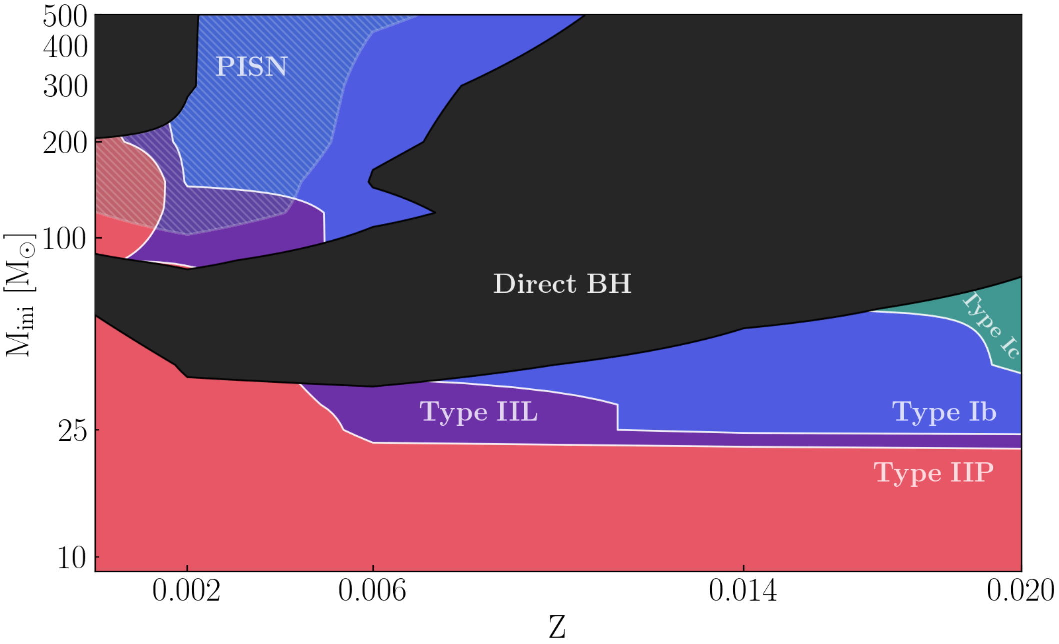

(b) Rotating

Figure 3.6: Supernova type as a function of initial mass and metallicity. The boundaries for each supernova type are given in Table 3.6.

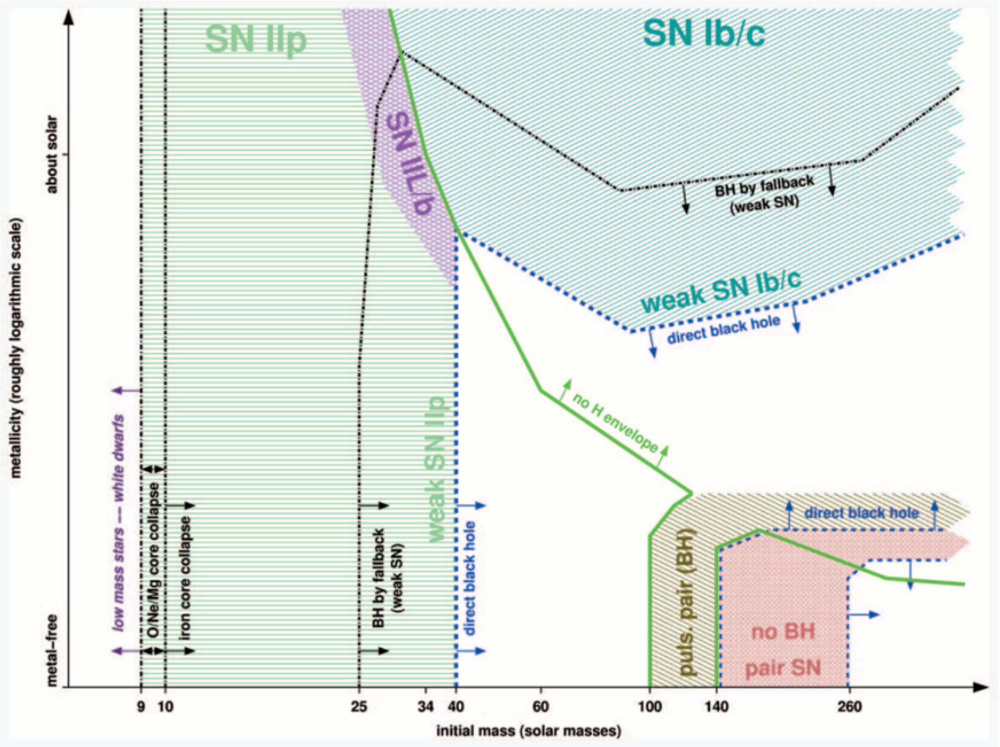

(a) Figure 2 from Heger et al. (2003).

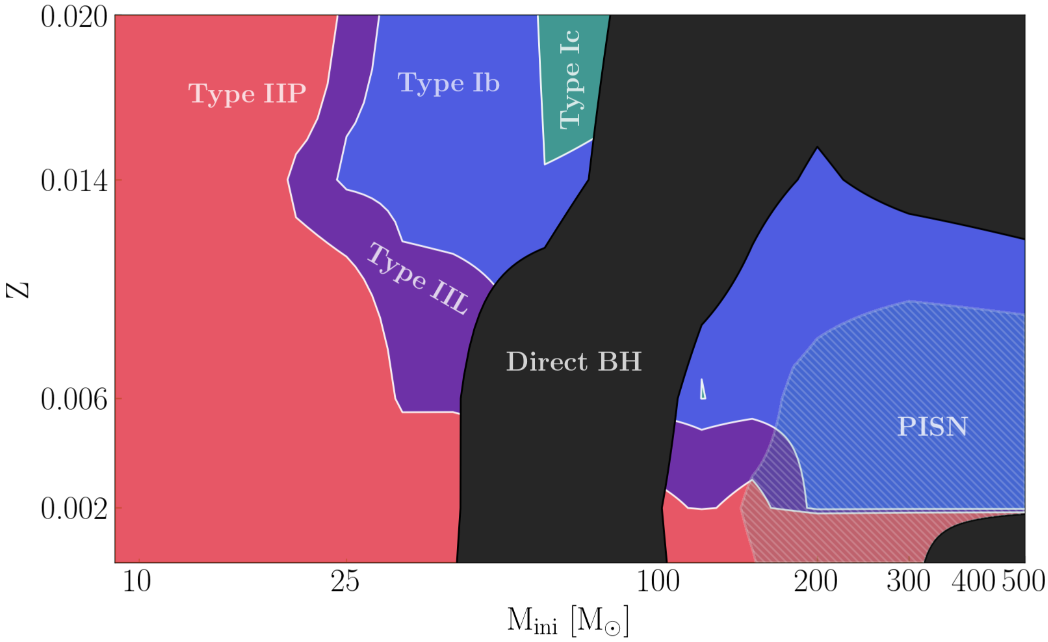

(b) Adapted from Figure 3.6a in this work.

Figure 3.7: Comparison of supernova type as a function of initial mass and metallicity between results from Heger et al. (2003) and this work.

Comparison to Heger et al. (2003)

Fig. 3.7a and 3.7b show a comparison between this work and that of Heger et al. (2003). Although they appear qualitatively quite similar, there are major differences between the two plots, largely due to the differing mass loss prescriptions used. The same threshold for stars that are considered H-poor, and so lead to Type IIP supernovae, is used in this work and that of Heger et al. (2003). In this work, Type IIP supernovae are expected above 100 $M_{\odot}$ at low metallicity, whereas Heger et al. (2003) suggested that the only Type IIP supernovae above 40 $M_{\odot}$ are PISN, as they assume that all PPISN have no hydrogen envelope.

Similarly, Type IIL supernovae are only predicted in a very narrow mass range at higher metallicity by Heger et al. (2003), but they are found across the whole metallicity range considered in this work. Heger et al. (2003) do not differentiate between Type Ib and Ic supernovae due to the uncertainties in how much helium is present in the envelopes of their progenitors (as they only simulate He stars) and so only limited comparisons can be made. Type Ib supernovae are found in a similar initial mass range in this work as that by Heger et al. (2003). It appears as if they are found at lower metallicity in this work, but the metallicity scale used by Heger et al. (2003) does not allow for direct comparisons to be made. The regions where there is direct collapse to black holes, PPISN and PISN is qualitatively similar in both Fig. 3.7a and 3.7b, but also has significant differences as discussed in Section 3.1.2.

3.3.3 Impact of rotation

The impact of rotation can be seen in Fig. 3.6, and differs depending on both initial mass and metallicity, due to the competing effects that rotation has on the mass of hydrogen and helium in the envelope. The results on the $M_{\text{ini}} - Z$ plane will be separated into four cases depending on the initial mass and metallicity, where the dominant effect due to rotation differs.

Case 1: low initial mass and low metallicity

When $M_{\rm ini} < 40\ M_{\odot}$ and $Z < 0.01$, the impact of rotation on supernova type is limited. At $Z = 10^{-5}$ in the rotating case, the boundary between Type IIP and direct collapse to black hole is at much higher initial mass than in the non-rotating case. Between $10^{-5} < Z < 0.002$, this boundary falls to 40 $M_{\odot}$, which is where it is situated in the non-rotating case. Hence, the impact of rotation in this region of Fig. 3.6b is limited to $Z < 10^{-5}$, due to the interaction between the hydrogen burning shell and helium burning core. The lower CO core mass means that models at lower initial mass that would directly collapse to black holes in the non-rotating case are predicted to successfully explode in the rotating case.

Case 2: low initial mass, higher metallicity

When $M_{\rm ini} < 40\ M_{\odot}$ and $Z > 0.01$, rotation has a few interesting effects. Firstly, the boundaries between Type IIP, IIL and Ib supernovae become completely horizontal, showing no dependence on metallicity. This is because models with $M_{\rm ini} \geq 25\ M_{\odot}$ completely lose their hydrogen envelope at both solar and supersolar metallicity. In the non-rotating case, the boundaries show more of a metallicity dependence, since models at solar and supersolar metallicity do not completely lose their hydrogen envelope at the same initial mass. On the other hand, the boundary between Type Ib and Ic is *more* dependent on metallicity such that stars at supersolar metallicity explode as Type Ic supernovae at lower initial mass than their non-rotating counterparts. This is because more stars at supersolar metallicity lose both their hydrogen and helium envelope due to increased mass loss.

Case 3: high initial mass, low metallicity

When $M_{\text{ini}} > 40\ M_{\odot}$ and $Z < 0.01$, Type IIP supernovae are only predicted below SMC metallicity. This is similar to the non-rotating case, but Type IIL supernovae are predicted at lower metallicities in the rotating case. This is because rotating stars evolve at higher luminosities and so experience higher rates of mass loss which can partially strip the star of its hydrogen envelope, even at metallicites below that of the SMC. Above $Z = 0.006$, stars are predicted to directly collapse to black holes from 100 $M_{\odot}$ to 300 $M_{\odot}$, whereas no direct black holes are predicted above $M_{\text{ini}} = 100\ M_{\odot}$ and $Z = 0.006$ in the non-rotating case. Additionally, no Type Ic supernova are predicted in this region, whereas in the non-rotating case there is a point where they are predicted.

Case 4: high initial mass, higher metallicity

When $M_{\text{ini}} > 40\ M_{\odot}$ and $Z > 0.01$, only direct collapse to black holes are predicted in the rotating case. This was not the case for non-rotating stars, where some stars in this region were predicted to explode as Type Ib supernovae. This is because the rotating models lose more mass early in their evolution, leading to CO core masses below 40 $M_{\odot}$ at all initial masses.

3.3.4 Fraction of massive stars per supernova type

As with remnant type, the distribution of supernovae depends on the regions identified in Fig. 3.6 and the choice of IMF. Supernovae types were weighted using the same mass distributions as used for remnant type (see Section 3.1.4 for details). Results using the Salpeter IMF are given in Table 3.7, and those calculated using the top-heavy IMF are given in Table 3.8.

Impact of metallicity

The non-rotating case weighted by the Salpeter IMF will be considered first, shown by the left panel of Fig. 3.8a. When $Z = 10^{-5}$, a fraction of 0.909 of massive stars explode as Type IIP supernovae. No other types of supernovae are expected at this metallicity, with the remaining fraction of 0.091 directly collapsing to black holes. The low rates of mass loss experienced by stars at this metallicity means that the envelope is rich in both hydrogen and helium across the range of initial masses considered in this work. As metallicity increases from $Z = 10^{-5}$ to $Z = 0.014$, the fraction of Type IIP supernovae decreases to 0.676. Then, from $Z = 0.014$ to $Z = 0.02$, the fraction of Type IIP supernovae increases to 0.763. This is because mass loss occurs later in the evolution of stars with initial mass below 25 $M_{\odot}$ at solar metallicity when compared to supersolar metallicity. Note that models below 25 $M_{\odot}$ at both metallicities have similar CO core masses and final masses, it is only the envelope mass which differs. This shows that they undergo a similar amount of mass loss throughout the whole evolution, but models at solar metallicity undergo more mass loss *later* in the evolution. The fraction of massive stars predicted to explode as Type IIL supernovae is zero when $Z = 10^{-5}$, increasing to 0.073 at solar metallicity. This increase is due to increased levels of mass loss as metallicity increases. The fraction of Type IIL supernovae decreases to 0.044 at supersolar metallicity, as more stars are predicted to explode as Type IIP supernovae.

No stars at $Z = 10^{-5}$ are expected to explode as Type Ib supernovae, since they all have envelopes rich in hydrogen. From $Z = 0.002$ to $Z = 0.014$, the fraction of massive stars expected to explode as Type Ib supernovae increases from 0.011 to 0.203 due to the increased rates of mass loss experienced by models at this metallicity. This fraction falls to 0.122 at supersolar metallicity. The fraction of massive stars predicted to explode as Type Ic supernovae is very low, or

Table 3.7: Fraction of massive stars per supernova type, calculated using the IMF from Salpeter (1955) with $\alpha = 2.35$.

Z	Type IIP	Type IIL	Type Ib	Type Ic	Direct BH
Non-rotating					
10^{-5}	0.909	0	0	0	0.091
0.002	0.898	0.009	0.011	0	0.082
0.006	0.833	0.053	0.028	0.001	0.086
0.014	0.676	0.073	0.203	0	0.048
0.02	0.763	0.044	0.122	0.026	0.044
Rotating					
10^{-5}	0.956	0	0	0	0.044
0.002	0.870	0.026	0.013	0	0.091
0.006	0.734	0.124	0.025	0	0.117
0.014	0.734	0.029	0.155	0	0.082
0.02	0.717	0.046	0.110	0.078	0.049

Table 3.8: Fraction of massive stars per supernova type, calculated using the top-heavy IMF from Schneider et al. (2018) with $\alpha = 1.9$.

Z	Type IIP	Type IIL	Type Ib	Type Ic	Direct BH
			Non-rotating		
10^{-5}	0.844	0	0	0	0.156
0.002	0.807	0.021	0.036	0	0.135
0.006	0.710	0.069	0.077	0.001	0.142
0.014	0.540	0.075	0.273	0	0.112
0.02	0.630	0.050	0.165	0.045	0.110
			Rotating		
10^{-5}	0.907	0	0	0	0.093
0.002	0.759	0.055	0.035	0	0.151
0.006	0.599	0.144	0.069	0	0.189
0.014	0.599	0.032	0.197	0	0.173
0.02	0.581	0.049	0.132	0.120	0.118

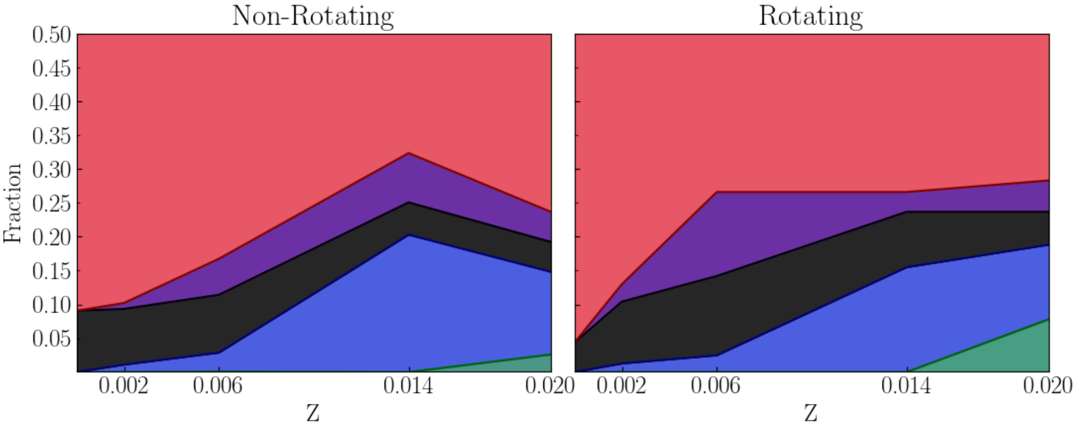

(a) Salpeter IMF.

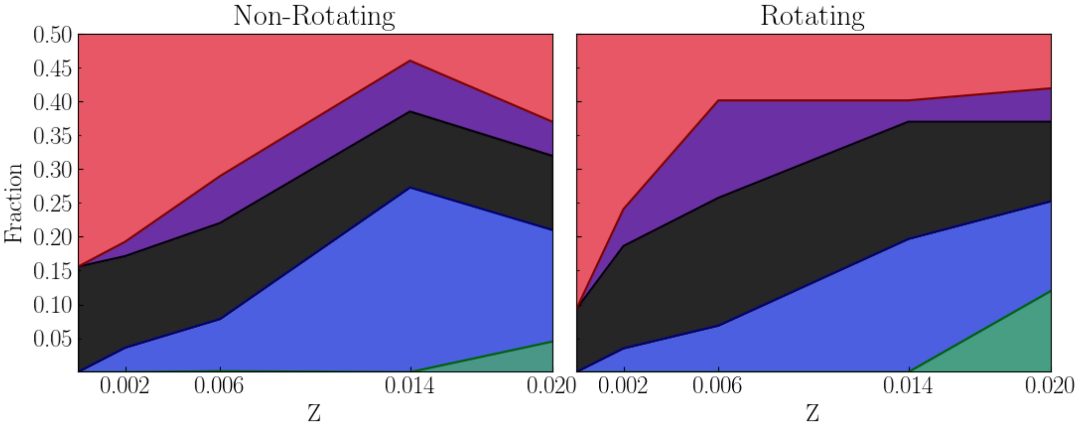

(b) Top-heavy IMF.

Figure 3.8: Plot of data from Table 3.7 and 3.8, with the fraction of massive stars per supernova type piled up on top of each other as per the colour coding used in Fig. 3.6.

zero, across all metallicities considered. At EMP, SMC and solar metallicities, no Type Ic supernovae are predicted. When $Z = 0.006$, a fraction of 0.001 is expected to explode as Type Ic supernovae, while at $Z = 0.02$ the same fraction is 0.026. These supernovae are predicted to be very rare for massive single stars, as very few have envelopes free of both hydrogen and helium. Those that do tend to have high initial mass, and so are not favourably weighted by the Salpeter IMF. Finally, the fraction of massive stars predicted to directly collapse to black holes is the same as discussed in Section 3.1.4. Hence, metallicity has a significant impact on supernova type, due to the metallicity dependence of mass loss.

Impact of rotation

Now, the non-rotating and rotating cases (with Salpeter IMF weighting), will be compared. The main differences are shown by Fig. 3.8a, with the two appearing qualitatively similar. When $Z = 10^{-5}$, the fractions are very similar between the non-rotating and rotating case, with the only predicted outcomes being either a Type IIP supernova or direct collapse to a black hole. In the rotating case, the fraction of massive stars predicted to explode as Type IIP supernovae is 0.956, which is higher than the same fraction in the non-rotating case. This is because of the interaction between the hydrogen burning shell and helium burning core in stars at this metallicity, with less rotating stars expected to directly collapse to black holes when compared to non-rotating stars. The fraction of massive stars expected to explode as Type IIL supernovae is higher for rotating stars when $0.002 \leq Z \leq 0.006$, as more rotating stars partially lose their hydrogen envelope. This fraction is lower than that for non-rotating stars at solar metallicity due to the increased fraction of direct black holes. At supersolar metallicity, this fraction is very similar between the non-rotating and rotating case, as shown by Fig. 3.8.

The fraction of massive stars predicted to explode as Type Ib supernovae is zero when $Z = 10^{-5}$ for both non-rotating and rotating stars. When $Z = 0.002$, this fraction is higher by 0.002 for rotating models, showing a small increase from the non-rotating case. When $Z \geq 0.014$, this fraction is lower for rotating stars. This is because more rotating stars are expected to directly collapse to black holes, which would have exploded as Type Ib supernovae in the non-rotating case. The fraction of rotating massive stars expected to explode as Type Ic supernovae is zero, apart from at supersolar metallicity where it is more than double that in the non-rotating case. This is because more rotating stars are expected to be completely free of both hydrogen and helium due to the increased mass loss rates which they experience. Hence, the effect of rotation on supernova type is dominated by increased mass loss, as well as the increased number of stars expected to directly collapse to black holes.

Impact of using a top-heavy IMF

The fraction of massive stars per supernova type is qualitatively very similar when comparing results weighted by either the Salpeter or top-heavy IMF, given by Fig. 3.8. Using the top-heavy IMF results in a decrease in the fraction of Type IIP supernovae, and an increase in the fraction of all other possibilities across the whole range of metallicities considered. This is because stars that explode as Type IIP supernovae generally have a lower initial mass (apart from when $Z = 10^{-5}$), and these stars make up less of the stellar population calculated using the top-heavy IMF than the Salpeter IMF. The largest increase in fraction is seen for direct black holes, as they occur within the initial mass range of $30 - 100\ M_{\odot}$ where the top-heavy IMF has the largest impact on the calculated population, as per Section 3.1.4.

3.4 Pair-instability supernova types

Despite the lack of observational evidence for PISN, it is still important to consider the proportion of supernovae which may be PISN as they have very different nucleosynthetic yields, as shown by Fig. 3.9. It shows that the odd-even effect is more significant for PISN than core-collapse supernovae, alongside higher abundances of Si, S, Ar and Ca due to the explosive oxygen burning (Kobayashi, 2015). This has implications within the field of Galactic chemical evolution, where these nucleosynthetic yields are used within simulations of chemical enrichment processes. However, Kobayashi et al. (2020) did not include effects from PISN in their Galactic chemical evolution models due to the lack of observational evidence. Hence, advancements in understanding whether PISN are likely to occur will be important if the observational data does become available. Additionally, the fraction of supernovae expected to be PISN is important when considering the black hole mass distributions found in gravitational wave events (Marchant et al., 2016; Farmer et al., 2019; Winch et al., 2024), in particular the PI mass gap discussed in Section 3.2.

Fig. 3.10 shows the proportion of all supernovae of a particular type which are expected to be PISN, with the data given in Table D.1 and D.2 in Appendix D. It is important to note that no PISN are expected at solar or supersolar metallicities, for both the non-rotating and rotating case using both variations of the IMF. Firstly, the impact of metallicity will be considered, for the non-rotating case calculated using the Salpeter IMF. When $Z = 10^{-5}$, the fraction of Type IIP supernova expected to be PISN is small, at 0.014. This fraction is lower, at 0.004, when $Z = 0.002$. However, the fraction of Type IIL supernovae expected to be PISN is significantly higher, at 0.424, and *all* Type Ib supernovae at SMC metallicity are expected to be PISN. When $Z = 0.006$, no Type IIP/L supernovae are expected to be PISN, and the fraction of Type Ib supernovae expected to be

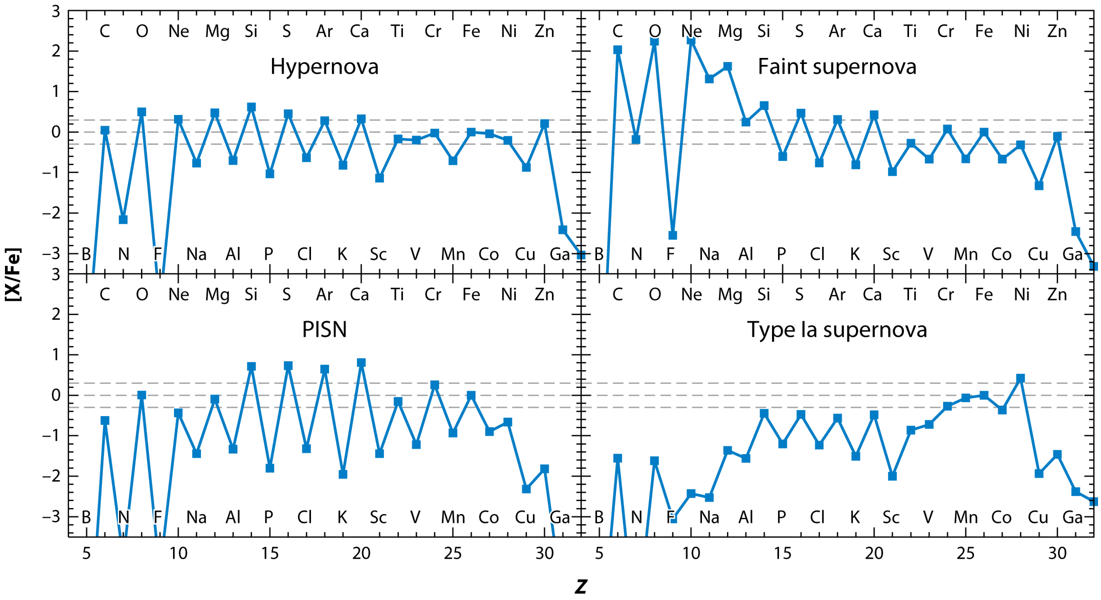

Figure 3.9: A comparison of the yields of PISN with that of hypernovae, faint supernovae and Type Ia supernovae. Taken from Nomoto et al. (2013) (Fig. 8).

PISN is 0.476, which is lower than when $Z = 0.002$. Hence, the impact of metallicity depends on the supernova type considered. The fraction of Type IIP supernovae expected to be PISN decreases as metallicity increases, reaching 0 when $Z = 0.006$. This is because PISN have progenitors at low metallicity which are VMS, and progenitors of Type IIP supernovae are generally not VMS when $Z > 0.002$. The fraction of Type Ib supernovae expected to be PISN falls from 1 when $Z = 0.002$ to 0 when $Z = 0.0014$, as PISN are only expected at low metallicity. The most significant effect of rotation on PISN types is the significant decrease in the fraction of Type Ib supernovae expected to be PISN from 0.476 in the non-rotating case to 0.030 in the rotating case. This is because PISN are only expected when $Z \leq 0.006$ in the rotating case due to lower CO core masses than in the non-rotating case. Using the top-heavy IMF results in an increase in all of the fractions, other than those equal to either 0 or 1; the choice of IMF has a significant impact on the fraction of Type IIP supernovae expected to be PISN, and very little impact on that of Type IIL and Ib. Note that the gaps in Table D.1 and D.2 mean that no supernovae of that type are predicted at the given

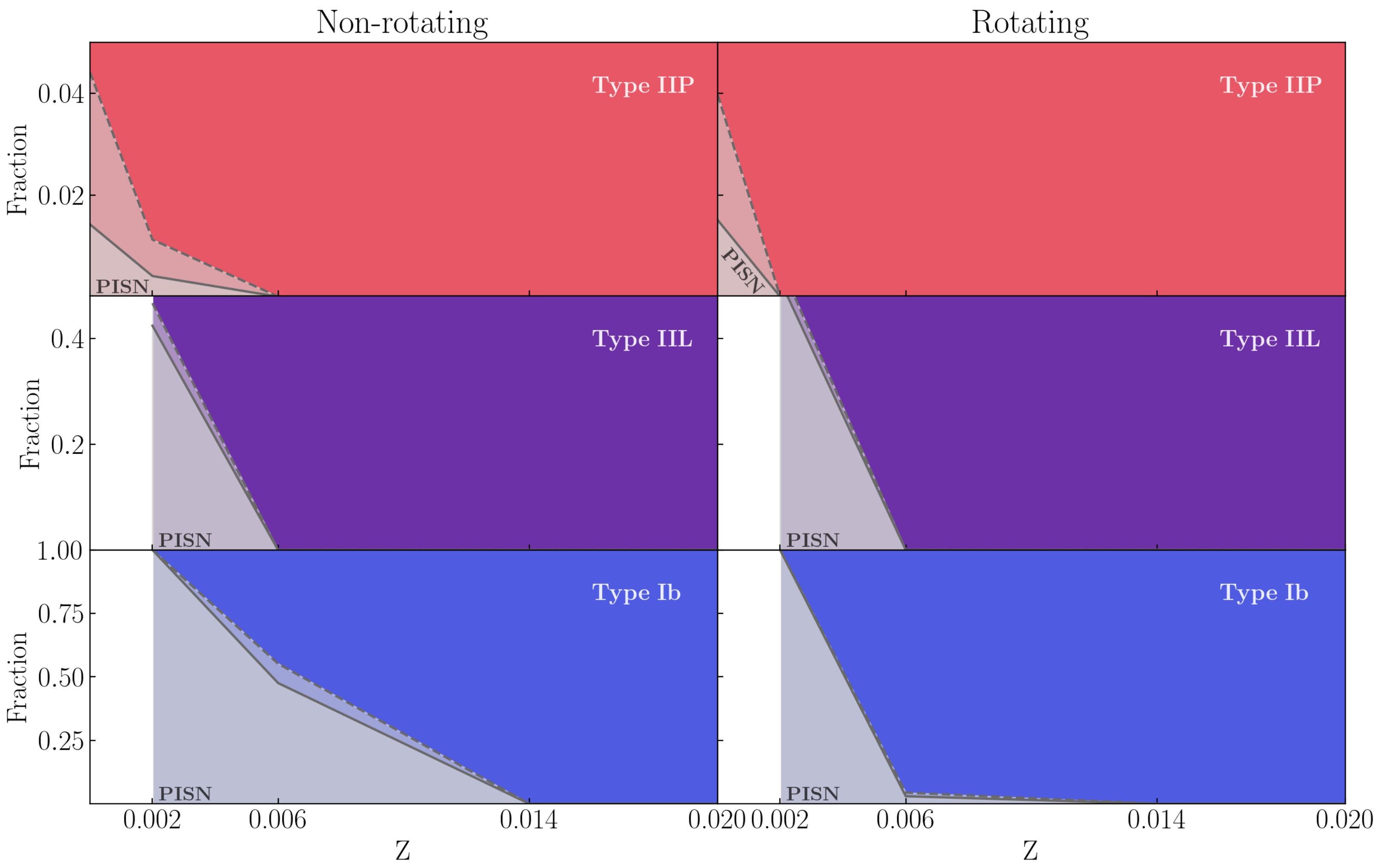

Figure 3.10: Fraction of different types of supernovae that are predicted to be PISN. The solid line indicates the fraction calculated using the Salpeter IMF, while the dashed line indicates the fraction calculated using the top-heavy IMF.

metallicity. See Appendix D for data on the fraction of PPISN and PISN of different types.

3.5 Comparison to observations

Table 3.9 gives a comparison between the proportions of different supernova types found in this work, compared to observational results from Smith et al. (2011) and Li et al. (2011). The observational results show a lower fraction of Type IIP supernovae than the fraction found in this work. This is not affected by choice of IMF, or whether the rotating or non-rotating case is considered. Both Smith et al. (2011) and Li et al. (2011) also show a significantly higher fraction of Type Ic supernovae than that found in this work, again regardless of rotation or IMF choice. The observational fraction of Type IIL supernovae is slightly higher than predicted in this work. The observational fractions of Type Ib supernovae vary from Smith et al. (2011) to Li et al. (2011), but are relatively consistent with the fractions predicted in this work, though the fractions calculated using the top-heavy IMF are higher than the observational range in Type Ib fraction. This suggests that the Salpeter IMF may be more representative in this case. It is important to acknowledge that it is difficult to make comparisons to observational results due to the large fraction of massive stars that exist in binary systems (Sana et al., 2012). The results presented in this chapter only consider single stars, and there is no way to separate the observational data for binary and single stars. Hence, it is difficult to tell *where* the differences between the observational data and the results presented in this chapter originate from, due to the significant effects that binary interactions can have on the fate of massive stars (see Section 3.6 for more detail).

Table 3.9: Comparison of the fraction of massive stars per supernova type across all metallicities calculated in this work and observational fractions of supernovae from Smith et al. (2011) and Li et al. (2011).

	Type IIP	Type IIL	Type Ib	Type Ic
Smith et al. (2011)	0.629	0.084	0.093	0.194
Li et al. (2011)	0.656	0.094	0.070	0.180
Non-rotating				
Salpeter IMF	0.877	0.039	0.078	0.006
Top-heavy IMF	0.813	0.049	0.127	0.011
Rotating				
Salpeter IMF	0.869	0.049	0.065	0.017
Top-heavy IMF	0.805	0.066	0.101	0.028

Overall, these differences suggest that most Type Ic supernovae result from stars in binary systems, where the hydrogen envelope has been removed through mass transfer. Observations of PISN are expected to present as superluminous supernovae with broad light curves (Gal-Yam, 2012). PISN are difficult to find with optical transient surveys as they are expected to occur at high redshift (due to the low metallicity of their progenitors), and so are faint in the optical wavelength range. For example, there is a deep optical survey with Subaru/Hyper Suprime-Cam (HSC), aimed at finding PISN candidates, but it has so far not found any (Moriya et al., 2021). Instead, the use of near-infrared instruments is more suitable for searching for PISN as they are bright in the near-infrared range. In the next decade, several wide-field near-infrared instruments are planned, such as the near-infrared wide-field instrument on the recently launched Euclid satellite (Scaramella et al., 2022) and the Wide Field Instrument on the Nancy Grace Roman space telescope (Spergel et al., 2015), which have the potential to find PISN candidates. However, there are currently no confirmed observations of PISN, and so no comparisons can be made in this case.

3.6 Effect of binarity

Most massive stars form in multiples and interactions between massive binary stars are common as they tend to exist in close binary systems (Chini et al., 2012; Sana et al., 2012; Preibisch et al., 2001). Due to this, it is important to consider the effect that binarity would have on the results presented in this chapter. For a more in-depth description of the ways binarity affects stellar evolution in general, see the review by Langer (2012).

3.6.1 Mass transfer

Firstly, the impact of mass transfer will be discussed. There are three different scenarios in which mass transfer can occur (known as Cases, see Kippenhahn et al. (1990); Podsiadlowski et al. (1992)):

- **Case A:** In very close binaries, the mass transfer occurs when the donor star is still on the main-sequence.
- **Case B:** The mass transfer occurs when the donor star is no longer on the main-sequence, during core helium burning.
- **Case C:** The mass transfer occurs after the donor star has finished core helium burning.

Mass transfer occurs when one of the stars in the binary systems overfills its Roche lobe, which is the region around the star where material is gravitationally bound to it. Roche lobes are approximated by a volume-equivalent radius using the fit from Eggleton (1983), given by Eq. (3.3).

$$R_{RL,1}(q) = f(q)a, \qquad f(q) = \frac{0.49q^{2/3}}{0.6q^{2/3} + \ln\left(1 + q^{1/3}\right)}, \tag{3.3}$$

where $q = m_1/m_2$ is the mass ratio, $R_{RL,1}$ is the Roche lobe radius of the star with mass m_1 and a is the orbital separation.

Stars with higher initial mass generally have shorter lifetimes and so it is usually the more massive star ($m = m_1$) which loses mass as the donor star, and the less massive star ($m = m_2$) that gains mass. Additionally, the mass ratio can invert if the initially most massive star loses enough mass. When the donor has a radiative envelope (generally Case A mass transfer), the envelope has a smaller radius after losing mass, and so experiences stable mass transfer. However, convective envelopes either have a constant or slightly larger radius while the Roche lobe radius has decreased, and so experience unstable mass transfer (see Paczynski and Sienkiewicz (1972) for details). In this case, a common envelope phase will occur, resulting in a very close system where the donor has become a completely stripped core as its whole envelope has become unbound. Note that this is a simplified view of events, and the radius of the donor star depends on many factors (Podsiadlowski et al., 1992).

Mass transfer has a significant impact on the evolution of both stars involved, and so will influence their respective fates. If the mass transfer occurs before the end of core helium burning (Case A or B), it can change the mass of the donor star's convective core. This means that it would end core helium burning with a smaller CO core mass, and so this would affect the remnant type predicted in this work. It may possibly result in more NS, and reduce the fraction of massive stars expected to end their lives as PISN, as this requires that very high CO core masses are retained. Additionally, loss of the envelope means that the fraction of massive stars expected to explode as Type Ib/c supernovae would be higher when including effects due to mass transfer. On the other hand, the secondary star in the binary system would have a larger envelope mass, and so may retain more hydrogen/helium in the envelope than if it were a single star. Hence, the effects that mass transfer has on the fate of massive stars is complicated! It is important to note that De Donder and Vanbeveren (2002) found that including binary stars in models of galactic chemical evolution had only a moderate effect on yield, suggesting that considering only single stars is sufficient for the purposes of this work.

3.6.2 Tidal interactions

In close binary systems, stars tend to synchronise their rotation to the orbital period, causing tidal mixing that dissipates the excess kinetic energy (Zahn, 1975, 1977, 2013). The time needed for synchronisation is given by Eq. (3.4) from Zahn (1977).

$$\begin{aligned}\frac{1}{t_{synch}} &= -\frac{d}{dt}\left|\frac{2(\Omega-\omega)}{\omega}\right|^{-5/3} \\ &= 5\cdot 2^{5/3}\left(\frac{GM}{R^3}\right)^{1/2}\frac{MR^2}{I}\,q^2(1+q)^{5/6}\,E_2\left(\frac{R}{a}\right)^{17/2} \qquad (3.4)\end{aligned}$$

where Ω is the star's angular velocity, ω is the orbital angular velocity, I is the inertia of the star and E_2 is the structure constant, which describes coupling between the tidal potential near the interface of the convective core and radiative envelope and the gravity mode dissipating it close to the surface of the star.

These internal tides increase rotational mixing, and so increase the effects of rotation even further. Additionally, this leads to the star being very compact, as it is in quasi-chemical equilibrium throughout its evolution. This means that it is less likely to overfill its Roche lobe, and so may prevent any resulting mass transfer. Hence, the effects of mass transfer on the fate of massive stars may be less significant than described in Section 3.6.1. Fig. 3.11 shows numerous possible intermediate products and end-points of the evolution of massive binary stars. This shows the complexity of considering binary interactions when determining the fate of massive stars, and illustrates why it is beyond the scope of this work.

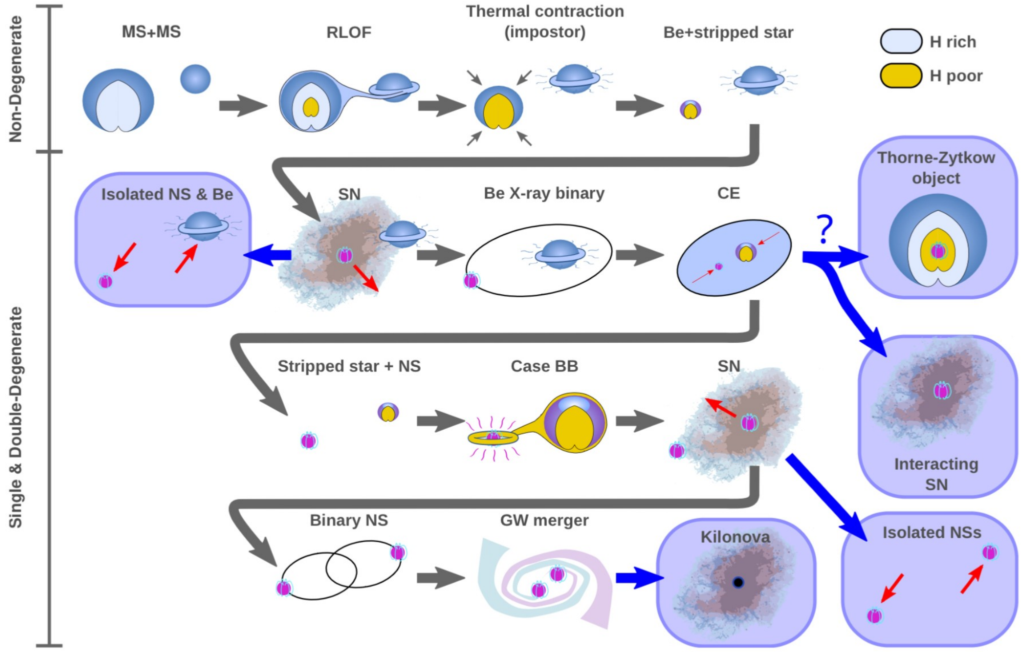

Figure 3.11: The evolution of massive binary stars up to the formation of a GW source, showing various intermediate products, with the phases in blue boxes showing the end points of binary evolution. Taken from Marchant and Bodensteiner (2023) (Fig. 4).

See Eldridge et al. (2017) for an example of how stellar evolution models can include effects due to binarity.

Chapter 4

Conclusions

In this thesis, the relationship between the life and death of massive single stars has been explored, resulting in the determination of their final fates from the properties of grids of stellar models at the end of core helium burning. The impact of varying the initial mass, metallicity and rotation on the fate of massive stars will be summarised in this final chapter. As initial mass is varied, different fates are found. At low initial mass, most massive stars are found to result in Type IIP supernovae and the formation of a neutron star. Then, as the initial mass increases, stars are less likely to successfully explode, and so are more likely to form black holes. Very massive stars are expected to end their lives as either PPISN or PISN (at low metallicity), or direct collapse to black holes (at higher metallicity). Extremely metal poor stars with the highest initial masses are also expected to directly collapse to black holes. Hence, varying the initial mass has a significant impact on the fate of massive stars.

This has also been explored through choice of IMF, considering different mass distributions and how this affects the results presented. The use of a top-heavy IMF allows for a closer match to observational data on supernova type than the use of the Salpeter IMF, possibly suggesting that the top-heavy IMF is a better match for the mass distribution of massive stars. However, the observational data does not exclude supernovae resulting from stars in binary systems, and so any comparisons should be treated with caution.

As the metallicity is increased, the rates of mass loss on the main sequence also increase, as per Eq. (2.7). This results in reduced CO core masses at higher metallicities, having various impacts on the remnant it leaves behind. In particular, very massive stars with low metallicity can end their lives as PISN and so leave behind no remnant. As long as the star does not become a RSG, increasing the metallicity also increases the rate of post-main sequence mass loss. This means that a significant proportion of the envelope may be lost, possibly resulting in Type Ib/c supernovae. Hence, metallicity has a significant impact on the final fate of massive stars as a whole, with both the remnant and supernova type showing a strong dependence on the metallicity.

Rotation has also been shown to have a significant impact on the fate of massive stars. It has two main competing effects: increased mixing tends to increase the CO core mass, and increased mass loss tends to decrease the CO core mass and H/He envelope mass. In addition to these effects, an unusual boost in the hydrogen burning shell of extremely metal poor models leads to a decrease in the CO core mass, which was unexpected. The dominant effect of rotation differs depending on initial mass and metallicity. Hence, rotation has different effects on the fate of massive stars depending on the other parameters considered.

One important direction for future research concerns pair-instability supernovae. If upcoming near-infrared wide-field surveys do not find potential PISN candidates at high redshift, then the theoretical framework on which the predictions in this work are based may need to be re-evaluated. Furthermore, if there are detections of gravitational wave events involving merging black holes with masses within the predicted mass gap, this may also challenge existing theory. The effect of varying metallicity on the IMF is another avenue for further exploration due to its uncertain nature, with the aim of calculating more accurate proportions of different remnant/supernova types from massive single stars to compare with observational data. Although a brief consideration of the effects of binarity on the fate of massive stars has been given, future studies could include quantitative analysis of these effects, through the inclusion of models of massive binary stars.

The most significant, novel findings of this work are summarised in the following list:

- The competing effects that rotation has on the evolution of massive stars results in it having a complex effect on both remnant and supernova type, depending on the initial mass and metallicity of the star.
- A pair-instability mass gap is expected when considering the distribution of black hole massses, from $\sim 92\ M_\odot$ to $\sim 250\ M_\odot$. Extremely metal poor stars with the highest initial masses are expected to directly collapse to black holes with mass *above* the pair-instability mass gap.
- Pair-instability supernovae and pulsation pair-instability supernovae are predicted at metallicities lower than solar, and initial masses greater than $100\ M_\odot$.

Understanding the fate of massive stars, and how it is impacted by various factors, has important applications across many different fields within astrophysics. The way in which massive stars die, both the type of supernova they produce and the type of compact remnant they leave behind, has significant effects on models of galactic chemical evolution, nucleosynthetic yields, gravitational wave astronomy, and also provides the necessary context for the interpretation of observational data. Since observations are generally limited to the surface properties of stars, the use of models and assumptions is important when considering the internal properties of massive stars. The fate of a massive star has its basis in both internal and surface properties, in particular the CO core mass and composition of the envelope. The grids of one-dimensional stellar evolution models used in this work have been calculated over the past decade, covering a wide range on initial masses, metallicities and considering models with and without rotation. This allows for analysis of how the properties, and the fate, of massive stars varies across this parameter space.

There are still many uncertainties to consider when using stellar evolution models, such as the mass loss prescriptions used and the extent of their convective zones. Using observational constraints and multi-dimensional stellar evolution models, these uncertainties can hopefully be reduced in the future as our understanding of stellar evolution continues to advance.

Appendix A

Origin of models

Table A.1: List of models used and their origin where superscript 1 corresponds to Sibony et al. (2024), 2 to Georgy et al. (2013), 3 to Yusof et al. (2013), 4 to Eggenberger et al. (2021), 5 to Martinet et al. (2023), 6 to Ekström et al. (2012), 7 to Yusof et al. (2022). Models without superscript are unpublished and have been calculated for this work.

Z	$v_{\mathrm{ini}}/v_{\mathrm{crit}}$	Initial mass of models													
1×10^{-5}	0	9^1	12^1	15^1	20^1	25^1	30^1	40^1	60^1	85^1	120^1	150^1	200^1	300^1	500^1
	0.4	9^1	12^1	15^1	20^1	25^1	30^1	40^1	60^1	85^1	120^1	150^1	200^1	300^1	500^1
0.002	0	9^2	12^2	15^2	20^2	25^2	32^2	40^2	60^2	85^2	120^2	150	200	300	
	0.4	9^2	12^2	15^2	20^2	25^2	32^2	40^2	60^2	85^2	120^2	150^3	200^3	300^3	
0.006	0	9^4	12^4	15^4	20^4	25^4	32^4	40^4	60^4	85^4	120^4	150^3	180^5	300^5	500^3
	0.4	9^4	12^4	15^4	20^4	25^4	32^4	40^4	60^4	85^4	120^4	150^3	200^3	300^3	500^3
0.014	0	9^6	12^6	15^6	20^6	25^6	32^6	40^6	60^6	85^6	120^6	150^3	200^3	300^3	500^3
	0.4	9^6	12^6	15^6	20^6	25^6	32^6	40^6	60^6	85^6	120^6	150^3	200^3	300^3	500^3
0.02	0	9^7	12^7	15^7	20^7	25^7	32^7	40^7	60^7	85^7	120^7	150^7	200^7	300^7	500
	0.4	9^7	12^7	15^7	20^7	25^7	32^7	40^7	60^7	85^7	120^7	150^7	200^7	300^7	

Appendix B

Data Tables

Table B.1: Initial mass ($M_{\rm ini}$), final total mass ($M_{\rm fin}$), helium core mass (M_α), CO core mass ($M_{\rm CO}$), H envelope mass ($M_{\rm H}^{\rm env}$), He envelope mass ($M_{\rm He}^{\rm env}$), followed by remnant and SN type of the models with $Z = 10^{-5}$ (EMP).

$M_{\rm ini}$	$v_{\rm ini}/v_{\rm crit}$	$M_{\rm fin}$	M_α	$M_{\rm CO}$	$M_{\rm H}^{\rm env}$	$M_{\rm He}^{\rm env}$	Remnant type	SN type
9	0	9.00	2.46	1.02	4.74	3.11	NS	Type IIP
9	0.4	9.00	2.68	1.12	4.20	3.51	NS	Type IIP
12	0	12.00	3.36	1.58	6.04	4.23	NS	Type IIP
12	0.4	12.00	3.46	1.59	5.33	4.81	NS	Type IIP
15	0	14.99	4.36	2.28	7.18	5.36	NS	Type IIP
15	0.4	14.99	5.20	2.63	5.80	5.48	NS	Type IIP
20	0	20.00	6.18	3.75	8.82	7.24	NS	Type IIP
20	0.4	20.00	5.47	2.98	6.82	8.27	NS	Type IIP
25	0	25.00	8.32	5.55	10.18	9.07	NS	Type IIP
25	0.4	25.00	8.50	5.52	7.92	10.48	NS	Type IIP
30	0	29.99	10.67	7.57	11.34	10.84	BH (NS)	Type IIP
30	0.4	22.84	7.67	4.81	4.23	10.68	NS	Type IIP
40	0	39.99	15.38	11.67	13.37	14.60	NS (BH)	Type IIP
40	0.4	39.84	5.47	3.14	8.49	20.58	NS	Type IIP
60	0	60.00	25.73	20.94	17.18	21.27	BH	Direct BH
60	0.4	56.61	17.46	13.42	10.58	24.36	BH	Direct BH
85	0	84.99	37.42	31.63	21.66	30.69	BH	Direct BH
85	0.4	57.22	44.28	37.36	2.13	14.67	BH	Direct BH
120	0	98.45	54.20	48.00	12.86	35.28	PPISN	Type IIP
120	0.4	86.62	68.53	59.50	2.88	20.02	PPISN	Type IIP
150	0	128.59	67.52	58.88	17.59	49.96	PPISN	Type IIP
150	0.4	131.84	94.72	86.62	7.43	37.03	PISN	Type IIP
200	0	168.21	93.16	83.24	19.43	64.24	PISN	Type IIP
200	0.4	158.24	134.54	123.50	2.90	27.29	PISN	Type IIP
300	0	245.66	142.38	117.67	22.37	89.36	PISN	Type IIP
300	0.4	282.38	266.28	247.63	1.06	22.14	BH	Direct BH
500	0	465.80	252.54	235.23	24.49	198.12	BH	Direct BH
500	0.4	462.66	433.15	404.05	1.62	36.09	BH	Direct BH

Table B.2: Initial mass (M_{ini}), final total mass (M_{fin}), helium core mass (M_α), CO core mass (M_{CO}), H envelope mass ($M_{\text{H}}^{\text{env}}$), He envelope mass ($M_{\text{He}}^{\text{env}}$), followed by remnant and SN type of the models with $Z = 0.002$ (SMC).

M_{ini}	$v_{\text{ini}}/v_{\text{crit}}$	M_{fin}	M_α	M_{CO}	$M_{\text{H}}^{\text{env}}$	$M_{\text{He}}^{\text{env}}$	Remnant type	SN type
9	0	8.89	2.49	1.00	4.65	3.09	NS	Type IIP
9	0.4	8.98	2.85	1.14	4.14	3.39	NS	Type IIP
12	0	11.91	3.60	1.73	5.88	4.03	NS	Type IIP
12	0.4	11.87	3.84	1.80	5.09	4.79	NS	Type IIP
15	0	14.78	4.60	2.41	6.91	5.27	NS	Type IIP
15	0.4	14.77	4.97	2.59	5.86	5.95	NS	Type IIP
20	0	19.70	6.53	4.00	8.44	7.01	NS	Type IIP
20	0.4	19.25	7.09	4.24	6.65	7.63	NS	Type IIP
25	0	24.40	8.47	5.66	9.52	8.92	NS	Type IIP
25	0.4	22.75	9.50	6.25	6.38	9.11	BH (NS)	Type IIP
32	0	23.90	11.77	8.59	5.64	9.31	NS (BH)	Type IIP
32	0.4	24.67	13.03	9.36	4.10	9.97	NS (BH)	Type IIP
40	0	29.55	14.92	11.39	5.74	11.96	NS (BH)	Type IIP
40	0.4	29.14	17.48	13.37	4.05	10.32	BH	Direct BH
60	0	37.91	25.19	20.43	4.08	12.58	BH	Direct BH
60	0.4	39.44	31.38	26.70	4.05	10.31	BH	Direct BH
85	0	48.75	37.53	32.26	3.00	12.12	BH	Direct BH
85	0.4	51.34	49.47	43.59	1.68	10.21	PPISN	Type IIL
120	0	64.15	55.65	49.57	1.75	11.56	PPISN	Type IIL
120	0.4	86.09	84.78	76.61	1.67	10.20	PISN	Type IIL
150	0	84.97	70.91	63.39	2.69	16.78	PISN	Type IIP
150	0.4	106.68	106.68	93.78	0.27	5.02	PISN	Type Ib
200	0	105.92	98.86	68.49	0.02	8.18	PISN	Type Ib
200	0.4	129.34	129.34	116.66	0.06	4.30	PISN	Type Ib
300	0	164.44	158.59	116.57	0.08	31.35	PISN	Type Ib
300	0.4	149.78	149.78	134.10	0.00	3.18	BH	Direct BH

Table B.3: Initial mass ($M_{\rm ini}$), final total mass ($M_{\rm fin}$), helium core mass (M_α), CO core mass ($M_{\rm CO}$), H envelope mass ($M_{\rm H}^{\rm env}$), He envelope mass ($M_{\rm He}^{\rm env}$), followed by remnant and SN type of the models with $Z = 0.006$ (LMC).

$M_{\rm ini}$	$v_{\rm ini}/v_{\rm crit}$	$M_{\rm fin}$	M_α	$M_{\rm CO}$	$M_{\rm H}^{\rm env}$	$M_{\rm He}^{\rm env}$	Remnant type	SN type
9	0	8.65	2.27	0.88	4.57	2.93	NS	Type IIP
9	0.4	8.80	2.56	1.00	4.16	3.44	NS	Type IIP
12	0	10.95	3.26	1.47	5.30	3.86	NS	Type IIP
12	0.4	11.25	3.81	1.77	4.68	4.11	NS	Type IIP
15	0	14.00	4.46	2.30	6.35	5.03	NS	Type IIP
15	0.4	14.15	5.05	2.68	5.43	5.58	NS	Type IIP
20	0	15.33	6.46	3.94	5.19	5.68	NS	Type IIP
20	0.4	13.80	7.13	4.33	3.04	5.58	NS	Type IIP
25	0	12.04	8.47	5.70	5.17	5.67	NS	Type IIP
25	0.4	12.42	9.35	6.28	1.18	4.09	BH (NS)	Type IIL
32	0	12.51	11.43	8.37	1.48	4.51	NS (BH)	Type IIL
32	0.4	13.99	13.43	9.91	1.18	4.08	NS (BH)	Type IIL
40	0	15.55	14.95	11.53	1.47	4.50	NS (BH)	Type IIL
40	0.4	19.41	18.89	14.89	0.09	2.36	BH	Direct BH
60	0	22.92	22.92	18.23	0.39	3.13	BH	Direct BH
60	0.4	33.03	33.03	28.25	0.09	2.35	BH	Direct BH
85	0	31.53	31.53	26.15	0.16	2.73	BH	Direct BH
85	0.4	35.93	35.93	29.93	0.09	2.35	BH	Direct BH
120	0	54.62	54.62	47.27	0.00	0.48	PPISN	Type Ic
120	0.4	52.58	52.58	45.08	0.08	2.32	PPISN	Type Ib
150	0	59.68	59.68	51.72	0.00	0.79	PPISN	Type Ib
150	0.4	45.67	45.67	38.70	0.08	2.31	BH	Direct BH
180	0	71.06	71.06	63.49	0.00	1.19	PISN	Type Ib
200	0.4	51.11	51.11	43.55	0.00	1.41	PPISN	Type Ib
300	0	91.35	91.35	82.30	0.00	1.13	PISN	Type Ib
300	0.4	54.14	54.14	46.45	0.00	0.88	PPISN	Type Ib
500	0	94.68	94.68	82.18	0.00	1.68	PISN	Type Ib
500	0.4	74.89	74.89	65.37	0.00	1.27	PISN	Type Ib

Table B.4: Initial mass (M_{ini}), final total mass (M_{fin}), helium core mass (M_{α}), CO core mass (M_{CO}), H envelope mass ($M_{\mathrm{H}}^{\mathrm{env}}$), He envelope mass ($M_{\mathrm{He}}^{\mathrm{env}}$), followed by remnant and SN type of the models with $Z = 0.014$ (solar).

M_{ini}	$v_{\mathrm{ini}}/v_{\mathrm{crit}}$	M_{fin}	M_{α}	M_{CO}	$M_{\mathrm{H}}^{\mathrm{env}}$	$M_{\mathrm{He}}^{\mathrm{env}}$	Remnant type	SN type
9	0	8.80	2.21	0.83	4.62	3.07	NS	Type IIP
9	0.4	8.58	2.92	1.18	3.61	3.34	NS	Type IIP
12	0	11.36	2.95	1.26	5.68	3.91	NS	Type IIP
12	0.4	10.31	3.83	1.83	4.08	3.56	NS	Type IIP
15	0	13.34	4.20	2.11	5.87	5.04	NS	Type IIP
15	0.4	11.19	5.01	2.69	3.38	4.01	NS	Type IIP
20	0	9.02	6.14	3.67	1.33	3.67	NS	Type IIL
20	0.4	7.55	7.04	4.36	3.38	4.01	NS	Type IIP
25	0	8.77	8.06	5.34	0.28	2.57	NS	Type Ib
25	0.4	9.91	9.59	6.54	0.15	2.33	BH (NS)	Type Ib
32	0	11.17	10.74	7.72	0.12	2.55	BH (NS)	Type Ib
32	0.4	10.21	10.21	7.05	0.15	2.33	BH (NS)	Type Ib
40	0	13.92	13.86	10.40	0.00	2.23	NS (BH)	Type Ib
40	0.4	12.41	12.41	9.01	0.03	2.01	NS (BH)	Type Ib
60	0	12.57	12.57	9.18	0.00	0.52	NS (BH)	Type Ib
60	0.4	18.07	18.07	13.97	0.00	0.51	BH	Direct BH
85	0	18.72	18.72	14.67	0.00	0.57	BH	Direct BH
85	0.4	26.49	26.49	21.47	0.00	0.54	BH	Direct BH
120	0	31.00	31.00	25.64	0.00	0.71	BH	Direct BH
120	0.4	19.12	19.12	14.87	0.00	0.60	BH	Direct BH
150	0	41.26	41.26	34.96	0.00	0.87	BH	Direct BH
150	0.4	20.31	20.31	16.10	0.00	0.68	BH	Direct BH
200	0	49.42	49.42	42.50	0.00	0.82	PPISN	Type Ib
200	0.4	22.01	22.01	17.57	0.00	0.60	BH	Direct BH
300	0	38.24	38.24	32.17	0.00	0.84	BH	Direct BH
300	0.4	24.01	24.01	19.43	0.00	0.63	BH	Direct BH
500	0	29.84	29.84	24.21	0.00	0.82	BH	Direct BH
500	0.4	25.91	25.91	21.05	0.00	0.70	BH	Direct BH

Table B.5: Initial mass (M_{ini}), final total mass (M_{fin}), helium core mass (M_α), CO core mass (M_{CO}), H envelope mass ($M_{\text{H}}^{\text{env}}$), He envelope mass ($M_{\text{He}}^{\text{env}}$), followed by remnant and SN type of the models with $Z = 0.02$ (supersolar).

M_{ini}	$v_{\text{ini}}/v_{\text{crit}}$	M_{fin}	M_α	M_{CO}	$M_{\text{H}}^{\text{env}}$	$M_{\text{He}}^{\text{env}}$	Remnant type	SN type
9	0	8.80	1.21	1.14	4.55	2.95	NS	Type IIP
9	0.4	8.74	1.83	1.31	4.05	3.12	NS	Type IIP
12	0	11.56	2.98	1.58	4.55	2.95	NS	Type IIP
12	0.4	10.36	3.68	2.14	4.05	3.12	NS	Type IIP
15	0	13.09	4.09	2.24	5.71	4.01	NS	Type IIP
15	0.4	10.83	5.22	3.09	4.08	3.50	NS	Type IIP
20	0	8.45	6.03	3.68	5.63	4.83	NS	Type IIP
20	0.4	7.27	7.14	4.66	3.15	3.70	NS	Type IIP
25	0	8.04	8.04	5.37	1.12	3.25	NS	Type IIL
25	0.4	9.08	9.08	6.67	0.01	1.22	BH (NS)	Type Ib
32	0	10.71	10.71	7.77	0.00	1.92	BH (NS)	Type Ib
32	0.4	9.80	9.80	7.16	0.00	1.07	BH (NS)	Type Ib
40	0	11.33	11.33	8.64	0.00	2.22	NS (BH)	Type Ib
40	0.4	11.63	11.63	8.97	0.00	0.32	NS (BH)	Type Ic
60	0	10.77	10.77	8.24	0.00	0.33	NS (BH)	Type Ic
60	0.4	12.87	12.87	9.93	0.00	0.40	NS (BH)	Type Ic
85	0	16.21	16.21	12.91	0.00	0.38	BH	Direct BH
85	0.4	16.64	16.64	13.25	0.00	0.39	BH	Direct BH
120	0	23.40	23.40	19.15	0.00	0.43	BH	Direct BH
120	0.4	22.26	22.26	18.05	0.00	0.42	BH	Direct BH
150	0	30.92	30.92	26.07	0.00	0.49	BH	Direct BH
200	0	35.65	35.65	30.02	0.00	0.63	BH	Direct BH
200	0.4	34.64	34.64	29.09	0.00	0.48	BH	Direct BH
300	0	22.23	22.23	18.08	0.00	0.69	BH	Direct BH
300	0.4	25.24	25.24	20.62	0.00	0.67	BH	Direct BH
500	0	25.55	25.55	20.31	0.00	0.67	BH	Direct BH
500	0.4	25.24	25.24	20.62	0.00	0.67	BH	Direct BH

Appendix C

Supernova type

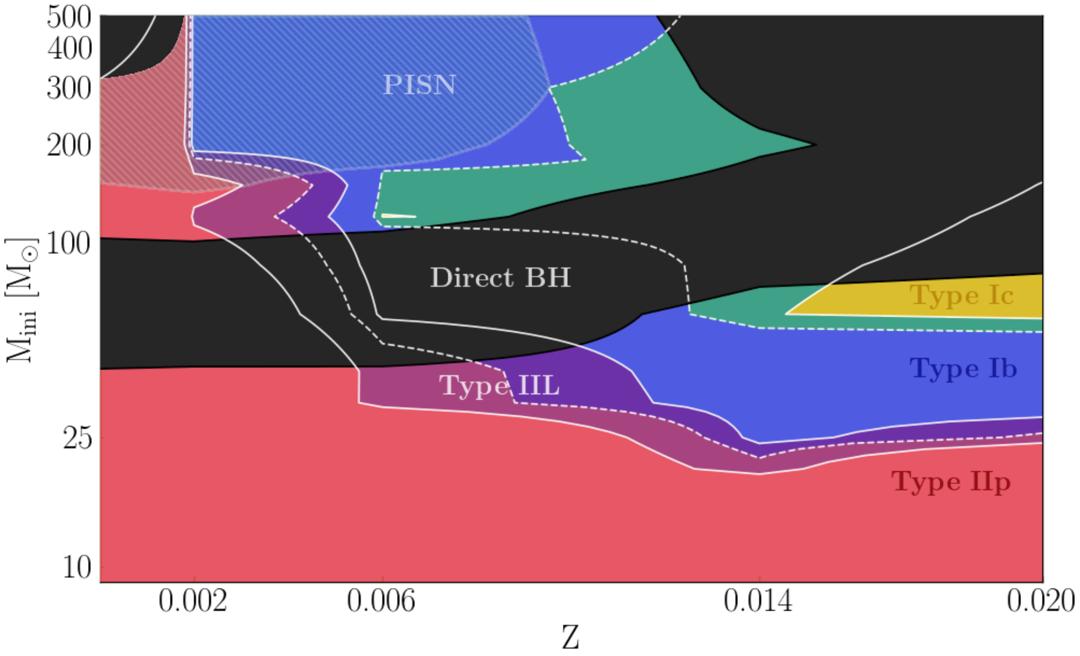

Figure C.1: Supernova types for non-rotating models using different definitions for hydrogen and helium free envelopes. Solid lines indicate the original choice of hydrogen/helium free threshold of 0.5 $M_\odot$, whereas the dotted lines use 1 $M_\odot$ as the threshold to define hydrogen/helium free stars.

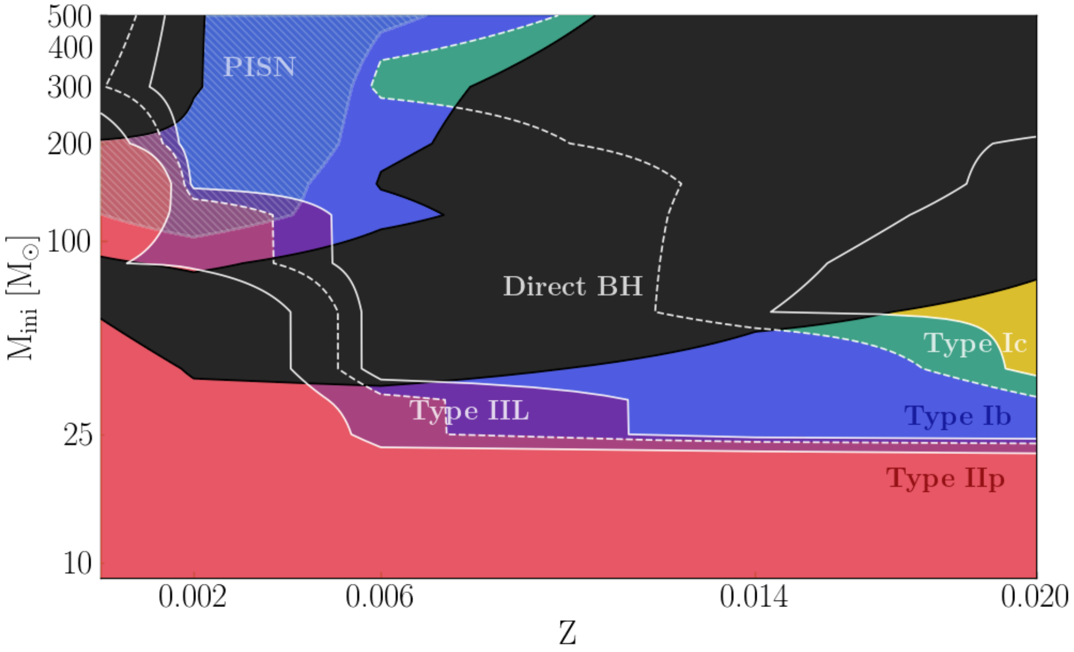

Figure C.2: Supernova types for rotating models using different definitions for hydrogen and helium free envelopes. Lines and regions have the same meaning as in Fig. C.1.

Appendix D

PISN types

Table D.1: Fraction of different supernovae types that are predicted to be PISN, calculated using the Salpeter IMF (Salpeter, 1955).

Z	Type IIP	Type IIL	Type Ib
Non-rotating			
10^{-5}	0.014		
0.002	0.004	0.424	1
0.006	0	0	0.476
0.014	0	0	0
0.02	0	0	0
Rotating			
10^{-5}	0.015		
0.002	0	0.510	1
0.006	0	0	0.030
0.014	0	0	0
0.02	0	0	0

Table D.2: Fraction of different supernovae types that are predicted to be PISN, calculated using the top-heavy IMF from Schneider et al. (2018).

Z	Type IIP	Type IIL	Type Ib
	Non-rotating		
10^{-5}	0.044		
0.002	0.011	0.467	1
0.006	0	0	0.552
0.014	0	0	0
0.02	0	0	0
	Rotating		
10^{-5}	0.040		
0.002	0	0.541	1
0.006	0	0	0.044
0.014	0	0	0
0.02	0	0	0

Table D.3: Fraction of massive stars per supernova type for PPISN and PISN, calculated using the IMF from Salpeter (1955) with $\alpha = 2.35$.

Z	Type IIP	Type IIL	Type Ib	Type Ic
Non-rotating				
10^{-5}	1	0	0	0
0.002	0.379	0.277	0.344	0
0.006	0	0	0.978	0.022
0.014	0	0	1	0
Rotating				
10^{-5}	1	0	0	0
0.002	0.041	0.645	0.315	0
0.006	0	0	1	0

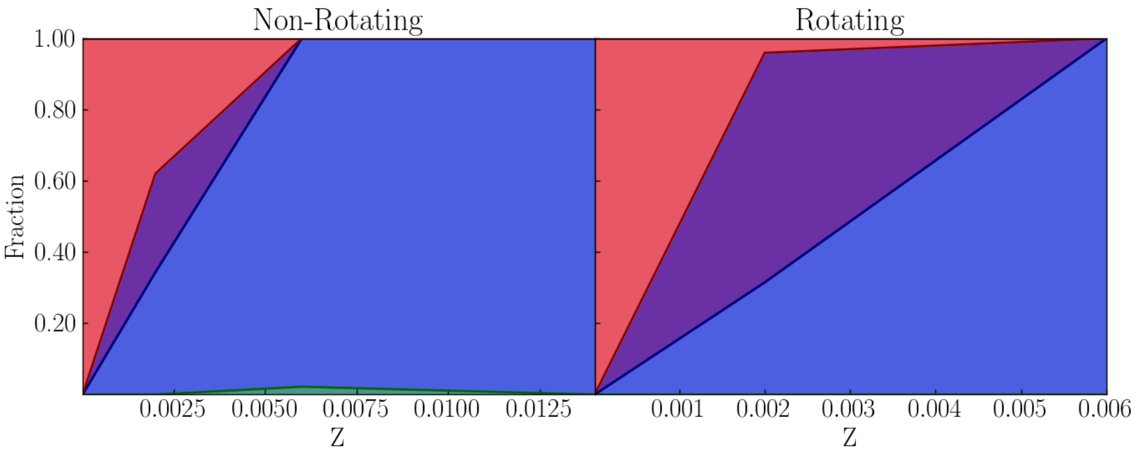

Figure D.1: Plot of data from Table D.3.

Table D.4: Fraction of massive stars per supernova type for PPISN and PISN, calculated using the top-heavy IMF from Schneider et al. (2018) with $\alpha = 1.9$.

Z	Type IIP	Type IIL	Type Ib	Type Ic
Non-rotating				
10^{-5}	1	0	0	0
0.002	0.326	0.250	0.424	0
0.006	0	0	0.982	0.018
0.014	0	0	1	0
Rotating				
10^{-5}	1	0	0	0
0.002	0.033	0.589	0.378	0
0.006	0	0	1	0

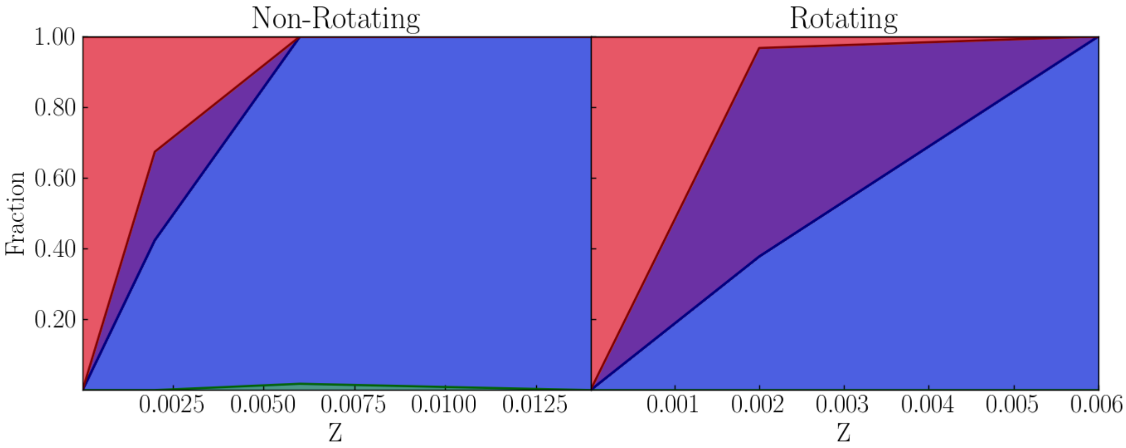

Figure D.2: Plot of data from Table D.4.

Bibliography

R. Abbott, T. Abbott, S. Abraham, F. Acernese, K. Ackley, C. Adams, R. Adhikari, V. Adya, C. Affeldt, M. Agathos, et al. Properties and astrophysical implications of the 150 $M_\odot$ binary black hole merger GW190521. *The Astrophysical Journal Letters*, 900(1):L13, 2020.

R. Abbott, T. Abbott, S. Abraham, F. Acernese, K. Ackley, A. Adams, C. Adams, R. Adhikari, V. Adya, C. Affeldt, et al. GWTC-2: compact binary coalescences observed by LIGO and Virgo during the first half of the third observing run. *Physical Review X*, 11(2):021053, 2021.

C. Angulo, M. Arnould, M. Rayet, P. Descouvemont, D. Baye, C. Leclercq-Willain, A. Coc, S. Barhoumi, P. Aguer, C. Rolfs, et al. A compilation of charged-particle induced thermonuclear reaction rates. *Nuclear Physics A*, 656 (1):3–183, 1999.

W. D. Arnett, C. Meakin, R. Hirschi, A. Cristini, C. Georgy, S. Campbell, L. J. Scott, E. A. Kaiser, M. Viallet, and M. Mocák. 3D simulations and MLT. I. Renzini's critique. *The Astrophysical Journal*, 882(1):18, 2019.

C. D. Bailyn, R. K. Jain, P. Coppi, and J. A. Orosz. The mass distribution of stellar black holes. *The Astrophysical Journal*, 499(1):367, 1998.

M. R. Bate. The statistical properties of stars and their dependence on metallicity. *Monthly Notices of the Royal Astronomical Society*, 484(2):2341–2361, 2019.

A. H. Batten. Some interesting massive spectroscopic binary systems. *Astronomical Journal, Vol. 73, p. 551-555 (1968)*, 73:551–555, 1968.

H. A. Bethe and J. R. Wilson. Revival of a stalled supernova shock by neutrino heating. *The Astrophysical Journal*, 295:14–23, 1985.

R. Bionta, G. Blewitt, C. Bratton, D. Casper, A. Ciocio, R. Claus, B. Cortez, M. Crouch, S. Dye, S. Errede, et al. Observation of a neutrino burst in coincidence with supernova 1987a in the large magellanic cloud. *Physical Review Letters*, 58(14):1494, 1987.

R. Björklund, J. Sundqvist, S. Singh, J. Puls, and F. Najarro. New predictions for radiation-driven, steady-state mass-loss and wind-momentum from hot, massive stars- III. Updated mass-loss rates for stellar evolution. *Astronomy & Astrophysics*, 676:A109, 2023.

E. Böhm-Vitense. Über die wasserstoffkonvektionszone in sternen verschiedener effektivtemperaturen und leuchtkräfte. Mit 5 textabbildungen. *Zeitschrift für Astrophysik, Vol. 46, p. 108*, 46:108, 1958.

I. A. Bonnell and M. R. Bate. Binary systems and stellar mergers in massive star formation. *Monthly Notices of the Royal Astronomical Society*, 362(3):915–920, 2005.

S. A. Brands, A. de Koter, J. M. Bestenlehner, P. A. Crowther, J. O. Sundqvist, J. Puls, S. M. Caballero-Nieves, M. Abdul-Masih, F. A. Driessen, M. García, et al. The R136 star cluster dissected with Hubble Space Telescope/STIS-III. The most massive stars and their clumped winds. *Astronomy & Astrophysics*, 663:A36, 2022.

V. Bromm, P. S. Coppi, and R. B. Larson. Forming the first stars in the universe: the fragmentation of primordial gas. *The Astrophysical Journal*, 527(1):L5, 1999.

B. W. Carroll and D. A. Ostlie. *An introduction to modern astrophysics.* Cambridge University Press, 2017.

J. P. Cassinelli, J. S. Mathis, and B. D. Savage. Central object of the 30 Doradus nebula, a supermassive star. *Science*, 212(4502):1497–1501, 1981.

G. R. Caughlan, W. A. Fowler, M. J. Harris, and B. A. Zimmerman. Tables of thermonuclear reaction rates for low-mass nuclei (1 ¡ Z¡ 14). *Atomic data and nuclear data tables*, 32(2):197–233, 1985.

B. Chaboyer and J.-P. Zahn. Effect of horizontal turbulent diffusion on transport by meridional circulation. *Astronomy and Astrophysics (ISSN 0004-6361), vol. 253, no. 1, Jan. 1992, p. 173-177.*, 253:173–177, 1992.

S. Chandrasekhar. *Hydrodynamic and hydromagnetic stability.* Courier Corporation, 1961.

A. Chieffi and M. Limongi. The presupernova core mass–radius relation of massive stars: Understanding its formation and evolution. *The Astrophysical Journal*, 890(1):43, 2020.

A. Chieffi, M. Limongi, and O. Straniero. The evolution of a 25 $M_\odot$ star from the main sequence up to the onset of the iron core collapse. *The Astrophysical Journal*, 502(2):737, 1998.

R. Chini, V. Hoffmeister, A. Nasseri, O. Stahl, and H. Zinnecker. A spectroscopic survey on the multiplicity of high-mass stars. *Monthly Notices of the Royal Astronomical Society*, 424(3):1925–1929, 2012.

S. Chon, K. Omukai, and R. Schneider. Transition of the initial mass function in the metal-poor environments. *Monthly Notices of the Royal Astronomical Society*, 508(3):4175–4192, 2021.

R. C. Coelho, M. O. Calvão, R. R. Reis, and B. B. Siffert. Standardization of type Ia supernovae. *European Journal of Physics*, 36(1):015007, 2014.

P. S. Conti and D. Ebbets. Spectroscopic studies of O-type stars. VII. Rotational velocities v sin i and evidence for macroturbulent motions. *Astrophysical Journal, Vol. 213, p. 438-447*, 213:438–447, 1977.

P. A. Crowther. Wind properties of Wolf-Rayet stars at low metallicity: Sk 41 (SMC). *Astronomy and Astrophysics, v. 356, p. 191-199 (2000)*, 356:191–199, 2000.

P. A. Crowther, O. Schnurr, R. Hirschi, N. Yusof, R. J. Parker, S. P. Goodwin, and H. A. Kassim. The R136 star cluster hosts several stars whose individual masses greatly exceed the accepted 150 $M_\odot$ stellar mass limit. *Monthly Notices of the Royal Astronomical Society*, 408(2):731–751, 2010.

R. M. Crutcher. Magnetic fields in molecular clouds. *Annual Review of Astronomy and Astrophysics*, 50:29–63, 2012.

E. De Donder and D. Vanbeveren. The chemical evolution of the solar neighbourhood: the effect of binaries. *New Astronomy*, 7(2):55–84, 2002.

C. de Jager, H. Nieuwenhuijzen, and K. Van Der Hucht. Mass loss rates in the Hertzsprung-Russell diagram. *Astronomy and Astrophysics Supplement Series (ISSN 0365-0138), vol. 72, no. 2, Feb. 1988, p. 259-289.*, 72:259–289, 1988.

L. Dessart, D. J. Hillier, C. Li, and S. Woosley. On the nature of supernovae Ib and Ic. *Monthly Notices of the Royal Astronomical Society*, 424(3):2139–2159, 2012.

P. Dufton, S. Smartt, J. Lee, R. Ryans, I. Hunter, C. Evans, A. Herrero, C. Trundle, D. Lennon, M. Irwin, et al. The VLT-FLAMES survey of massive stars:

stellar parameters and rotational velocities in NGC 3293, NGC 4755 and NGC 6611. *Astronomy & Astrophysics*, 457(1):265–280, 2006.

A. Eddington. Circulating currents in rotating stars. *The Observatory, Vol. 48, p. 73-75 (1925)*, 48:73–75, 1925.

P. Eggenberger, S. Ekström, C. Georgy, S. Martinet, C. Pezzotti, D. Nandal, G. Meynet, G. Buldgen, S. Salmon, L. Haemmerlé, et al. Grids of stellar models with rotation-VI. Models from 0.8 to 120 $M_\odot$ at a metallicity Z= 0.006. *Astronomy & Astrophysics*, 652:A137, 2021.

P. P. Eggleton. Approximations to the radii of Roche lobes. *Astrophysical Journal, Part 1 (ISSN 0004-637X), vol. 268, May 1, 1983, p. 368, 369.*, 268:368, 1983.

S. Ekström. Massive star modeling and nucleosynthesis. *Frontiers in Astronomy and Space Sciences*, 8:617765, 2021.

S. Ekström, C. Georgy, P. Eggenberger, G. Meynet, N. Mowlavi, A. Wyttenbach, A. Granada, T. Decressin, R. Hirschi, U. Frischknecht, et al. Grids of stellar models with rotation-I. Models from 0.8 to 120 $M_\odot$ at solar metallicity (Z= 0.014). *Astronomy & Astrophysics*, 537:A146, 2012.

J. Eldridge and J. S. Vink. Implications of the metallicity dependence of Wolf-Rayet winds. *Astronomy & Astrophysics*, 452(1):295–301, 2006.

J. Eldridge, E. R. Stanway, L. Xiao, L. McClelland, G. Taylor, M. Ng, S. M. Greis, and J. Bray. Binary population and spectral synthesis version 2.1: construction, observational verification, and new results. *Publications of the Astronomical Society of Australia*, 34:e058, 2017.

A. Endal and S. Sofia. The evolution of rotating stars. II-Calculations with time-dependent redistribution of angular momentum for 7 - 10 solar mass stars.

Astrophysical Journal, Part 1, vol. 220, Feb. 15, 1978, p. 279-290., 220:279–290, 1978.

T. Ertl, H. Janka, T. Woosley, S.Eand Sukhbold, and M. Ugliano. A two-parameter criterion for classifying the explodability of massive stars by the neutrino-driven mechanism. *The Astrophysical Journal*, 818(2):124, 2016.

C. J. Evans, S. Smartt, J.-K. Lee, D. Lennon, A. Kaufer, P. Dufton, C. Trundle, A. Herrero, S. Simón-Díaz, A. de Koter, et al. The VLT-FLAMES survey of massive stars: Observations in the galactic clusters NGC 3293, NGC 4755 and NGC 6611. *Astronomy & Astrophysics*, 437(2):467–482, 2005.

R. Farmer, M. Renzo, S. de Mink, P. Marchant, and S. Justham. Mind the gap: the location of the lower edge of the pair-instability supernova black hole mass gap. *The Astrophysical Journal*, 887(1):53, 2019.

R. Farmer, M. Renzo, S. de Mink, M. Fishbach, and S. Justham. Constraints from gravitational-wave detections of binary black hole mergers on the 12C (α, γ) 16O rate. *The Astrophysical Journal Letters*, 902(2):L36, 2020.

W. M. Farr, N. Sravan, A. Cantrell, L. Kreidberg, C. D. Bailyn, I. Mandel, and V. Kalogera. The mass distribution of stellar-mass black holes. *The Astrophysical Journal*, 741(2):103, 2011.

D. F. Figer. An upper limit to the masses of stars. *Nature*, 434(7030):192–194, 2005.

W. A. Fowler and F. Hoyle. Neutrino processes and pair formation in massive stars and supernovae. *Astrophysical Journal Supplement, vol. 9, p. 201 (1964)*, 9:201, 1964.

T. Fragos, J. J. Andrews, S. S. Bavera, C. P. Berry, S. Coughlin, A. Dotter, P. Giri, V. Kalogera, A. Katsaggelos, K. Kovlakas, et al. Posydon: A generalpurpose population synthesis code with detailed binary-evolution simulations. *The Astrophysical Journal Supplement Series*, 264(2):45, 2023.

L. H. Frey, C. L. Fryer, and P. A. Young. Can stellar mixing explain the lack of type Ib supernovae in long-duration gamma-ray bursts? *The Astrophysical Journal Letters*, 773(1):L7, 2013.

I. Fukuda. A statistical study of rotational velocities of the stars. *Publications of the Astronomical Society of the Pacific*, 94(558):271, 1982.

A. Gal-Yam. Luminous supernovae. *Science*, 337(6097):927–932, 2012.

A. Gal-Yam, P. Mazzali, E. Ofek, P. Nugent, S. Kulkarni, M. Kasliwal, R. Quimby, A. Filippenko, S. Cenko, R. Chornock, et al. Supernova 2007bi as a pair-instability explosion. *Nature*, 462(7273):624–627, 2009.

C. Georgy. Yellow supergiants as supernova progenitors: an indication of strong mass loss for red supergiants? *Astronomy & Astrophysics*, 538:L8, 2012.

C. Georgy, G. Meynet, R. Walder, D. Folini, and A. Maeder. The different progenitors of type Ib, Ic SNe, and of GRB. *Astronomy & Astrophysics*, 502 (2):611–622, 2009.

C. Georgy, S. Ekström, P. Eggenberger, G. Meynet, L. Haemmerlé, Maederandré, A. Granada, J. H. Groh, R. Hirschi, N. Mowlavi, et al. Grids of stellar models with rotation-III. Models from 0.8 to 120 $M_{\odot}$ at a metallicity Z= 0.002. *Astronomy & Astrophysics*, 558:A103, 2013.

G. Gräfener and W.-R. Hamann. Mass loss from late-type WN stars and its Z-dependence- Very massive stars approaching the Eddington limit. *Astronomy & Astrophysics*, 482(3):945–960, 2008.

L. Haemmerlé, P. Eggenberger, G. Meynet, Maederandré, and C. Charbonnel.

Massive star formation by accretion-I. disc accretion. *Astronomy & Astrophysics*, 585:A65, 2016.

A. Heger, N. Langer, and S. Woosley. Presupernova evolution of rotating massive stars. I. numerical method and evolution of the internal stellar structure. *The Astrophysical Journal*, 528(1):368, 2000.

A. Heger, A. Fryer, S. Woosley, N. Langer, and D. Hartmann. How massive single stars end their life. *The Astrophysical Journal*, 591(1):288, 2003.

S. Hirano, T. Hosokawa, N. Yoshida, H. Umeda, K. Omukai, G. Chiaki, and H. W. Yorke. One hundred first stars: protostellar evolution and the final masses. *The Astrophysical Journal*, 781(2):60, 2014.

K. Hirata, T. Kajita, M. Koshiba, M. Nakahata, Y. Oyama, N. Sato, A. Suzuki, M. Takita, Y. Totsuka, T. Kifune, et al. Observation of a neutrino burst from the supernova sn1987a. *Physical Review Letters*, 58(14):1490, 1987.

R. Holt, B. W. Filippone, and S. C. Pieper. Impact of O 16 (γ, α) C 12 measurements on the C 12 (α, γ) O 16 astrophysical reaction rate. *Physical Review C*, 99(5):055802, 2019.

I. D. Howarth, K. W. Siebert, G. A. Hussain, and R. K. Prinja. Cross-correlation characteristics of OB stars from IUE spectroscopy. *Monthly Notices of the Royal Astronomical Society*, 284(2):265–285, 1997.

W. Huang, D. R. Gies, and M. McSwain. A stellar rotation census of b stars: from zams to tams. *The Astrophysical Journal*, 722(1):605, 2010.

I. Iben. Stellar evolution. I. the approach to the main sequence. *Astrophysical Journal, vol. 141, p. 993*, 141:993, 1965.

C. Iliadis. *Nuclear physics of stars.* John Wiley & Sons, 2015.

H.-T. Janka. Neutrino emission from supernovae. *Handbook of Supernovae*, page 1575, 2017.

H.-T. Janka and E. Müller. Neutrino-driven type-II supernova explosions and the role of convection. *Physics Reports*, 256(1-3):135–156, 1995.

S. Jones, R. Hirschi, K. Nomoto, T. Fischer, F. X. Timmes, F. Herwig, B. Paxton, H. Toki, T. Suzuki, G. Martinez-Pinedo, et al. Advanced burning stages and fate of 8-10 $M_\odot$ stars. *The Astrophysical Journal*, 772(2):150, 2013.

P. G. Jonker, K. Kaur, N. Stone, and M. A. Torres. The observed mass distribution of galactic black hole LMXBs is biased against massive black holes. *The Astrophysical Journal*, 921(2):131, 2021.

E. Keto and K. Wood. Observations on the formation of massive stars by accretion. *The Astrophysical Journal*, 637(2):850, 2006.

R. Kippenhahn, A. Weigert, and E. Hofmeister. Methods in computational physics, vol. 7, methods for calculating stellar evolution, 1967.

R. Kippenhahn, A. Weigert, and A. Weiss. *Stellar structure and evolution*, volume 192. Springer, 1990.

C. Kobayashi. Inhomogeneous chemical enrichment in the galactic halo. *Proceedings of the International Astronomical Union*, 11(S317):57–63, 2015.

C. Kobayashi, A. I. Karakas, and M. Lugaro. The origin of elements from carbon to uranium. *The Astrophysical Journal*, 900(2):179, 2020.

K. Köhler, N. Langer, A. de Koter, S. de Mink, P. Crowther, C. Evans, G. Gräfener, H. Sana, D. Sanyal, F. Schneider, et al. The evolution of rotating very massive stars with LMC composition. *Astronomy & Astrophysics*, 573:A71, 2015.

M. R. Krumholz and C. McKee. A minimum column density of 1 g cm-2 for massive star formation. *Nature*, 451(7182):1082–1084, 2008.

M. R. Krumholz, C. F. McKee, and R. I. Klein. The formation of stars by gravitational collapse rather than competitive accretion. *Nature*, 438(7066): 332–334, 2005.

N. Langer. Presupernova evolution of massive single and binary stars. *Annual Review of Astronomy and Astrophysics*, 50(1):107–164, 2012.

R. B. Larson. Mass spectra of young stars. *Monthly Notices of the Royal Astronomical Society*, 200(2):159–174, 1982.

S. Larson, R. B.and Starrfield. On the formation of massive stars and the upper limit of stellar masses. *Astronomy and Astrophysics, Vol. 13, p. 190-197*, 13: 190–197, 1971.

J. Li, C. Liu, Z.-Y. Zhang, H. Tian, X. Fu, J. Li, and Z.-Q. Yan. Stellar initial mass function varies with metallicity and time. *Nature*, 613(7944):460–462, 2023.

W. Li, J. Leaman, R. Chornock, A. V. Filippenko, D. Poznanski, M. Ganeshalingam, X. Wang, M. Modjaz, S. Jha, R. J. Foley, et al. Nearby supernova rates from the Lick Observatory Supernova Search–II. the observed luminosity functions and fractions of supernovae in a complete sample. *Monthly Notices of the Royal Astronomical Society*, 412(3):1441–1472, 2011.

Y.-Q. Liu, M. Modjaz, F. B. Bianco, and O. Graur. Analyzing the largest spectroscopic data set of stripped supernovae to improve their identifications and constrain their progenitors. *The Astrophysical Journal*, 827(2):90, 2016.

A. Maeder. Stellar evolution with rotation. II. a new approach for shear mixing. *Astronomy and Astrophysics, v. 321, p. 134-144*, 321:134–144, 1997.

A. Maeder. *Physics, formation and evolution of rotating stars.* Springer Science & Business Media, 2008.

A. Maeder and G. Meynet. Stellar evolution with rotation. VI. the Eddington and Omega-limits, the rotational mass loss for OB and LBV stars. *Astronomy and Astrophysics*, 361:159–166, 2000a.

A. Maeder and G. Meynet. The evolution of rotating stars. *Annual Review of Astronomy and Astrophysics*, 38(1):143–190, 2000b.

P. Marchant and J. Bodensteiner. The evolution of massive binary stars. *Annual Review of Astronomy and Astrophysics*, 62, 2023.

P. Marchant, N. Langer, P. Podsiadlowski, T. M. Tauris, and T. J. Moriya. A new route towards merging massive black holes. *Astronomy & Astrophysics*, 588:A50, 2016.

M. Marks, P. Kroupa, J. Dabringhausen, and M. S. Pawlowski. Evidence for top-heavy stellar initial mass functions with increasing density and decreasing metallicity. *Monthly Notices of the Royal Astronomical Society*, 422(3):2246–2254, 2012.

S. Martinet, G. Meynet, S. Ekström, C. Georgy, and R. Hirschi. Very massive star models-I. impact of rotation and metallicity and comparisons with observations. *Astronomy & Astrophysics*, 679:A137, 2023.

C. F. McKee and J. C. Tan. The formation of the first stars. II. radiative feedback processes and implications for the initial mass function. *The Astrophysical Journal*, 681(2):771, 2008.

G. Meynet and A. Maeder. Stellar evolution with rotation. I. the computational method and the inhibiting effect of the mu-gradient. *Astronomy and Astrophysics, v. 321, p. 465-476*, 321:465–476, 1997.

G. Meynet, M. Arnould, N. Prantzos, and G. Paulus. Contribution of wolf-rayet stars to the synthesis of ^{26}Al I. the gamma-ray connection. *Astronomy and Astrophysics, v. 320, p. 460-468*, 320:460–468, 1997.

G. Meynet, V. Chomienne, S. Ekström, C. Georgy, A. Granada, J. Groh, A. Maeder, P. Eggenberger, E. Levesque, and P. Massey. Impact of mass-loss on the evolution and pre-supernova properties of red supergiants. *Astronomy & Astrophysics*, 575:A60, 2015.

M. Mokiem, A. de Koter, J. Vink, J. Puls, C. Evans, S. Smartt, P. Crowther, A. Herrero, N. Langer, D. Lennon, et al. The empirical metallicity dependence of the mass-loss rate of O-and early B-type stars. *Astronomy & Astrophysics*, 473(2):603–614, 2007.

T. J. Moriya, J.-a. Jiang, N. Yasuda, M. Kokubo, K. Kawana, K. Maeda, Y.-C. Pan, R. M. Quimby, N. Suzuki, I. Takahashi, et al. Constraints on the rate of supernovae lasting for more than a year from Subaru/Hyper Suprime-Cam. *The Astrophysical Journal*, 908(2):249, 2021.

B. Müller, A. Heger, D. Liptai, and J. Cameron. A simple approach to the supernova progenitor–explosion connection. *Monthly Notices of the Royal Astronomical Society*, 460(1):742–764, 2016.

L. J. Murphy, J. H. Groh, E. Farrell, G. Meynet, S. Ekström, S. Tsiatsiou, A. Hackett, and S. Martinet. Ionizing photon production of Population III stars: effects of rotation, convectionand initial mass function. *Monthly Notices of the Royal Astronomical Society*, 506(4):5731–5749, 2021.

A. Myers, C. McKee, A. Cunningham, R. Klein, and M. Krumholz. The fragmentation of magnetized, massive star-forming cores with radiative feedback. *The Astrophysical Journal*, 766(2):97, 2013.

F. Nakamura and M. Umemura. On the initial mass function of population III stars. *The Astrophysical Journal*, 548(1):19, 2001.

K. Nomoto, C. Kobayashi, and N. Tominaga. Nucleosynthesis in stars and the chemical enrichment of galaxies. *Annual Review of Astronomy and Astrophysics*, 51(1):457–509, 2013.

T. Nugis and H. Lamers. Mass-loss rates of wolf-rayet stars as a function of stellar parameters. *Astronomy and Astrophysics, Vol. 360, p. 227-244*, 360:227–244, 2000.

E. O'Connor and C. D. Ott. Black hole formation in failing core-collapse supernovae. *The Astrophysical Journal*, 730(2):70, 2011.

M. S. Oey and C. Clarke. Statistical confirmation of a stellar upper mass limit. *The Astrophysical Journal*, 620(1):L43, 2005.

T. Ohkubo, K. Nomoto, H. Umeda, N. Yoshida, and S. Tsuruta. Evolution of very massive population III stars with mass accretion from pre-main sequence to collapse. *The Astrophysical Journal*, 706(2):1184, 2009.

B. Paczynski and R. Sienkiewicz. Evolution of close binaries VIII. mass exchange on the dynamical time scale. *Acta Astronomica, Vol. 22, p. 73-91*, 22:73–91, 1972.

T. Padmanabhan. *Theoretical astrophysics: volume 2, stars and stellar systems.* Cambridge University Press, 2000.

R. Patton and T. Sukhbold. Towards a realistic explosion landscape for binary population synthesis. *Monthly Notices of the Royal Astronomical Society*, 499 (2):2803–2816, 2020.

T. Peters, R. Klessen, M. Mac Low, and R. Banerjee. Limiting accretion onto massive stars by fragmentation-induced starvation. *The Astrophysical Journal*, 725(1):134, 2010.

A. C. Phillips. *The physics of stars.* John Wiley & Sons, 2013.

P. Podsiadlowski, P. Joss, and J. Hsu. Presupernova evolution in massive interacting binaries. *Astrophysical Journal, Part 1 (ISSN 0004-637X), vol. 391, no. 1, May 20, 1992, p. 246-264.*, 391:246–264, 1992.

S. F. Portegies Zwart, S. L. McMillan, and M. Gieles. Young massive star clusters. *Annual review of astronomy and astrophysics*, 48:431–493, 2010.

N. Prantzos and R. Diehl. Radioactive 26Al in the galaxy: observations versus theory. *Physics Reports*, 267(1):1–69, 1996.

T. Preibisch, G. Weigelt, and H. Zinnecker. Multiplicity of massive stars. In *Symposium-International Astronomical Union*, volume 200, pages 69–78. Cambridge University Press, 2001.

D. Reimers. Circumstellar envelopes and mass loss of red giant stars. In *Problems in stellar atmospheres and envelopes*, pages 229–256. Springer, 1975.

E. E. Salpeter. The luminosity function and stellar evolution. *Astrophysical Journal, vol. 121, p. 161*, 121:161, 1955.

H. Sana, S. De Mink, A. de Koter, N. Langer, C. Evans, M. Gieles, E. Gosset, R. Izzard, J.-B. Le Bouquin, and F. Schneider. Binary interaction dominates the evolution of massive stars. *Science*, 337(6093):444–446, 2012.

A. A. Sander and J. S. Vink. On the nature of massive helium star winds and Wolf-Rayet-type mass-loss. *Monthly Notices of the Royal Astronomical Society*, 499(1):873–892, 2020.

D. Sanyal, L. Grassitelli, N. Langer, and J. M. Bestenlehner. Massive main-sequence stars evolving at the Eddington limit. *Astronomy & Astrophysics*, 580:A20, 2015.

K. Sato. Supernova explosion and neutral currents of weak interaction. *Progress of Theoretical Physics*, 54(5):1325–1338, 1975.

R. Scaramella, J. Amiaux, Y. Mellier, C. Burigana, C. Carvalho, J.-C. Cuillandre, A. Da Silva, A. Derosa, J. Dinis, E. Maiorano, et al. Euclid preparation-I. the Euclid wide survey. *Astronomy & Astrophysics*, 662:A112, 2022.

F. R. N. Schneider, R. G. Izzard, S. E. de Mink, N. Langer, Stolteandrea, A. de Koter, V. V. Gvaramadze, B. Hußmann, A. Liermann, and H. Sana. Ages of young star clusters, massive blue stragglersand the upper mass limit of stars: analyzing age-dependent stellar mass functions. *The Astrophysical Journal*, 780(2):117, 2013.

F. R. N. Schneider, H. Sana, C. Evans, J. Bestenlehner, N. Castro, L. Fossati, G. Gräfener, N. Langer, O. Ramírez-Agudelo, C. Sabín-Sanjulián, et al. An excess of massive stars in the local 30 Doradus starburst. *Science*, 359(6371): 69–71, 2018.

F. R. N. Schneider, P. Podsiadlowski, and B. Müller. Pre-supernova evolution, compact-object massesand explosion properties of stripped binary stars. *Astronomy & Astrophysics*, 645:A5, 2021.

M. Schwarzschild. Structure and evolution of the stars. *Structure and Evolution of Stars. Martin Schwarzschild. ISBN: 9780691080444. Princeton University Press*, 1958.

Y. Sibony, K. G. Shepherd, N. Yusof, R. Hirschi, C. Chambers, S. Tsiatsiou, D. Nandal, L. Sciarini, F. D. Moyano, J. Bétrisey, et al. Grids of stellar models with rotation VIII: Models from 1.7 to 120 $M_\odot$ at metallicity $Z = 10^{-5}$. *Astronomy & Astrophysics*, 690:A91, 2024.

L. Siess. Evolution of massive AGB stars- I. Carbon burning phase. *Astronomy & Astrophysics*, 448(2):717–729, 2006.

N. Smith, W. Li, A. V. Filippenko, and R. Chornock. Observed fractions of core-collapse supernova types and initial masses of their single and binary progenitor stars. *Monthly Notices of the Royal Astronomical Society*, 412(3):1522–1538, 2011.

C.-Y. Song and T. Liu. Long-duration gamma-ray burst progenitors and magnetar formation. *The Astrophysical Journal*, 952(2):156, 2023.

D. Spergel, N. Gehrels, C. Baltay, D. Bennett, J. Breckinridge, M. Donahue, A. Dressler, B. Gaudi, T. Greene, O. Guyon, et al. Wide-field infrared survey telescope-astrophysics focused telescope assets WFIRST-AFTA 2015 report. 2015.

H. Spinka and H. Winkler. Experimental determination of the total reaction cross section of the stellar nuclear reaction 16O + 16O. *Nuclear Physics A*, 233(2): 456–494, 1974.

S. W. Stahler and F. Palla. *The formation of stars*. John Wiley & Sons, 2008.

E. R. Stanway and J. J. Eldridge. Initial mass function variations cannot explain the ionizing spectrum of low metallicity starbursts. *Astronomy & Astrophysics*, 621:A105, 2019.

D. Sugimoto and M. Y. Fujimoto. Why stars become red giants. *The Astrophysical Journal*, 538(2):837, 2000.

T. Sukhbold and S. Woosley. The compactness of presupernova stellar cores. *The Astrophysical Journal*, 783(1):10, 2014.

T. Sukhbold, T. Ertl, S. Woosley, J. M. Brown, and H.-T. Janka. Core-collapse supernovae from 9 to 120 solar masses based on neutrino-powered explosions. *The Astrophysical Journal*, 821(1):38, 2016.

P. Sweet. The importance of rotation in stellar evolution. *Monthly Notices of the Royal Astronomical Society*, 110(6):548–558, 1950.

R. Sylvester, C. Skinner, and M. Barlow. Silicate and hydrocarbon emission from Galactic M supergiants. *Monthly Notices of the Royal Astronomical Society*, 301(4):1083–1094, 1998.

K. Takahashi. The low detection rate of pair-instability supernovae and the effect of the core carbon fraction. *The Astrophysical Journal*, 863(2):153, 2018.

J. C. Tan, M. T. Beltrán, P. Caselli, F. Fontani, A. Fuente, M. R. Krumholz, C. F. McKee, and Stolteandrea. Massive star formation. *Protostars and Planets VI*, 149(6), 2014.

T. S. Tanvir and M. R. Krumholz. The metallicity dependence of the stellar initial mass function. *Monthly Notices of the Royal Astronomical Society*, 527 (3):7306–7316, 2024.

C. Tur, A. Heger, and S. M. Austin. On the sensitivity of massive star nucleosynthesis and evolution to solar abundances and to uncertainties in helium-burning reaction rates. *The Astrophysical Journal*, 671(1):821, 2007.

M. Ugliano, H.-T. Janka, A. Marek, and A. Arcones. Progenitor-explosion connection and remnant birth masses for neutrino-driven supernovae of iron-core progenitors. *The Astrophysical Journal*, 757(1):69, 2012.

J. T. van Loon, M. Groenewegen, A. de Koter, N. Trams, L. Waters, A. Zijlstra, P. Whitelock, and C. Loup. Mass-loss rates and luminosity functions of dust-enshrouded agb stars and red supergiants in the lmc. *Astronomy and Astrophysics*, 351:559–572, 1999.

J. T. van Loon, M.-R. Cioni, A. A. Zijlstra, and C. Loup. An empirical formula for the mass-loss rates of dust-enshrouded red supergiants and oxygen-rich Asymptotic Giant Branch stars. *Astronomy & Astrophysics*, 438(1):273–289, 2005.

J. S. Vink. Theory and diagnostics of hot star mass loss. *Annual Review of Astronomy and Astrophysics*, 60:203–246, 2022.

J. S. Vink, A. de Koter, and H. Lamers. Mass-loss predictions for O and B stars as a function of metallicity. *Astronomy & Astrophysics*, 369(2):574–588, 2001.

J. S. Vink, E. R. Higgins, A. A. Sander, and G. N. Sabhahit. Maximum black hole mass across cosmic time. *Monthly Notices of the Royal Astronomical Society*, 504(1):146–154, 2021.

H. von Zeipel. The radiative equilibrium of a rotating system of gaseous masses. *Monthly Notices of the Royal Astronomical Society, Vol. 84, p. 665-683*, 84: 665–683, 1924.

T. A. Weaver. The structure of supernova shock waves. *Astrophysical Journal Supplement Series, vol. 32, Oct. 1976, p. 233-282.*, 32:233–282, 1976.

C. Weidner and P. Kroupa. Evidence for a fundamental stellar upper mass limit from clustered star formation. *Monthly Notices of the Royal Astronomical Society*, 348(1):187–191, 2004.

S. Wellstein and N. Langer. Implications of massive close binaries for black hole formation and supernovae. *Astron. Astrophys*, 350:148–162, 1999.

E. R. Winch, J. S. Vink, E. R. Higgins, and G. N. Sabhahitf. Predicting the heaviest black holes below the pair instability gap. *Monthly Notices of the Royal Astronomical Society*, 529(3):2980–3002, 2024.

K. M. Wollenberg, S. C. Glover, P. C. Clark, and R. S. Klessen. Formation sites of Population III star formation: The effects of different levels of rotation and turbulence on the fragmentation behaviour of primordial gas. *Monthly Notices of the Royal Astronomical Society*, 494(2):1871–1893, 2020.

S. Woosley. Pulsational pair-instability supernovae. *The Astrophysical Journal*, 836(2):244, 2017.

S. Woosley and A. Heger. The pair-instability mass gap for black holes. *The Astrophysical Journal Letters*, 912(2):L31, 2021.

S. E. Woosley and T. Janka. The physics of core-collapse supernovae. *Nature Physics*, 1(3):147–154, 2005.

S. E. Woosley, W. D. Arnett, and D. D. Clayton. The explosive burning of oxygen and silicon. *Astrophysical Journal Supplement*, 1973.

S. E. Woosley, A. Heger, and T. A. Weaver. The evolution and explosion of massive stars. *Reviews of modern physics*, 74(4):1015, 2002.

M. Yang, A. Z. Bonanos, B. Jiang, E. Zapartas, J. Gao, Y. Ren, M. I. Lam, T. Wang, G. Maravelias, P. Gavras, et al. Evolved massive stars at low-metallicity-V. Mass-loss rate of red supergiant stars in the Small Magellanic Cloud. *Astronomy & Astrophysics*, 676:A84, 2023.

S. C. Yoon, N. Langer, and C. Norman. Single star progenitors of long gamma-ray bursts- I. model grids and redshift dependent GRB rate. *Astronomy & Astrophysics*, 460(1):199–208, 2006.

S.-C. Yoon, S. E. Woosley, and N. Langer. Type Ib/c supernovae in binary systems. I. evolution and properties of the progenitor stars. *The Astrophysical Journal*, 725(1):940, 2010.

T. Yoshida and H. Umeda. A progenitor for the extremely luminous type Ic supernova 2007bi. *Monthly Notices of the Royal Astronomical Society: Letters*, 412(1):L78–L82, 2011.

N. Yusof, R. Hirschi, G. Meynet, P. Crowther, S. Ekström, U. Frischknecht, C. Georgy, H. Kassim, and O. Schnurr. Evolution and fate of very massive stars. *Monthly Notices of The Royal Astronomical Society*, 433(2):1114–1132, 2013.

N. Yusof, R. Hirschi, P. Eggenberger, S. Ekström, C. Georgy, Y. Sibony, P. Crowther, G. Meynet, H. Kassim, W. Harun, et al. Grids of stellar models with rotation VII: models from 0.8 to 300 $M_\odot$ at supersolar metallicity (Z= 0.020). *Monthly Notices of the Royal Astronomical Society*, 511(2):2814–2828, 2022.

J.-P. Zahn. The dynamical tide in close binaries. *Astronomy and Astrophysics*, 41:329–344, 1975.

J.-P. Zahn. Tidal friction in close binary stars. *Astronomy and Astrophysics*, 57: 383–394, 1977.

J.-P. Zahn. Circulation and turbulence in rotating stars. *Astronomy and Astrophysics*, 265:115–132, 1992.

J.-P. Zahn. Stellar tides. In *Tides in astronomy and astrophysics*, pages 301–325. Springer, 2013.

H. Zinnecker and H. W. Yorke. Toward understanding massive star formation. *Annu. Rev. Astron. Astrophys.*, 45:481–563, 2007.

S. Zucker and T. Alexander. Spectroscopic binary mass determination using relativity. *The Astrophysical Journal*, 654(1):L83, 2006.